Doctoral Dissertation

Light Responsive Molecular Probes for In Vivo Visualization and Activation of Cellular Functions

Ryu Hashimoto

January 2024

Laboratory of Chemical Biology

Division of Applied Chemistry

Graduate School of Engineering

Osaka University

Contents

General Introduction

Light is unsurpassed in its ability to control biological systems with high spatial and temporal resolution. It has the advantages of noninvasive and remote action, reversibility, speed, and facile modulation of the energies involved (**Figure 1**). Over the past two decades, light has provided a noninvasive tool to probe or perturb biological systems by incorporating light-active reporters or triggers in synthetic compounds.[1] Precise switching the activity of such molecules leads us to analyze downstream molecular biological processes, investigate associating biomolecules, and ultimately control the cellular dynamics toward therapeutics.[2] The use of light-activatable synthetic molecules has grown in biology, pharmacology, and medicine. Synthetic fluorescent probes are one of the powerful light-activatable tools because of their high sensitivity, specificity, fast response, and technical simplicity. They can inherit various functional switches that can detect various physiological factors associated with cell activity[3] because synthetic fluorescent probes are constructed from flexible scaffolds by organic synthesis. They can provide direct visualization of microenvironments (e.g., pH, viscosity, and polarity) and dynamic information concerning the localization and quantity of biomolecules of interest (e.g., ions, reactive oxygen species, and enzymes).[4] The observation of fluorescently labeled cells by light achieved novel findings in the various areas of basic and applied life sciences.

A "second use" of light, which is namely optical control of bioactivity, has been emerged in the late 1970s with the invention of caged compounds.[5] Caged compounds are

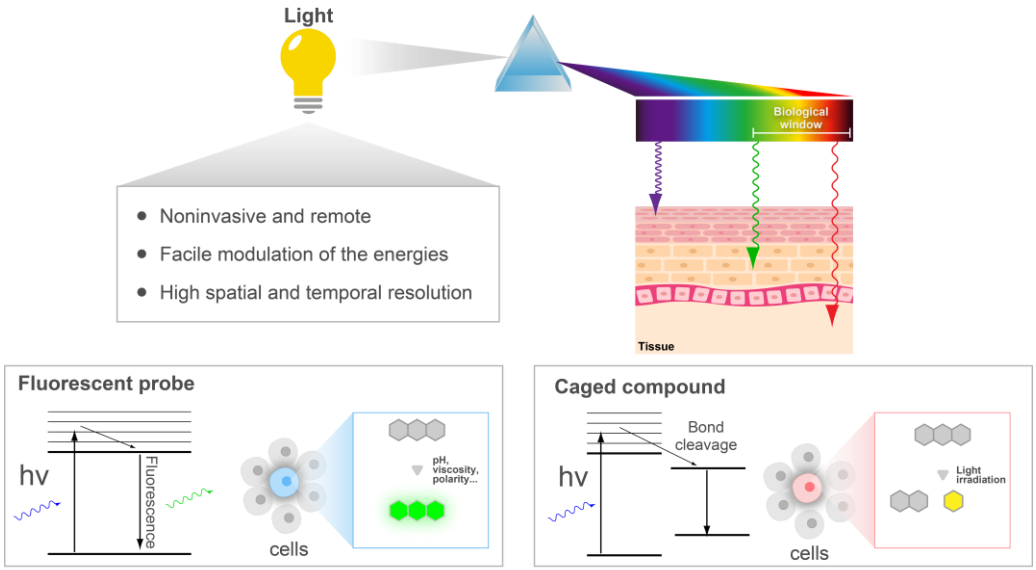

Figure 1. Schematic illustration of variation of tissue penetration depth according to wavelength and light-activatable synthetic molecules.

physiological signaling molecules that have been rendered biologically inert by covalent attachment of photoremovable protective groups (PPGs).[5] Illumination results in the release of the biomolecules (uncaging) and a subsequent concentration jump, which allows binding to cellular receptors and switching on or off the targeted process. These light-based approaches undoubtedly contribute to new findings in tracking biological function.

In vivo analysis of biological processes at subcellular resolution provides realistic images of heterogeneous cell dynamics in response to stimulation by extracellular signaling molecules,[6] cell–matrix contacts,[7] and cell–cell communication.[8] To achieve in vivo analysis, it is necessary to deliver or activate light-responsive probes in specific tissues or cells. One approach is the active-targeting probes, where ligands capable of delivering probes specifically to certain tissues are introduced, allowing their accumulation in the target tissues (**Figure 2 Left**). This enables the selective capture of molecules of interest within complex biological tissues. Another approach involves the site-specific activation of molecules using light and caged compounds (**Figure 2 Right**). To activate target cells, simply adding bioactive molecules is challenging to investigate the desired cell functions due to the diffusion. However, by using caged compounds that can release probes or bioactive molecules upon exposure to light, it can selectively activate the intended cells.

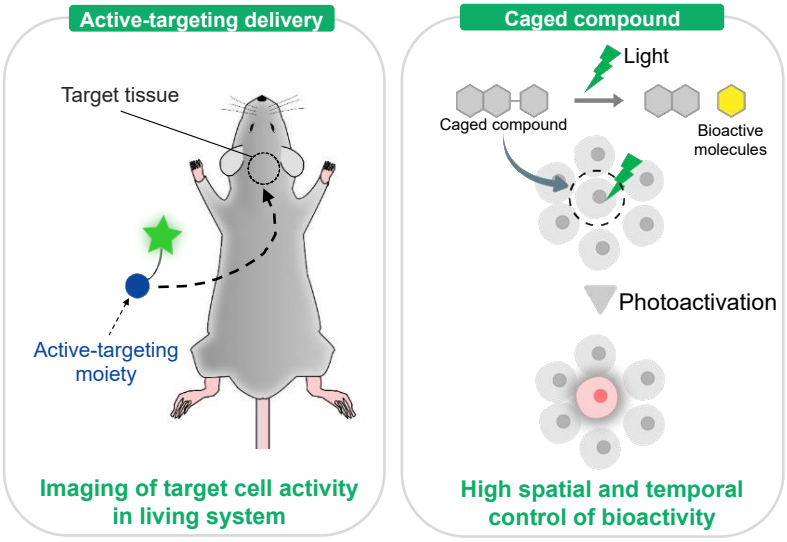

Figure 2. Schematic illustration of in vivo imaging by fluorescent probes with active-targeting moiety and light-inducible activation of cellular function by caged compounds.

The ability to visualize live and intact tissue at the cellular and subcellular level has seen incredible advances over the past two decades. In the beginning, ultraviolet (UV)/blue irradiation responsive systems have been used for various applications. UV/blue light is high energy which can lead to phototoxicity and has limited low tissue penetration depth owning to a strong scattering and absorption by water, and major tissue chromophores, including hemoglobin, oxyhemoglobin, and melanin. Therefore, visible/near-infrared (NIR) light with wavelengths ranging from 500–900 nm which can penetrate deeply into

the tissues is preferred for cellular or in vivo imaging and uncaging due to its minimal attenuation by soft tissues, blood, and water.

One of the core techniques driving in vivo imaging and uncaging is multiphoton (two-photon) excitation (MPE) microscopy.[9] Especially, two-photon excitation (2PE) microscopy with NIR allows for deeper tissue penetration, diminished phototoxicity, and high 3D resolution in living tissue and animals. 2PE microscopy produces the excited singlet state of a chromophore with wavelengths approximately double that used for one-photon excitation. Two photons are absorbed almost simultaneously, via a virtual state, and this makes the excitation technique inherently non-linear. To make it work, the photons must arrive nearly simultaneously within a femtosecond, resulting in the fluorescence signal upon excitation only coming from the focal point. This property can bring us a high 3D resolution. By combination with fluorescence imaging or uncaging techniques based on fluorescent molecular probes or caged compounds, 2PE can be used to visualize and control single-cell functions in complex in vivo environments.

Outline of Research

***Fluorescent probe*:** Intravital imaging by 2PE microscopy has been widely used to visualize cell functions.[10] However, small molecular probes, commonly used for cell imaging, cannot be simply applied to intravital imaging because of the challenge of delivering them into target tissues, as well as their undesirable physicochemical properties for 2PE imaging. Recently, the author's research group reported in vivo 2PE imaging of osteoclast activity on bone tissue with reversible OFF/ON pH-sensing probes.[11–13] These probes contain bisphosphonate-derived alendronate fragments that bind strongly to the bone matrix enabling visualization of osteoclast-mediated bone resorption processes.

In Chapter 1, a pH-activatable fluorescent probe (pHocas-RIS) was developed to measure localized pH levels in osteocytic lacunae in bone tissue. Conjugation of the moderate bone-binding drug risedronate to a pH-activatable BODIPY fluorophore enables the probe to penetrate osteocytic lacunae cavities that are embedded deep within the bone matrix. After injection of pHocas-RIS, any osteocytic lacunae caused by bone-resorbing osteocytes cause the probe to fluoresce in vivo, thus allowing imaging by intravital 2PE microscopy. This pH-responsive probe enabled the visualization of the bone mineralizing activities of acid producing osteocytes in real-time, thus allowing the study of their central role in remodeling the bone matrix in healthy and disease states.

***Caged compound*:** Caged compounds are powerful tools for noninvasive spatial and temporal control of bioactivity and are produced by incorporating PPGs into the structure of bioactive compounds. Unfortunately, most PPGs require high-energy UV-light

illumination, which leads to cellular damage or death at a low tissue penetration depth. In the biological setting, longer-wavelength light uncaging is desirable. As an alternative to long-wavelength light uncaging methods, 2PE with NIR light provides deeper tissue penetration, reduced phototoxicity, and high 3D resolution. Although some UV/blue-light-sensitive caged compounds can be activated by 2PE (~740–800 nm), fewer 2PE-sensitive chromophores are available to long-wavelength light (~900 nm) for biological applications. Therefore, the development of long-wavelength light-sensitive PPGs with high cleavage efficiency in aqueous solution is still a significant challenge.

In Chapter 2, the author presented a new molecular framework for one-photon visible (490–505 nm) or two-photon (940 nm) excitation-responsive PPGs with high cleavage efficiencies in aqueous solution. The author rationally designed and synthesized hydroxylated thiazole orange dye-based PPGs (HTO), which possess efficient photodegrading structures (7-hydroxyquinoline/quinolinium moieties[14,15]) in a visible-light-absorbing chromophore. Importantly, the uncaging efficiencies ($\varepsilon\Phi \approx 110$~$370$, where ε and Φ are the molar absorption coefficients and photolysis quantum yield, respectively) of HTO-caged compounds were superior to those reported for green light-responsive PPGs in the aqueous condition. The author demonstrated optical control of *N*-methyl-D-aspartic acid (NMDA) receptors in *Xenopus* oocytes and mammalian HEK293T cells with a glutamate-conjugated HTO-caged compound (Sul-HTO-Glu). The illumination of 505 nm light on Sul-HTO-Glu successfully released glutamate under biological conditions and activated NMDA receptors with controlled timing. In addition, the 2PE photolysis reaction of Sul-HTO-Glu was achieved using a NIR laser (940 nm). Finally, the author showed single-spine stimulation by 2PE uncaging of Sul-HTO-Glu.

In Chapter 3, the author showed the development of more efficient HTO-based PPGs and the optical control of DNA recombination with high spatiotemporal efficiency. The precise control of DNA recombination enables the cell- or time-dependent regulation of gene expression in studies of gene function. Caged estrogen receptor ligands combined with a Cre-ERT2/loxP system are useful tools for light-triggered DNA recombination.[16] However, the photolysis of most caged estrogen receptor ligands requires UV or blue light, which is toxic and displays low tissue penetration. Although a cyanine-based PPG can release estrogen receptor ligands with longer-wavelength light, its low photolytic efficiency requires long illumination times.[17,18] Therefore, the author developed a caged estrogen receptor ligand with improved green-light-responsive PPGs. The rational modification of HTO photocages using electron-donating groups (EDGs), such as dimethoxy (DiMeO)-substituted HTO, resulted in high photolytic efficiency (up to $\varepsilon\Phi \approx 320$). Theoretical calculations demonstrated that the enhanced photolytic efficiencies

were derived from the increased intramolecular charge transfer by EDGs upon excitation. The efficient uncaging of estrogen receptor ligands enabled the control of gene recombination in a ligand-dependent Cre-ERT2/loxP system in live cells.

Reference

[1] K. Hüll, J. Morstein, D. Trauner, *Chem. Rev.* **2018**, *118*, 10710–10747.

[2] S. Jia, E. M. Sletten, *ACS Chem. Biol.* **2022**, *17*, 3255–3269.

[3] S. B. Wagh, V. A. Maslivetc, J. J. La Clair, A. Kornienko, *ChemBioChem* **2021**, *22*, 3109–3139.

[4] H. Zhu, J. Fan, J. Du, X. Peng, *Acc. Chem. Res.* **2016**, *49*, 2115–2126.

[5] S. Kawahama, *Tanpakushitsu. Kakusan. Koso.* **2007**, *52*, 1772–1773.

[6] S. Giampieri, C. Manning, S. Hooper, L. Jones, C. S. Hill, E. Sahai, *Nat. Cell. Biol.* **2009**, *11*, 1287–1296.

[7] M. Ishii, J. G. Egen, F. Klauschen, M. Meier-Schellersheim, Y. Saeki, J. Vacher, R. L. Proia, R. N. Germain, *Nature* **2009**, *458*, 524–528.

[8] M. J. Miller, S. H. Wei, I. Parker, M. D. Cahalan, *Science* **2002**, *296*, 1869–1873.

[9] W. Denk, J. H. Strickler, W. W. Webb, *Science* **1990**, *248*, 73–76.

[10] F. Helmchen, W. Denk, *Nat. Methods* **2005**, *2*, 932–940.

[11] T. Kowada, J. Kikuta, A. Kubo, M. Ishii, H. Maeda, S. Mizukami, K. Kikuchi, *J. Am. Chem. Soc.* **2011**, *133*, 17772–17776.

[12] H. Maeda, T. Kowada, J. Kikuta, M. Furuya, M. Shirazaki, S. Mizukami, M. Ishii, K. Kikuchi, *Nat. Chem. Biol.* **2016**, *12*, 579–585.

[13] M. Minoshima, J. Kikuta, Y. Omori, S. Seno, R. Suehara, H. Maeda, H. Matsuda, M. Ishii, K. Kikuchi, *ACS Cent. Sci.* **2019**, *5*, 1059–1066.

[14] Y. Zhu, C. M. Pavlos, J. P. Toscano, T. M. Dore, *J. Am. Chem. Soc* .**2006**, *128*, 4267–4276.

[15] T. Narumi, K. Miyata, A. Nii, K. Sato, N. Mase, T. Furuta, *Org. Lett.* **2018**, *20*, 4178–4182.

[16] T. Faal, P. T. Wong, S. Tang, A. Coulter, Y. Chen, C. H. Tu, J. R. Baker, S. K. Choi, M. A. Inlay, *Mol. Biosyst.* **2015**, *11*, 783–790.

[17] A. P. Gorka, R. R. Nani, J. Zhu, S. Mackem, M. J. Schnermann, *J. Am. Chem. Soc* .**2014**, *136*, 14153–14159.

[18] A. P. Gorka, T. Yamamoto, J. Zhu, M. J. Schnermann, *ChemBioChem* **2018**, *19*, 1239–1243.

Chapter 1

An Acid Activatable Fluorescence Probe for Imaging Osteocytic Bone Resorption Activity in Deep Bone Cavities

Introduction

Long lived osteocytes constitute around 90–95% of all bone cells, which exist within disk-shaped cavities called osteocytic lacunae that are present throughout the mineralized bone matrix.[19] These lacunae are interconnected by a three-dimensional canalicular network that penetrates widely throughout the bone matrix. Osteocytes project their long dendrites into these canals, which allows them to detect and modulate shear stress through communication with surface bound osteoblasts and osteoclasts that are responsible for modifying bone structures.[20] For example, osteocytes upregulate the bone resorbing activities of osteoclasts through secretion of osteoprotegerin and receptor activator of nuclear factor kappa-B ligand (RANKL), whilst they downregulate osteoblast bone forming activities through secretion of sclerostin.[21] This means that osteocytes play a central role in controlling bone remodelling pathways that are important in maintaining bone homeostasis and central to disease processes such as osteoporosis and bone cancer metastasis.[22]

Osteocytes exist deep within the bone matrix, so it is challenging to study their morphologies, activities and cellular dynamics in live animals using conventional histochemical, topographic, diffraction and imaging techniques.[23] This has led to ex vivo and in vivo imaging techniques being developed that employ fluorescence microscopy and/or fluorescent probes to image osteocytes and their associated lacuna-canalicular networks in real time. For example, transgenic reporter mice producing osteocytes that express green fluorescent proteins in their cytoplasm have been used to provide high resolution images of osteocyte dendrites oscillating within their lacunae in bone explant.[24] Alternatively, Ca^{2+} binding fluorescent dyes have been used to visualize the structures of osteocytic lacuna-canalicular networks.[25]

Osteocytes are known to directly remodel the bone walls of their lacuna-canalicular systems in response to hormones produced by lactating or hibernating animals, with lacunae bone wall mineralization producing larger cavities in a process known as osteocytic osteolysis.[26] However, the physiological role of osteocytes in direct bone mineralization to produce Ca^{2+} is still open to debate,[27] so the availability of high-resolution imaging method that would enable osteocytic osteolysis to be imaged in real-time would be extremely useful. Osteocytes can directly mineralize the bone matrix of

the cavity walls of their lacunae through the secretion of acid from vacuolar type H+-ATPases.[28] Therefore, osteocytic bone mineralization activity can potentially be visualized indirectly through the use of an OFF/ON pH-sensitive fluorophore and two-photon excitation microscopic analysis to image pH levels in the lacuna-canalicular system.

The intravital imaging approach has been used to image the walls of osteocytic lacunae through the application of a pH-sensitive dye (AcidiFluor^{TM} ORANGE) to exposed surfaces of tibiae. This enabled in vivo imaging studies to be used to demonstrate that sciatic neurectomy in mice leads to a significant increase in the pH of the osteocytic lacunae and mineralization of the lacuna-canalicular networks in their tibiae.[25] In another ex vivo study, injection of acridine orange into mice that were pre-treated with parathyroid hormone related protein (osteocytic osteolysis promoter) enabled acidic lacunae in tibia bone explants to be imaged.[28] However, neither of these approaches is suitable for real-time visualization of local pH variations in osteocytic lacunae in live animal models, because the pH-sensitive dyes they employ are not selective for bone surfaces and so cannot produce stable well-resolved images to allow in vivo monitoring to be carried out over long periods.

The author's group has previously developed reversible OFF/ON pH-sensing probes containing bis-phosphonate derived alendronate fragments that bind strongly to the bone matrix that enabled visualization of osteoclast mediated bone resorption processes.[11–13] These fluorescent probes exhibit good environmental stability, large molar absorption coefficients, and high fluorescence quantum yields, which makes them well suited for visualizing the low pH environments of bone surfaces in vivo. This allows their fluorescence properties at low pH to be used to monitor the bone resorption activities and motilities of osteoclasts on bone surfaces and the effect of cytokines, immune cells and drugs on their activities. For example, the use of the photostable boron dipyrromethene (BODIPY) based pH-activatable fluorescent probe (pHocas-3) in transgenic reporter mice whose osteoclasts expressed tartrate-resistant acid phosphatase (TRAP)-promoter-driven red fluorescent protein (tdTomato)[29] in their mature osteoclasts enabled in vivo time-lapse imaging of osteoclast dynamics.[12] This study revealed that static osteoclasts actively promote acid mediated bone resorption, whilst motile osteoclasts do not dissolve bone surfaces. Additionally, interrogation of cellular interactions in mature osteoclasts and osteoblasts with pHocas-3 revealed that direct contact with an osteoblast resulting in an osteoclast becoming mobile and ceasing its acid secreting and bone resorption activity.[30]

Unfortunately, attempts to employ pHocas-3 for the intravital imaging of low-pH regions

in osteocytic lacunae within the bones of living mice proved unsuccessful, because its strong bone binding alendronate fragments prevent it from effectively penetrating bone surfaces. Consequently, the author now reports herein the development of an alternative pH-activatable probe containing risedronate fragments, whose moderate bone binding affinity enables it to penetrate deep within the bone matrix. This enables this new OFF/ON pHocas-RIS probe to be used to carry out real-time intravital two-photon fluorescence imaging of acidic environments of not only bone surfaces but also osteocytic lacunae that contain acid secreting osteoclasts/osteocytes that are actively involved in bone resorption in the bones of live animals (**Figure 3**).

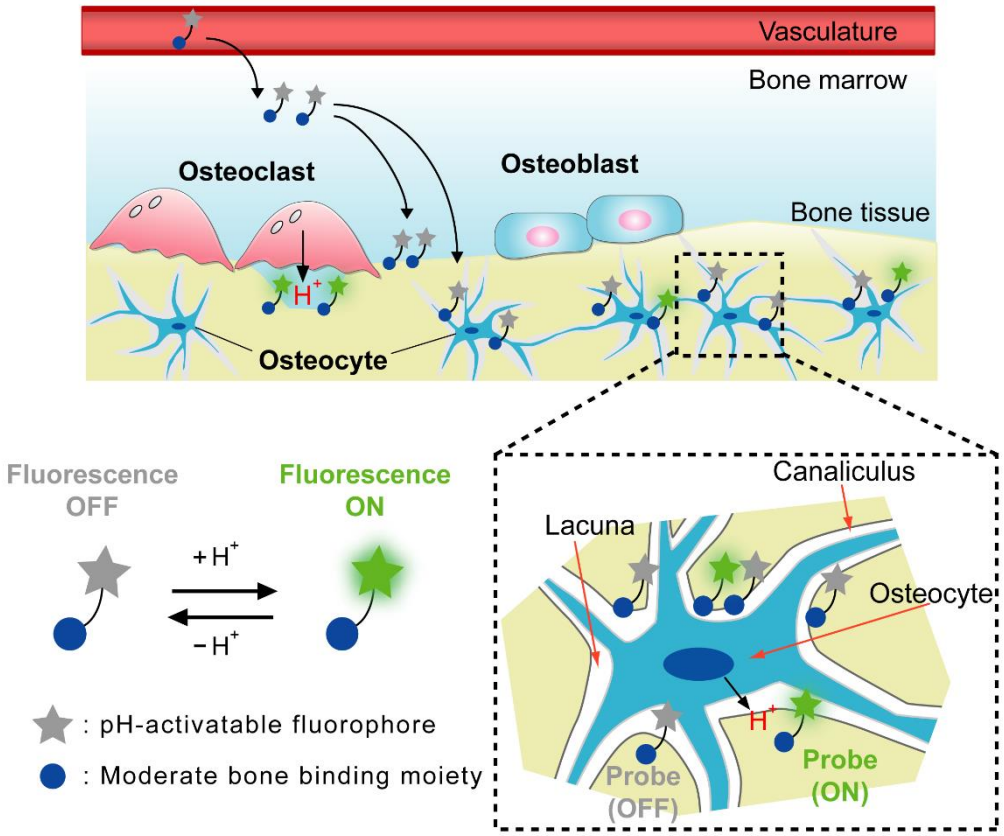

Figure 3. Targeted delivery of a pH-activatable pHocas-RIS probe from the vasculature to bone surfaces and the bone walls of osteocytic lacunae. Osteocyte cell shown in blue, bone walls shown in grey. Dark blue oval represents nucleus of osteocyte.

Results and Discussion

Risedronate is a bisphosphonate drug used for the treatment of osteoporosis that binds to bone mineral through interaction with calcium ions in hydroxyapatite (HAP) in bones.[31] It exhibits lower bone binding affinity than alendronate, which enables it to distribute itself more widely throughout the bone matrix, including attachment to the walls of

osteocytic lacunae.[32] Consequently, the author reasoned that attachment of risedronate fragments to a pH-activatable BODIPY fluorophore would afford a new pHocas-RIS probe that could be used to visualize the low pH environments of osteocytic lacunae that contained acid secreting osteocytes (**Figure 4**). Two new BODIPY-containing fluorescent probes [pH-activatable pHocas-RIS and always-ON pHocas-AL-RIS (**Figure 5a**)] bearing bone targeting risedronate fragments were prepared through modification of a previously reported procedure involving use of a 3-aminopropane oxide linker to attach two equivalents of risedronate to a BODIPY dye (**Scheme 1**).[33] Reversible protonation of the basic nitrogen atom of the tertiary para-diethylamino group of pHocas-RIS means that it can function as an ON/OFF pH switch to modulate the fluorescent output of the BODIPY fluorophore through a photoinduced electron transfer (PET) mechanism.

Scheme 1. Synthetic scheme of pHocas-RIS and pHocas-AL-RIS.

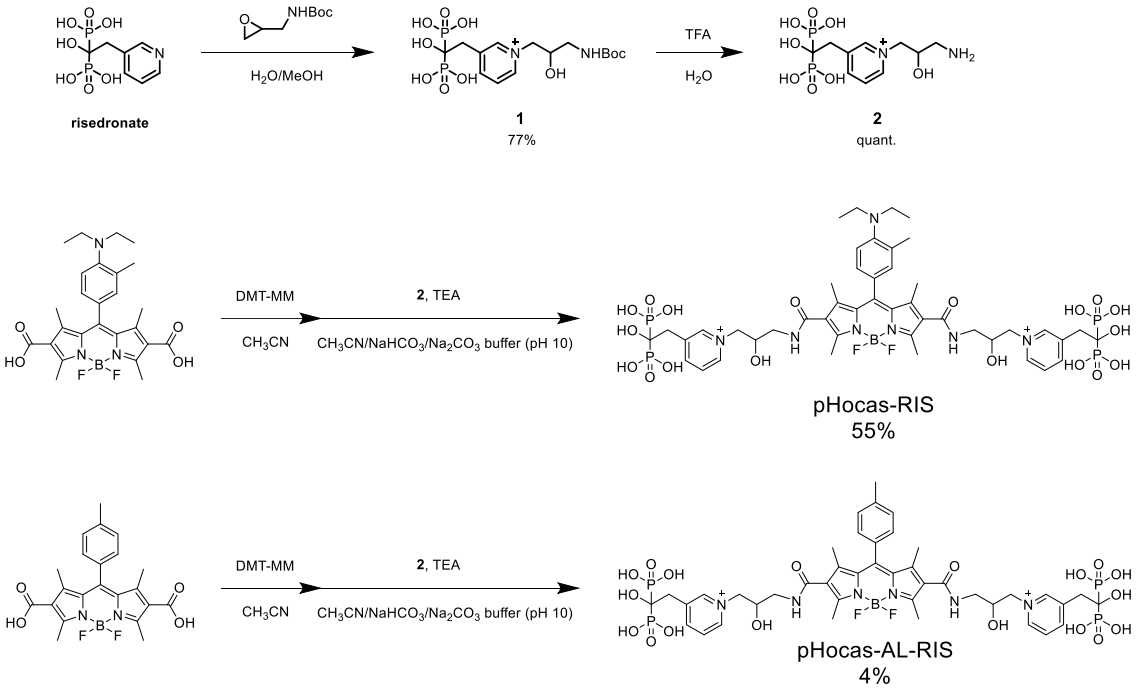

The pK_a value of the *N*,*N*-diethyl-2-methylaniline fragment was calculated to be around 6.6,[34] meaning that it is well suited to function as a protonatable OFF/ON switch over the pH range of 4.5-7.4 that commonly exist in lacunae.[25] pHocas-AL-RIS, which contains a BODIPY fragment with a para-tolyl substituent, was prepared as a control probe whose fluorescence would be "always-ON", regardless of pH.

The fluorescence quantum yields (QY) of the probes at different pH values were acquired by measuring their absorption and fluorescence emission spectra in citrate-phosphate

buffer (**Figure 5b**). The fluorescence intensity of the pHocas-RIS probe increased approximately 15-fold as the pH decreased from 8.0 to 4.0, with changes in its QY at different pH levels used to calculate the pK_a value of its aniline moiety as 6.8 (**Figure 5c**). Conversely, as expected, the QY of pHocas-AL-RIS was found to be pH independent (**Figure 5c**). The QY values of protonated pHocas-RIS and pHocas-AL-RIS were similar in value to BODIPY,[12] thus indicating that the risedronate fragments had not adversely affected the probe's fluorescence properties.

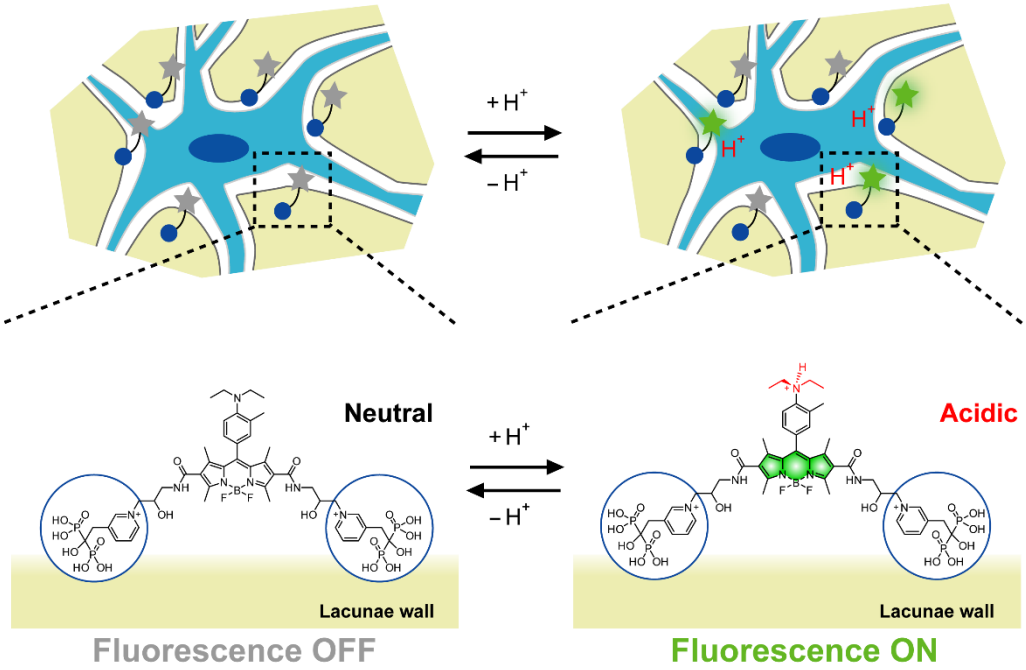

Figure 4. Release of acid from osteocytes results in a decrease in the pH of their osteocytic lacunae which results in protonation of the diethylamino nitrogen atom of the BODIPY fluorophore. This results in PET quenching resulting in the fluorescent activity of the BODIPY fluorophore of bone bound pHocas-RIS being turned ON.

HAP samples were soaked in a solution of pHocas-RIS in buffers at different pH values (pH 4.5-8.0), with the resultant HAP bound probes then imaged using the fluorescence confocal microscopy. The fluorescence signals of the HAP particles treated with pHocas-RIS were very weak at pH 8.0 while the fluorescence intensity of the HAP-probe samples increasing dramatically at low-pH (pH 5.0) **(Figure 6a)**, which was similar to the pH fluorescence response of the free probe in aqueous solution (**Figure 5c**).

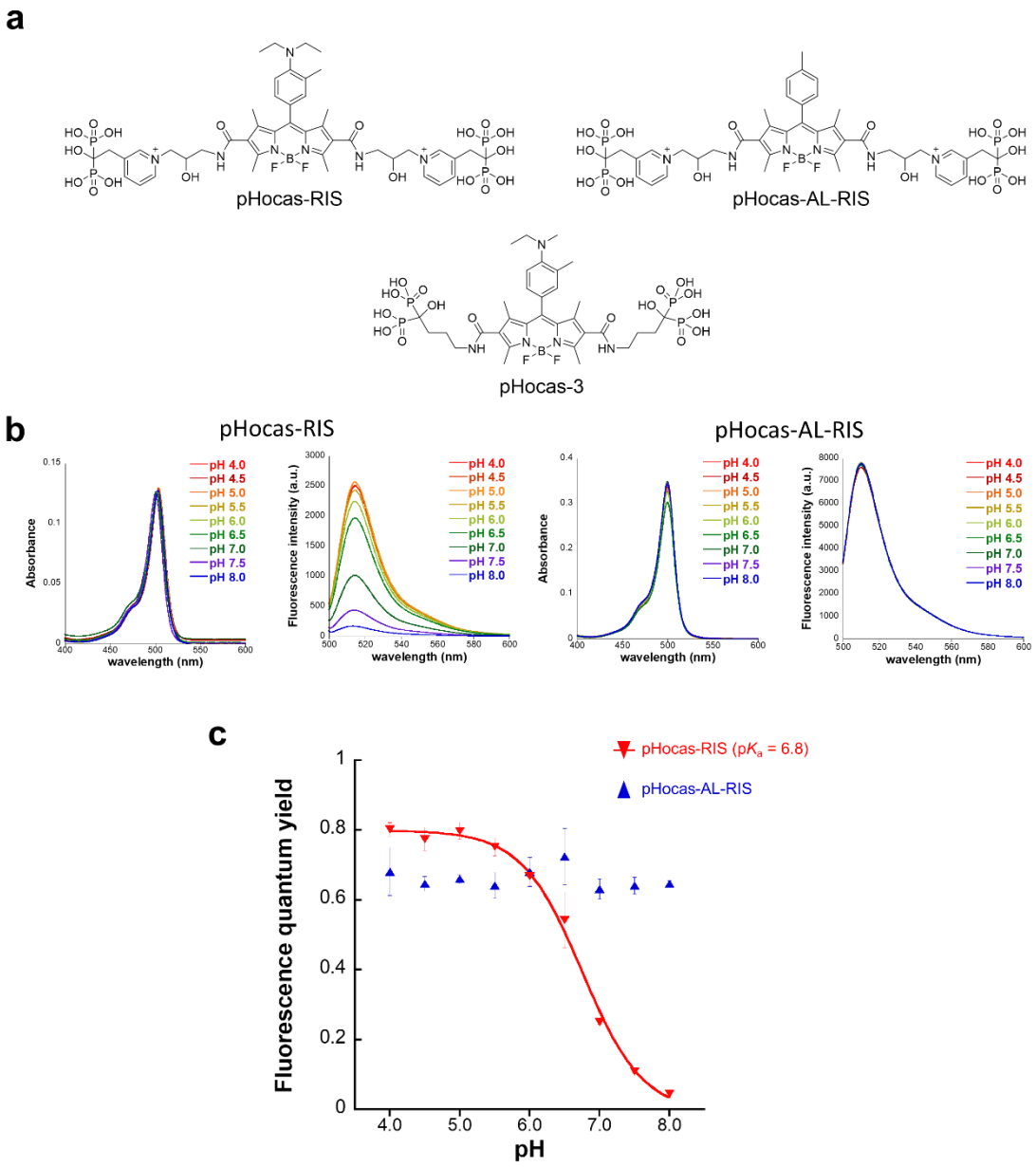

Figure 5. (a) Risedronate containing pH-activatable pHocas-RIS probe; Risedronate containing always-ON pHocas-AL-RIS probe; Alendronate containing pHocas-3 probe. (b) Absorption and Intensity of Fluorescence spectra (excited at 492 nm) of pHocas-RIS and pHocas-AL-RIS in citrate-phosphate buffer (pH 4.0-8.0) increases as pH decreases. (c) pH profiles of the fluorescence quantum yields of pHocas-RIS and pHocas-AL-RIS. Fluorescence quantum yields estimated using fluorescein (0.1 N NaOH, Φ 0.85) as a control. Data are presented as mean values with ± s.d. (N = 3).

Conversely, as expected, the fluorescence intensity of HAP particles bound to always-ON pHocas-AL-RIS probe remained constant over the pH range from 4.5-8.0 (**Figure 6b**). No dissociation of either risedronate-conjugated probes from the HAP particles was

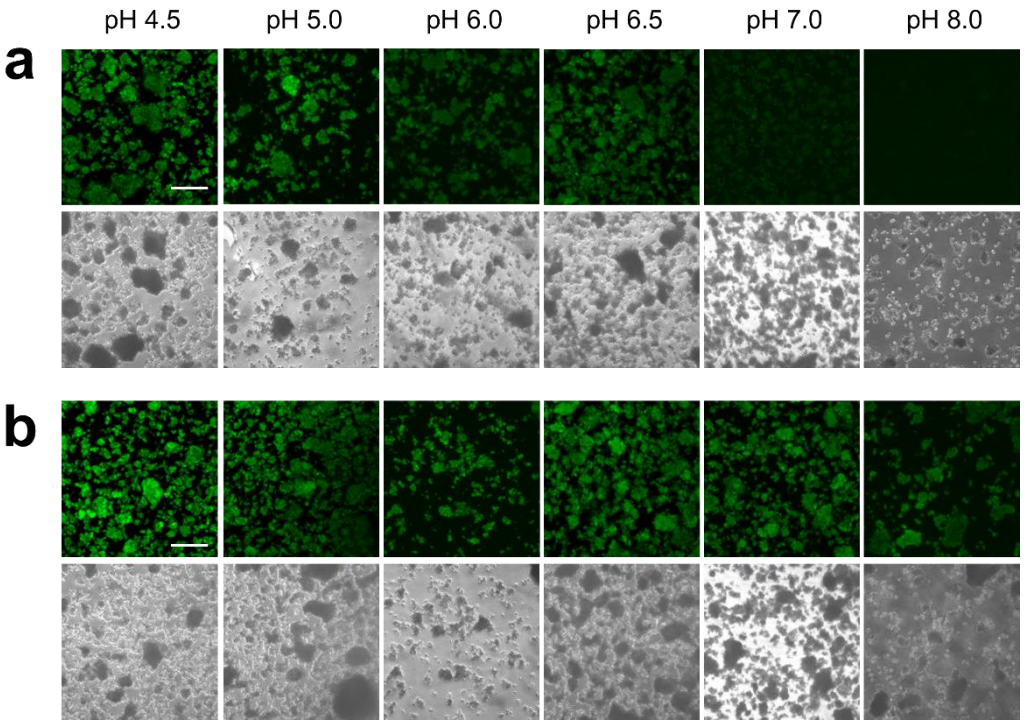

Figure 6. Confocal microscopic images of (a) pHocas-RIS and (b) pHocas-AL-RIS bound to hydroxyapatite in McIlvaine's citrate-phosphate buffer. Scale bar: 25 μm.

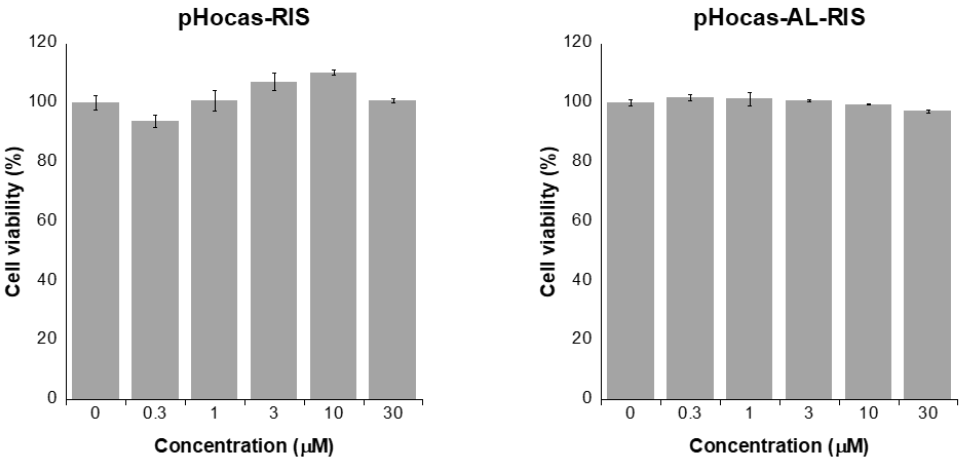

Figure 7. Cytotoxicity results of pHocas-RIS and pHocas-AL-RIS against RAW264.7 cells. Error bars denote ± SD ($N = 3$).

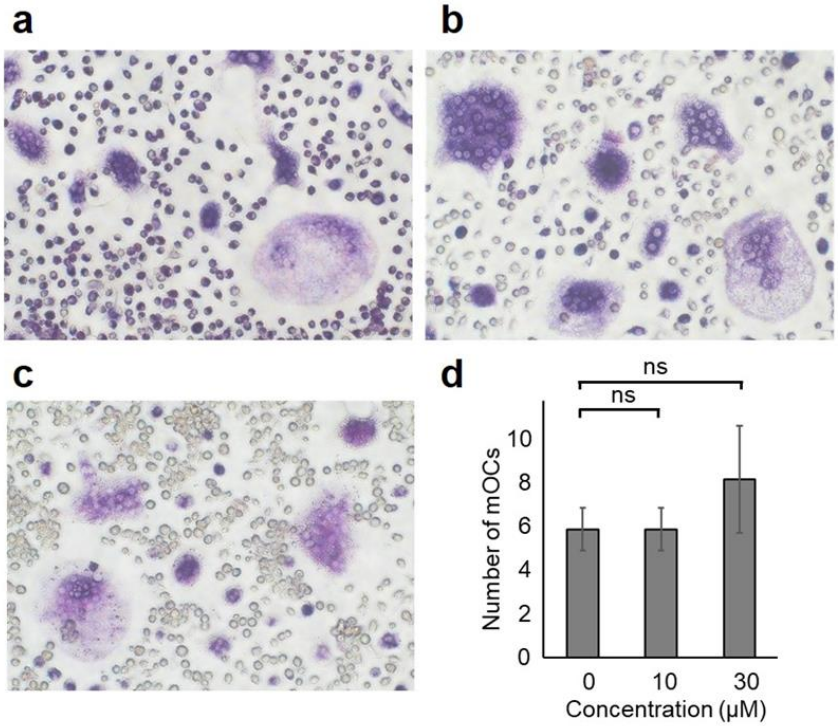

Figure 8. Effects of pHocas-RIS on RANKL-induced osteoclastogenesis. Bone marrow-derived macrophages were cultured with 10 ng/mL M-CSF, 50 ng/mL RANKL, and pHocas-RIS ((a) 0, (b) 10, and (c) 30 μM) for 4 days. The cells were fixed and stained to determine tartrate-resistance acid phosphatase (TRAP) activity. TRAP-positive multinucleated (>3 nuclei) cells were regarded as being mature osteoclasts. (d) The number of mature osteoclasts (mOCs) in each condition. Error bars denote ± SD ($N = 3$). ns, not significant (student *t*-test).

observed over time, thus indicating that both probes remained permanently bound to HAP over the time-course of these imaging experiments. These probes exhibit no cytotoxicity against cultured RAW264.7 cells that can be differentiated into osteoclasts (**Figure 7**), whilst pHocas-RIS did not inhibit RANKL-induced osteoclastogenesis (**Figure 8**).

Imaging studies were then carried out using transgenic TRAP-tdTomato mice containing osteoclasts expressing a red fluorescent protein.[29] Daily subcutaneous administration of both probes (5 mg/kg) to these genetically modified mice over a 3 day period was followed by their anaesthetisation and two-photon imaging of the medullary cavities of their thin calvaria parietal bones. Processing of the images were carried out using spectroscopic unmixing algorithms that enabled fluorescence signals from the probe (green), tdTomato (red) and second-harmonic generation (SHG) emissions of bone collagen fibres (blue) to be distinguished. Green fluorescence signals from pHocas-AL-

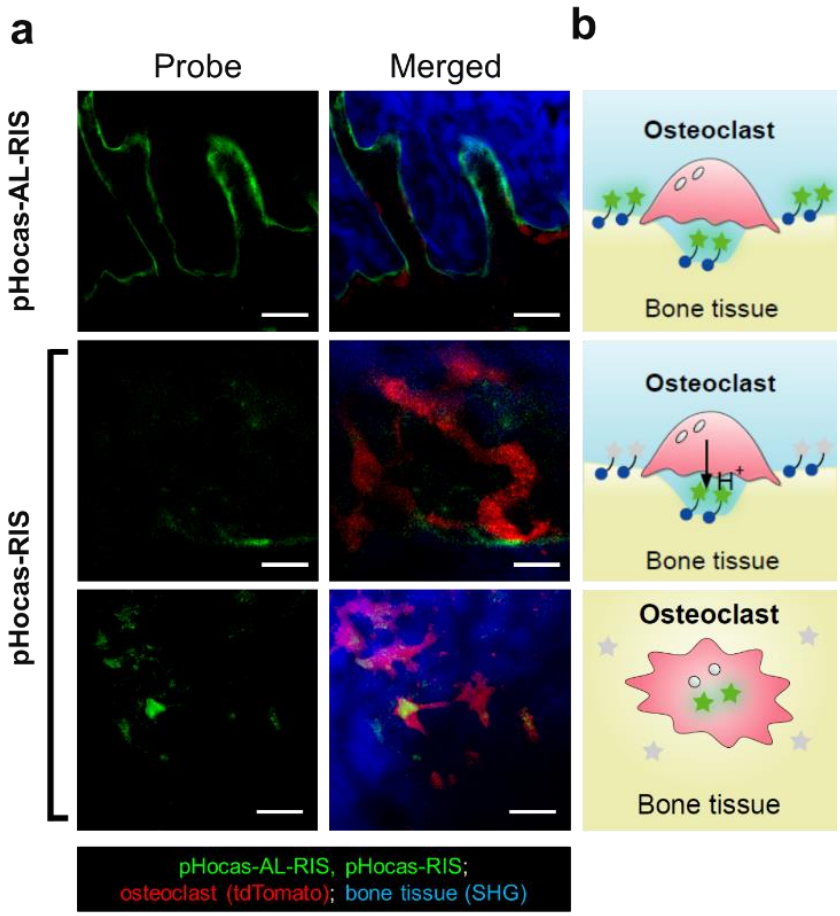

Figure 9. (a) Two-photon excitation imaging of pHocas-AL-RIS and pHocas-RIS in the bone tissue of living transgenic mice. Emissions: pHocas probes in green; tdTomato protein in osteocytes in red; Collagen in bone matrix in blue. Excitation: 940 nm. Scale bar: 50 µm (pHocas-AL-RIS, top); 20 µm (pHocas-RIS, middle); 50 µm (pHocas-RIS, bottom). Second harmonic generation from collagen in the bone matrix responsible for blue fluorescent signals. (b) Schematic illustration of bone tissues.

RIS were present across the entire parietal bone surface (**Figure 9**, top left), thus indicating that the risedronate-conjugated probe was evenly distributed over the bone surface.

The fluorescent output of pHocas-AL-RIS on external bone surfaces was not decreased after 90 min (**Figure 10**), thus demonstrating that the BODIPY fluorophore is sufficiently photostable to be used for real time in vivo imaging of bone surfaces over extended periods of time. Imaging studies (from a lateral view) revealed the presence of green fluorescence signals from protonated pH-activatable pHocas-RIS produced from the action of stationary acid secreting osteoclasts in direct contact with bone surfaces within the bone marrow cavity (**Figure 9**, middle). Images of bone surfaces (viewed from above) showed local overlap of protonated pHocas-RIS signals (green) that were coincident with osteoclasts expressing the TRAP-tdTomato gene (red) (**Figure 9**, bottom). Time-lapse imaging could be used to explore spatiotemporal changes in bone acidification levels

induced by the action of osteoclasts (**Figure 11**), with the fluorescence output of protonated pHocas-RIS enabling the appearance of acidified bone surfaces to be detected in real-time. As demonstrated in our previous studies,[11,12] overlap of the green fluorescence signals of the new pH-activatable pHocas-RIS probe with the red fluorescent signals of osteoclasts enabled active acid secreting osteoclasts (bone-resorptive) to be readily discriminated from inactive (non bone-resorptive) osteoclasts.

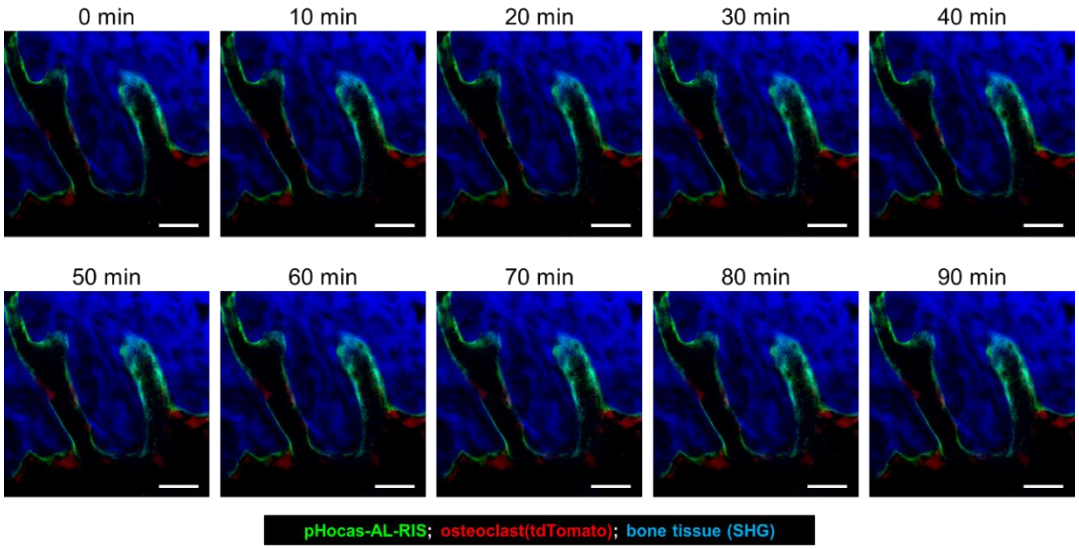

Figure 10. Two-photon time-lapse imaging of bone tissues, with images acquired 90 min after injection of the final dose of pHocas-AL-RIS. Excitation: 940 nm. Scale bar: 50 μm.

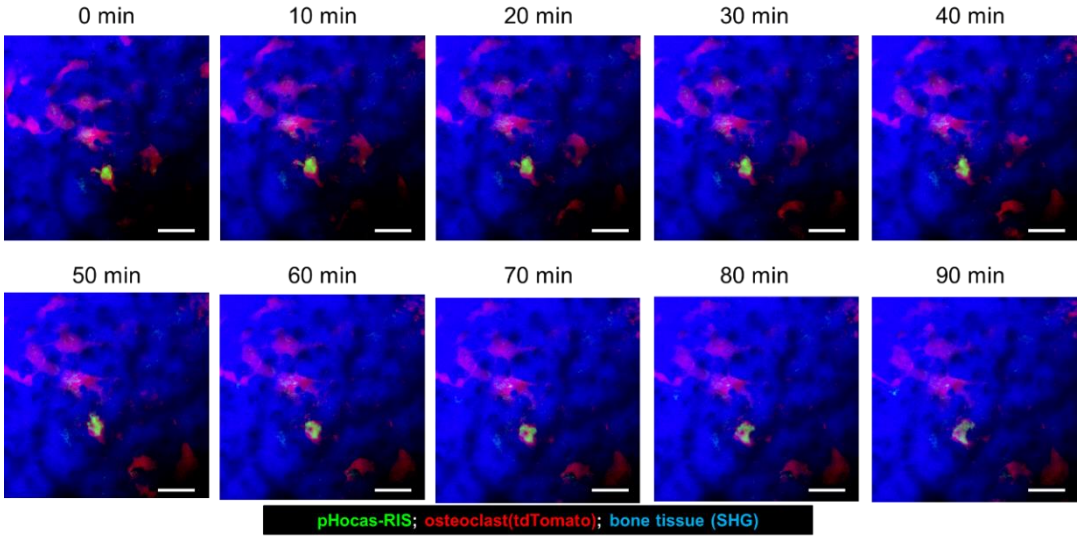

Figure 11. (a) Two-photon time-lapse imaging of bone tissues, with images acquired 90 min after injection of the final dose of pHocas-RIS. Excitation: 940 nm. Scale bar: 50 μm.

Further imaging studies revealed the presence of small numbers of ring-shaped green fluorescence signals of the protonated pHocas-RIS that were present in bone obtained from deep cortical regions. It is proposed that these fluorescent signals originate from probes bound to the walls of osteocytic lacunae that contained bone resorptive osteocytes that were actively secreting acid to create a low pH environment (**Figure 12a**). The relatively low numbers of these fluorescence signals reflect the fact that only a small number of osteocytes are thought to be actively resorbing bone matrix under normal physiological conditions. As expected, our previously reported pHocas-3 probe containing the high bone-affinity alendronate fragment was incapable of penetrating bone surfaces to image osteocytic lacunae (**Figure 12b**). The pH responsiveness of the pHocas-RIS probe within the lacunae of the bone matrix was confirmed by carrying out ex vivo fluorescent imaging of cryogenically prepared deep bone slices at different pH levels (**Figure 13**). These studies revealed the presence of strong fluorescent signals for osteocytic lacunae in a bone section treated at pH 4.0, reduction in fluorescent intensity of a bone section at pH 7.0, and no fluorescence for a bone section treated at pH 10.0. This clearly demonstrated that the intensity of the pH-activatable fluorescent response of the pHocas-RIS probe can be used to effectively image the pH of osteocytic lacunae in living bone. This should enable the probe to be used to visualize the pharmacokinetics of osteoclast and osteocyte mediated bone remodeling processes and help delineate the role that osteocytes play in controlling bone homeostasis in health, aging and disease.

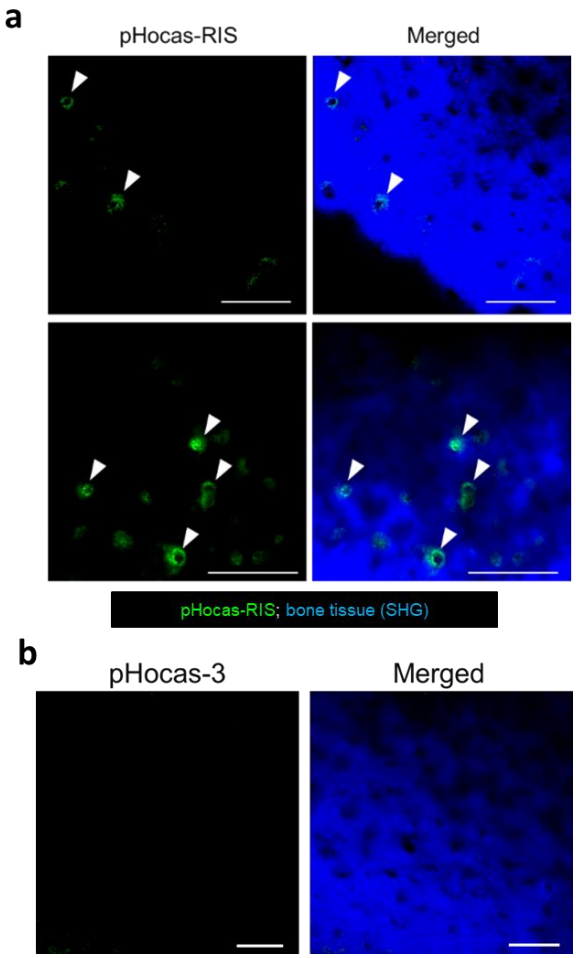

Figure 12. (a) Two-photon excitation imaging reveals green fluorescent regions (see white arrows) corresponding to protonated pHocas-RIS bound to the walls of acidic osteocytic lacunae in calvaria parietal bones. Dose: 5 mg/kg (top), 10 mg/kg (bottom) for 3 days. Excitation: 940 nm. Scale bar: 100 µm. (b) Two-photon imaging with pHocas-3 (alendronate). Dose: 5 mg/kg (over 3 days). Excitation: 940 nm. Scale bar: 50 µm.

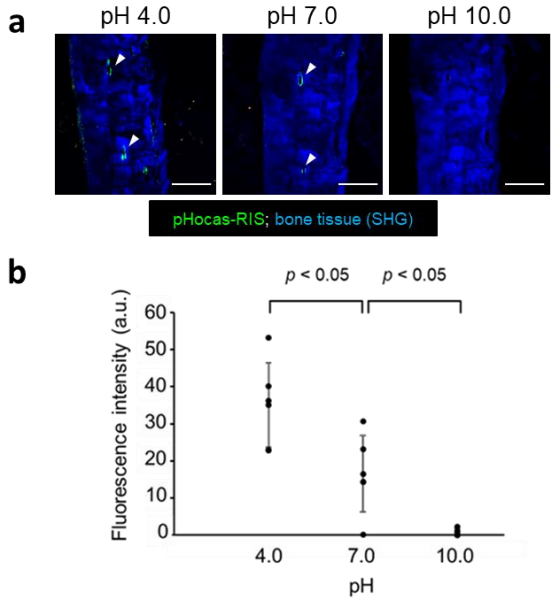

Figure 13. (b) Two-photon excitation imaging of bone tissue cryosections at different pH (pH 4.0, pH 7.0, pH 10.0). Bone cryosections obtained from mice pre-treated with pHocas-RIS that were then pre-soaked in buffers of different pH prior to imaging. Scale bar: 150 μm. White arrows indicate green fluorescent regions corresponding to protonated pHocas-RIS bound to the walls of acidic osteocytic lacunae. Second harmonic generation from collagen in the bone matrix responsible for blue background signals. (c) Quantification of fluorescence intensity in osteocytic lacunae at different pH (pH 4.0, pH 7.0, pH 10.0). Data are presented as mean ± SDs (N = 5). Significance was evaluated using a student t-test.

Experimental Methods

General

All reagents were purchased from Tokyo Chemical Industries, Wako Pure Chemical, or Sigma-Aldrich Chemical Co. and used without further purification. Analytical thin-layer chromatography was performed on 60F254 silica plates (Merck & Co., Inc.) and visualized under UV light. Flash auto purification was carried out using an Isolera Spectra (Biotage) employing ZIP sphere, SNAP Ultra and SNAP C18 cartridges. Nuclear magnetic resonance (NMR) spectra were recorded using an AVANCE500HD instrument (Bruker) with ^{1}H NMR spectra recorded at 500 MHz and ^{13}C NMR spectra recorded at 125 MHz using tetramethylsilane as an internal standard. Electrospray ionization (ESI) mass spectra were obtained using a LCT-Premier XE mass spectrometer (Waters) and an AccuTOF LC-plus 4G mass spectrometer (JEOL). Reverse-phase high-performance liquid chromatography (RP-HPLC) analyses were performed using an Inertsil ODS-3 column (4.6 × 250 mm; GL Sciences, Inc.) and an HPLC system comprised of a pump (PU-2080; JASCO) and UV detection (MD-2010 plus and FP-2020; JASCO). Preparative HPLC separations were performed using an Inertsil ODS-3 column (10.0 × 250 mm; GL Sciences, Inc.) and a HPLC system comprised of a pump (PU-2087; JASCO) and detector (UV-2075; JASCO). Buffer A was 50 mM triethylammonium acetate (TEAA) in H_2O; buffer B was acetonitrile (MeCN). Cytotoxicity assays were performed using PrestoBlue^{TM} cell viability reagent (Invitrogen).

UV-Vis Absorption and Fluorescence Spectroscopy

UV-vis absorption spectra (sample concentration: 2 or 5 μM in citrate-phosphate buffer) were recorded using a V-650 UV-VIS spectrometer (JASCO) at 37 °C. Fluorescence spectra (sample concentration: 0.2 or 0.5 μM in citrate-phosphate buffer, excitation at 492 nm) were measured using a Fluorescence Spectrophotometer F-7000 (Hitachi) at 37 °C, using a slit width of 5.0 nm for both excitation and emission and a photomultiplier voltage of 700 V. pH profiles were plotted over a pH range from 8.0 to 4.0. Fluorescence quantum yields were determined using fluorescein in 0.1 N NaOH as a standard (Φ = 0.85, excited at 492 nm). Citrate-phosphate buffer was prepared by mixing a 0.1 M solution of citric acid with a 0.1 M solution of Na_2HPO_4. pK_a values for absorption or emission maxima were calculated using curve fitting software based on the Henderson-Hasselbalch equation.

In vitro hydroxyapatite binding test

Hydroxyapatite (5 mg/mL) was vortexed in 1 μM aqueous solutions of pHocas-RIS or pHocas-AL-RIS (1 mL) for 30 min at room temperature. The resultant mixture was then centrifuged and washed two times with water and a portion of the resultant powder then soaked in citrate-phosphate buffer (400 μL) at various pH values (from pH 4.5 to 8.0). Fluorescence images were then acquired using a confocal laser scanning microscope (FLUOVIEW FV10i; Olympus) equipped with a 60× lens using an excitation wavelength of 492 nm, with emission spectra filtered through a 490-590 nm bandpass filter.

Cytotoxicity asay

RAW264.7 cells were re-plated into 96-well plates (1×10^4 cells/well) in DMEM containing 10% FBS and the cells then incubated overnight. The cells were then treated with the indicated concentrations of pHocas-RIS and pHocas-AL-RIS. After 24 h, PrestoBlue™ cell viability reagent was added and the cells further incubated according to the manufacture's guidelines. Cell viability was then calculated by measuring absorbances at 570 nm (experimental wavelength) and 600 nm (reference wavelength) using a M1000 microplate reader (Tecan).

In vitro osteoclast differentiation

Bone marrow progenitor cells were cultured with M-CSF (10 ng/mL) in minimal essential medium containing 10% fetal calf serum and bone marrow-derived macrophages (BMMs) collected after 2 days. Osteoclast differentiation was triggered by culturing the BMMs in minimal essential medium containing M-CSF (10 ng/mL) and RANKL (50

ng/mL) using the pHocas-RIS concentration levels indicated on the figure captions. The cells were then fixed and stained after four days using acid phosphatase and a leukocyte kit (Sigma), according to the manufacture's procedures.

Histological analysis

Histological analysis of bone tissue was performed using the Kawamoto film method according to the manufacturer's protocol. Dissected bone tissue from mice that had been administered pHocas-RIS were fixed with 4% paraformaldehyde (PFA) at 4 °C overnight. These samples were then embedded in super cryoembedding medium (Section-LAB Co. Ltd) and frozen, with the resultant frozen samples then sliced into 10 μm sections using a cryostat (CM3050; Leica) to control temperature. The treated bone slices were then soaked in citrate-phosphate buffer at various pH values (pH 4.0, 7.0, and 10.0) and fluorescence images then acquired using a multiphoton and confocal microscope (TCS-SP5; Leica Microsystems).

Two-photon imaging of bone samples using pHocas-AL-RIS and pHocas-RIS

All animal experiments were performed in compliance with the guidelines of the Animal Experimental Committee of Osaka University and approved by the 'Animal Care and Use Committee' of Osaka University (Approval number: 30-037-033). pHocas-AL-RIS or pHocas-RIS (5-10 mg/kg) dissolved in PBS was injected subcutaneously into 8-12-week-old male transgenic mice expressing tartrate-resistant acid phosphatase-(TRAP) promoter-driven tdTomato in their osteoclastsS4 daily for 3 days prior to recording images. Intravital imaging of mouse calvaria bone tissues was performed through modification of a previously described protocol. Mice were anesthetized with isoflurane (Escain; 2% (vol/vol) vaporized in 100% (vol/vol) oxygen), the frontoparietal regions of their skull bones exposed and their internal surfaces (adjacent to the bone marrow cavity) then imaged using a two-photon excitation microscopy. The imaging system employed was comprised of a multiphoton microscope (LSM 780 NLO; Carl Zeiss AG) using a laser (Chameleon Vision II Ti: Sapphire; Coherent Inc.) tuned to 940 nm and an upright microscope fitted with a 20× water immersion objective lens (W Plan-Apochromat, NA 1.0; Carl Zeiss). The imaging system employed for the bottom image in Fig 12a was a multiphoton microscope (A1-MP; Nikon) containing a laser (Chameleon Vision II Ti: Sapphire; Coherent Inc.) tuned to 940 nm and an upright microscope fitted with a 25× water immersion objective lens (APO, N.A. 1.1; Nikon). Fluorescence was detected by an external non-descanned detector (NDD; Nikon) using the following emission filters:

492/SP nm for the second harmonic generation (SHG), 525/50 nm for fluorescent probes. The microscope was enclosed in an environmental chamber that enabled anesthetized mice to be warmed using heated air.

Synthesis of compounds

Compound 1

Compound 1 was prepared via adaptation of a literature procedure.[35] Monosodium 1-hydroxy-2-(3-pyridyl) ethylidene-1,1-diphosphonate hemipentahydrate, (314 mg, 1.1 mmol) was dissolved in 9 mL water and the pH adjusted to 6.2 using 1 M NaOH. *tert*-Butyl (oxiran-2-ylmethyl) carbamate (270 mg, 1.6 mmol) in minimal MeOH was then added and the reaction mixture stirred at 40 °C for 24 h. The solvent was then removed in vacuo and the residue purified using a Biotage isolera Flash Purification System (silica-packed 30 g snap column) (solvent A: 50 mM aq. TEAA; solvent B: CH_3CN) to afford **1** (391 mg, 0.85 mmol, 77%) as a colorless solid. ^{1}H NMR (500 MHz, D_2O): δ 8.73 (s, 1H), 8.50 (d, J = 6.0 Hz, 1H), 8.47 (d, J = 8.0 Hz, 1H), 7.83 (dd, J = 8.0, 6.0 Hz, 1H), 4.30 (dd, J = 14.0, 10.0 Hz, 1H), 4.10-4.01 (m, 1H), 3.36-3.30 (m, 3H), 3.27 (d, J = 5.0 Hz, 1H), 3.19 (dd, J = 14.0, 5.0 Hz, 1H), 1.36 (s, 9H). ^{13}C NMR (125 MHz, D_2O): δ 158.2, 148.0, 145.7, 141.9, 140.0, 126.5, 81.3, 74.2, 73.2, 72.2, 70.0, 64.2, 27.6. MS (ESI^+): calcd for $[M]^+$ 457.11, found 457.10.

Compound 2

Compound **2** was prepared via adaptation of a literature procedure.[S1] Compound **1** (391 mg, 0.85 mmol) was dissolved in 5 mL water. 4 mL TFA was then added slowly and the solution stirred at rt for 3 h. The solvent was then removed in vacuo, and the resulting solids washed with ether, filtered, and dried, to afford **2** (446 mg, 1.25 mmol, quant.) as a colorless solid that was used without further purification. ^{1}H NMR (500 MHz, D_2O): δ 8.76 (s, 1H), 8.59 (d, J = 6.0 Hz, 1H), 8.50 (d, J = 8.0 Hz, 1H), 7.90 (dd, J = 8.0, 6.0 Hz, 1H), 4.77 (dd, J = 14.0, 3.0 Hz, 1H), 4.42 (dd, J = 14.0, 9.5 Hz, 1H), 4.31-4.27 (m, 1H), 3.41 (m, 2H), 3.30 (dd, J = 14.0, 3.0 Hz, 1H), 3.01 (dd, J =14.0, 9.5 Hz, 1H). ^{13}C NMR (125 MHz, D_2O): δ 148.0, 145.7, 141.9, 140.0, 126.5, 74.3, 73.2, 72.1, 69.5, 64.0. MS (ESI^+): calcd for $[M]^+$ 357.06, found 357.03.

Compound 3, 4 was prepared according to a literature procedure.[12]

Compound 5 (pHocas-RIS)

4-(4,6-dimethoxy-1,3,5-triazin-2-yl)-4-methylmorpholinium chloride (DMT-MM) (41.5 mg, 161 μmol) was added to a solution of compound **3** (20.0 mg, 40.2 μmol) in CH_3CN

(5.0 mL) and the reaction mixture stirred for 1 h. A solution of compound **2** (143 mg, 402 μmol) in aq. sodium carbonate/sodium bicarbonate buffer (pH 10.0, 2 mL) was then added and the reaction mixture stirred for 24 h, before the acetonitrile was removed under reduced pressure. The residue was then purified by reverse-phase HPLC (A/B = 20/80 (0 min), 50/50 (30 min) [solvent A: 50 mM aq. TEAA; solvent B: CH_3CN], flow rate: 4.7 mL/min) with the desired compound **5** eluting after 11 min. Lyophilization then afforded compound **5** as an orange powder (26.2 mg, 222 μmol, 55%). ^{1}H NMR (500 MHz, D_2O): δ 8.72 (s, 2H), 8.56 (d, *J* = 6.0 Hz, 2H), 8.47 (d, *J* = 8.0 Hz, 2H), 7.85 (dd, *J* = 6.0, 8.0 Hz, 2H), 7.73 (d, *J* = 8.0 Hz, 1H), 7.49 (d, *J* = 8.0 Hz, 1H), 7.48 (s, 1H), 4.76-4.74 (part. obscured by HDO, 2H), 4.36 (dd, *J* = 14.0, 9.5 Hz, 2H), 4.18-4.16 (m, 2H), 3.64 (q, 4H), 3.59 (dd, *J* = 14.0, 3.0 Hz, 2H), 3.39-3.35 (m, 6H), 2.51 (s, 6H), 2.43 (s, 3H), 1.43 (s, 3H), 1.03 (t, 6H). ^{13}C NMR (125 MHz, D_2O): δ 167.5, 155.2, 148.2, 145.8, 143.3, 142.7, 142.4, 138.7, 135.4, 134.0, 130.8, 128.3, 126.6, 119.8, 117.5, 115.1, 112.8, 77.3, 73.2 (t, *J* = 135 Hz), 69.2, 64.3, 42.5, 36.0, 17.3, 12.7, 12.5, 9.4. HRMS (ESI$^-$): calcd for $[M\text{-}3H]^-$, 1172.3074, found 1172.3062.

Compound 6 (pHocas-AL-RIS)

DMT-MM (55.4 mg, 197 μmol) was added to a solution of compound **4** (20.8 mg, 48.8 μmol) in CH_3CN (5.0 mL) and the reaction mixture stirred for 1 h. A solution of compound **2** (171 mg, 479 μmol) in aq. sodium carbonate/sodium bicarbonate buffer (pH 10.0, 2.5 mL) was added and the reaction mixture stirred for 24 h, with the acetonitrile then removed under reduced pressure. The residue was purified by reverse-phase HPLC (A/B = 20/80 (0 min), 50/50 (30 min) [solvent A: 50 mM aq. TEAA; solvent B: CH_3CN], flow rate: 4.7 mL/min) with the desired compound **6** eluting after 10 min. Lyophilization then afforded compound **6** as an orange powder (3.35 mg, 2.85 μmol, 4%). ^{1}H NMR (500 MHz, D_2O): δ 8.72 (s, 2H), 8.53 (d, *J* = 6.5 Hz, 2H), 8.47 (d, *J* = 8.5 Hz, 2H), 7.85 (dd, *J* = 6.5, 8.5 Hz, 2H), 7.33 (d, *J* = 8.0 Hz, 2H), 7.13 (d, *J* = 8.0 Hz, 2H), 4.75-4.65 (part. Obscured by HDO, 2H), 4.34 (dd, *J* = 14, 9.5 Hz, 2H), 4.35-4.16 (m, 2H), 3.59 (dd, *J* = 14, 4.0 Hz, 1H), 3.42-3.36 (m, 6H), 2.49 (s, 6H), 2.32 (s, 3H), 1.40 (s, 3H). ^{13}C NMR (125 MHz, D_2O): δ 167.6, 154.6, 148.2, 146.5, 145.8, 143.1, 142.2, 140.0, 139.2, 131.3, 130.2, 130.1, 127.9, 127.3, 126.5, 73.3 (t, *J* = 132 Hz), 69.4, 64.4, 42.5, 36.1, 23.0, 20.5, 12.7, 12.4. HRMS (ESI$^-$): calcd for $[M\text{-}3H]^-$, 1101.2339, found 1101.2355.

Reference

[19] A. G. Robling, L. F. Bonewald, *Annu. Rev. Physiol.* **2020**, *82*, 485–506.

[20] A. Vatsa, R. G. Breuls, C. M. Semeins, P. L. Salmon, T. H. Smit, J. Klein-Nulend, *Bone* **2008**, *43*, 452–458.

[21] G. Y. Rochefort, S. Pallu, C. L. Benhamou, *Osteoporos. Int* **2010**, *21*, 1457–1469.

[22] J. T. Compton, F. Y. Lee, *J. Bone Joint Surg. Am* **2014**, *96*, 1659–1668.

[23] K. D. Harrison, D. M. L. Cooper, *Front. Endocrinol.* **2015**, *6*, DOI 10.3389/fendo.2015.00122.

[24] S. L. Dallas and P.A.Veno, *Methods Mol. Biol.* **2012**, 816,425–457.

[25] H. Sano, J. Kikuta, M. Furuya, N. Kondo, N. Endo, M. Ishii, *Bone* **2015**, *74*, 134–139.

[26] E. Tsourdi, K. Jähn, M. Rauner, B. Busse, L. F. Bonewald, *J. Musculoskelet. Neuronal Interact.* **2018**, *18*, 292–303.

[27] N. K. Wittig, M. E. Birkbak, F. L. Bach-Gansmo, A. Pacureanu, M. H. Wendelboe, A. Brüel, J. S. Thomsen, H. Birkedal, *Calcif. Tissue. Int.* **2019**, *105*, 308–315.

[28] K. Jähn, S. Kelkar, H. Zhao, Y. Xie, L. A. M. Tiede-Lewis, V. Dusevich, S. L. Dallas, L. F. Bonewald, *J. Bone Miner. Res.* **2017**, *32*, 1761–1772.

[29] J. Kikuta, Y. Wada, T. Kowada, Z. Wang, G. H. Sun-Wada, I. Nishiyama, S. Mizukami, N. Maiya, H. Yasuda, A. Kumanogoh, K. Kikuchi, R. N. Germain, M. Ishii, *J. Clin. Investig.* **2013**, *123*, 866–873.

[30] M. Furuya, J. Kikuta, S. Fujimori, S. Seno, H. Maeda, M. Shirazaki, M. Uenaka, H. Mizuno, Y. Iwamoto, A. Morimoto, K. Hashimoto, T. Ito, Y. Isogai, M. Kashii, T. Kaito, S. Ohba, U. Il Chung, A. C. Lichtler, K. Kikuchi, H. Matsuda, H. Yoshikawa, M. Ishii, *Nat. Commun.* **2018**, *9*, DOI 10.1038/s41467-017-02541-w.

[31] R. G. G. Russell and M. J. Rogers, *Bone*, **1999**, *25*. 97–106.

[32] A. J. Roelofs, F. P. Coxon, F. H. Ebetino, M. W. Lundy, Z. J. Henneman, G. H. Nancollas, S. Sun, K. M. Blazewska, J. L. F. Bala, B. A. Kashemirov, A. B. Khalid, C. E. McKenna, M. J. Rogers, *J. Bone Miner. Res.* **2010**, *25*, 606–616.

[33] S. Sun, K. M. BŁazewska, A. P. Kadina, B. A. Kashemirov, X. Duan, J. T. Triffitt, J. E. Dunford, R. G. G. Russell, F. H. Ebetino, A. J. Roelofs, F. P. Coxon, M. W. Lundy, C. E. McKenna, *Bioconjug. Chem.* **2016**, *27*, 329–340.

[34] Y. Urano, D. Asanuma, Y. Hama, Y. Koyama, T. Barrett, M. Kamiya, T. Nagano, T. Watanabe, A. Hasegawa, P. L. Choyke, H. Kobayashi, *Nat. Med.* **2009**, *15*, 104–109.

[35] B. A. Kashemirov, J. L. F. Bala, X. Chen, F. H. Ebetino, Z. Xia, R. G. G. Russell, F. P. Coxon, A. J. Roelofs, M. J. Rogers, C. E. McKenna, *Bioconjug. Chem.* **2008**, *19*, 2308–2310.

Chapter 2

Efficient Visible/NIR Light-driven Uncaging of Hydroxylated Thiazole Orange-based Caged Compounds in Aqueous Media

Introduction

Caged compounds are powerful tools for non-invasive spatial and temporal control of bioactivity and are produced by incorporating photoremovable protecting groups (PPGs) into the structure of bioactive compounds.[36] Illumination of the caged compounds leads to the immediate release of biomolecules and activation of their biofunctions. Therefore, light-induced cargo release technology has gained attention in the fields of chemical biology, photoactivated chemotherapy, and neuroscience.[37,38] As biologically useful caged compounds, they should be soluble and stable in aqueous solution and undergo efficient photorelease. Although conventional PPGs such as *o*-nitrobenzyl or coumarin-4-ylmethyl group meet those conditions,[36] they require high-energy UV-light illumination, leading to cellular damage or death at a low tissue penetration depth. Recently, limited numbers of visible-light-sensitive PPGs (>450 nm) based on ruthenium complexes,[39] boron dipyrromethene (BODIPY) derivatives,[40–43] or cyanine dyes[17,44,45] have been reported.[46] However, most of them suffer from low water solubility, which limits their manipulation in biological systems. Moreover, their photolytic efficiencies (uncaging efficiencies) were measured in organic solvents, which could have affected the uncaging of biomolecules under physiological conditions. While some BODIPY-based PPGs displayed improved water solubility,[47] their uncaging cross sections and water solubility were still low ($\varepsilon\Phi \approx 3$–$24$ in CH_3CN/water (7/3)). Compared with one-photon excitation (1PE), two-photon excitation (2PE) with near-infrared (NIR) light provides deeper tissue penetration, diminished phototoxicity, and high 3D resolution.[48,49] Most 2PE-sensitive PPGs are activated by 740–800 nm light since they absorb UV/blue light whereas only a few 2PE-sensitive caged compounds[50] are active at longer than 900 nm. Uncaging with long-wavelength two-photon light enables an extra level of spatial and temporal control in the deeper tissue. Although the optical control with long-wavelength light is highly demanded for a wide range of biological applications such as control of neural activity in neuroscience and drug release in photoactivated chemotherapy, the development of visible/NIR light-sensitive PPGs with high photolytic efficiency in aqueous solution is still highly challenging.

Here, the author presents new visible/NIR light-sensitive PPGs for caged compounds with high photolytic efficiency in aqueous solution. The author developed hydroxylated

thiazole orange dye-based PPGs (HTO) which absorb visible green light (**Figure 14**). Caged compounds with HTO-based PPGs were efficiently uncaged by green-light illumination under physiological conditions and were stable under dark conditions. In addition, 2PE photolysis reactions of HTO-caged glutamate (Sul-HTO-Glu) were achieved using an NIR laser (940 nm).

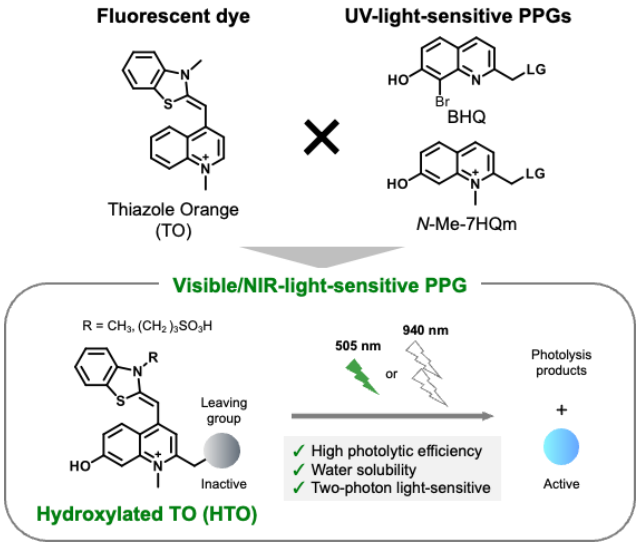

Figure 14. Design of hydroxylated TO (HTO)-based PPGs.

Results and Discussion

Design, Synthesis, and Photochemical Properties of HTO-caged Compounds

Scheme 2. Synthesis of HTO-OAc.

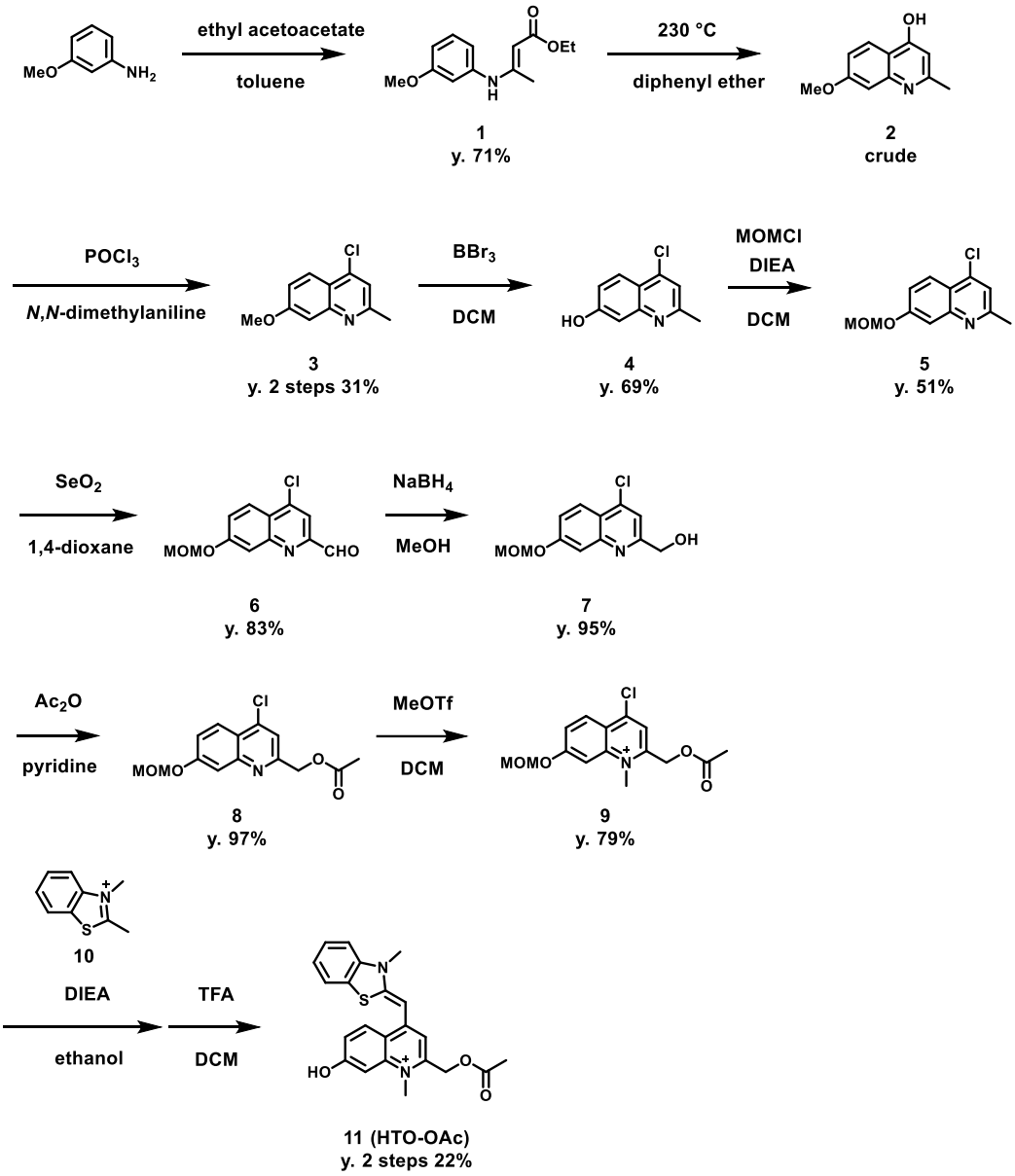

Scheme 3. Synthesis of HTO-OPip.

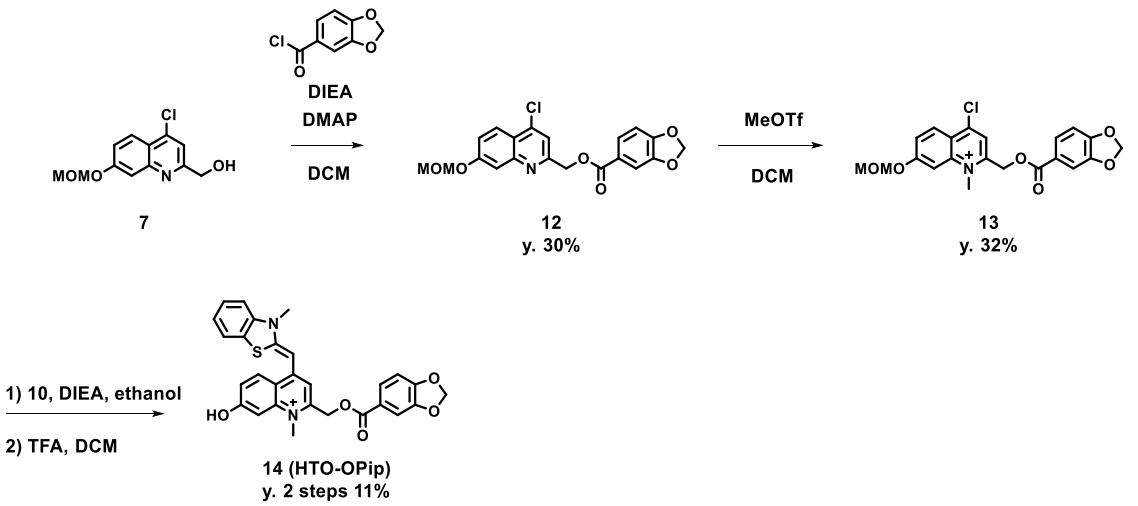

Visible-light-sensitive PPGs were designed based on hydroxylated thiazole orange (HTO) using thiazole orange (TO) as the molecular framework of the chromophore (**Figure 14**). TO absorbs visible green light with a high absorption coefficient and is used as a fluorescent dye for nucleic acid staining.[51] In addition, this dye contains a quinoline/*N*-methylquinolinium moiety that serves as a scaffold for UV light-sensitive PPGs.[52–55] Photo-induced deprotonation of the 7-hydroxyl group of the quinoline-based PPGs accelerates the intramolecular charge transfer in the excited state, resulting in bond dissociation at the 2-methyl position with a high quantum efficiency of 1PE and 2PE.[14,56] Although 7-hydroxyl-quinoline-based PPGs are photolyzed with high photolytic efficiencies to 1PE and 2PE, they have low molar absorption coefficients in short-wavelength regions (365 nm for 1PE or 740 nm for 2PE).[55] In contrast, in our molecular design of HTO, a 7-hydroxyl-quinoline-based PPG is incorporated into TO that has a high absorption coefficient in a visible light region. Furthermore, hydrophilic groups can be introduced into the HTO scaffold, which improves its water solubility. Thus, the author reasoned that HTO-based PPG would enable visible-light uncaging with a high photolytic efficiency in aqueous solution. Photoactivation of HTO by green light was assessed using synthetic model caged compounds bearing acetic acid (HTO-OAc) and piperonylic acid (HTO-OPip) as leaving groups (**Figure 15**). Methoxymethyl (MOM)-protected 7-hydroxyquinoline derivatives were conjugated with leaving groups, followed by *N*-

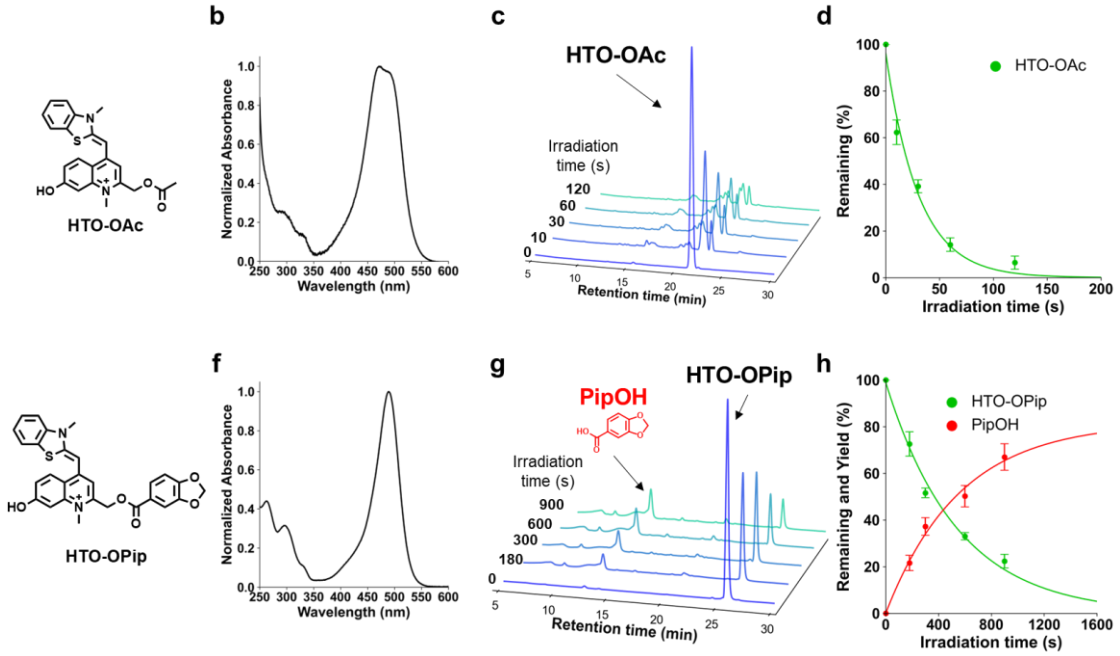

Figure 15. The photochemical reaction of HTO-caged compounds. (a) Chemical structure of HTO-OAc. (b) Normalized absorption spectrum of 10 μM HTO-OAc at 25°C in pH 7.4 PBS buffer (10% DMSO). (c) HPLC time courses of photolysis of HTO-OAc at 500 nm. Conditions: 100 μM HTO-OAc in PBS buffer (10% DMSO), Light intensity: 10 mW/cm^2, λ_{ex} = 490 ± 5 nm. (d) Quantitative monitoring of the photolysis reaction of HTO-OAc. Error bars represent the SD (N = 3). (e) Chemical structure of HTO-OPip. (f) Normalized absorption spectrum of 10 μM HTO-OPip at 25°C in pH 7.4 PBS buffer/CH_3CN = 1/1 (3% DMSO). (g) HPLC time courses of photolysis of HTO-OPip at 254 nm. Conditions: 100 μM HTO-OPip in pH 7.4 PBS buffer/CH_3CN = 1/1 (3% DMSO), Light intensity: 10 mW/cm^2, λ_{ex} = 490 ± 5 nm. Error bars represent the SD (N = 3). (h) Quantitative monitoring of the photolysis reaction of HTO-OPip. Error bars represent the SD (N = 3).

alkylation. After the formation of TO analogs with 2,3-dimethylbenzo[*d*]thiazol-3-ium, the target compounds were obtained by deprotection of MOM groups (**Scheme 2, 3**).

The time courses for the one-photon photolysis reactions of HTO-OAc or HTO-OPip with internal standards were monitored by HPLC analysis (**Figure 15**). Illumination of HTO-OAc in aqueous solution with green light led to rapid degradation of HTO-OAc (**Figure 15c, d**). In the case of HTO-OPip, the released product, piperonylic acid, was detected by HPLC after green light illumination (in PBS buffer/MeCN = 1:1, 3% DMSO) (**Figure 15g**). Illumination of HTO-OPip resulted in an 80% theoretical yield of piperonylic acid (**Figure 15h**). However, HTO-OPip showed slower degradation than HTO-OAc. This result indicates the solvent dependency of uncaging of HTO derivatives and is consistent

with the effects observed when an aprotic polar solvent (acetonitrile) was used with quinoline-based PPGs.[56]

HTO-caged Glutamate

Next, the author developed HTO-caged glutamate for activation of neurotransmitters with visible/NIR light. UV-light and two-photon activatable caged glutamates have been widely used in neuroscience to control neuronal activity.[57] However, no caged glutamate that undergoes one-photon uncaging with longer-wavelength light (>500 nm) exists. For two-photon uncaging, only DEAC450 has been reported to be a two-photon-activatable caged glutamate at ~900 nm.[50] The author assumed that the rapid degradation of HTO by green light was suitable for the development of long wavelength-light sensitive caged glutamate. Therefore, the author designed HTO-caged glutamate (Sul-HTO-Glu) (**Scheme 4**). In the molecular design of Sul-HTO-Glu, a sulfonic acid is introduced from the benzothiazole nitrogen of the HTO scaffold, which can enhance the water solubility.

Scheme 4. Synthesis of Sul-HTO-Glu.

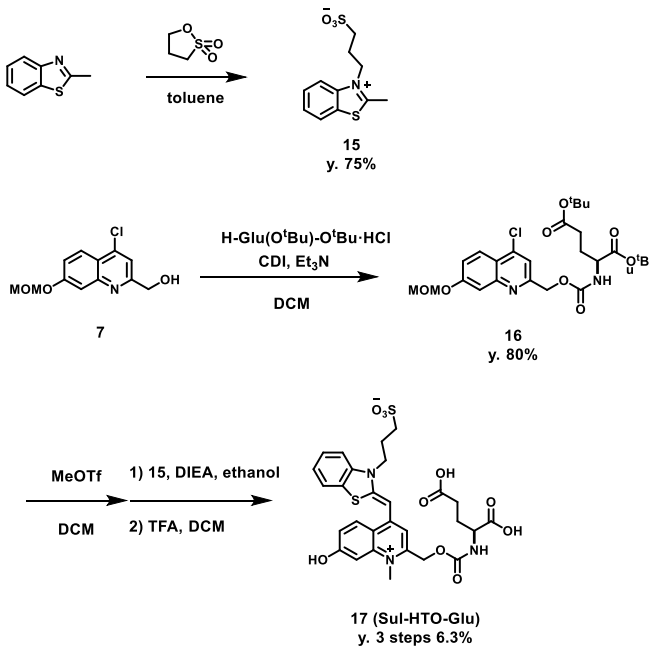

As expected, Sul-HTO-Glu did not aggregate, even in PBS buffer containing 0.1% DMSO (**Figure 16b**). Illumination of Sul-HTO-Glu in aqueous solution with green light led to rapid degradation of Sul-HTO-Glu (**Figure 16c**). Glutamate was released at a

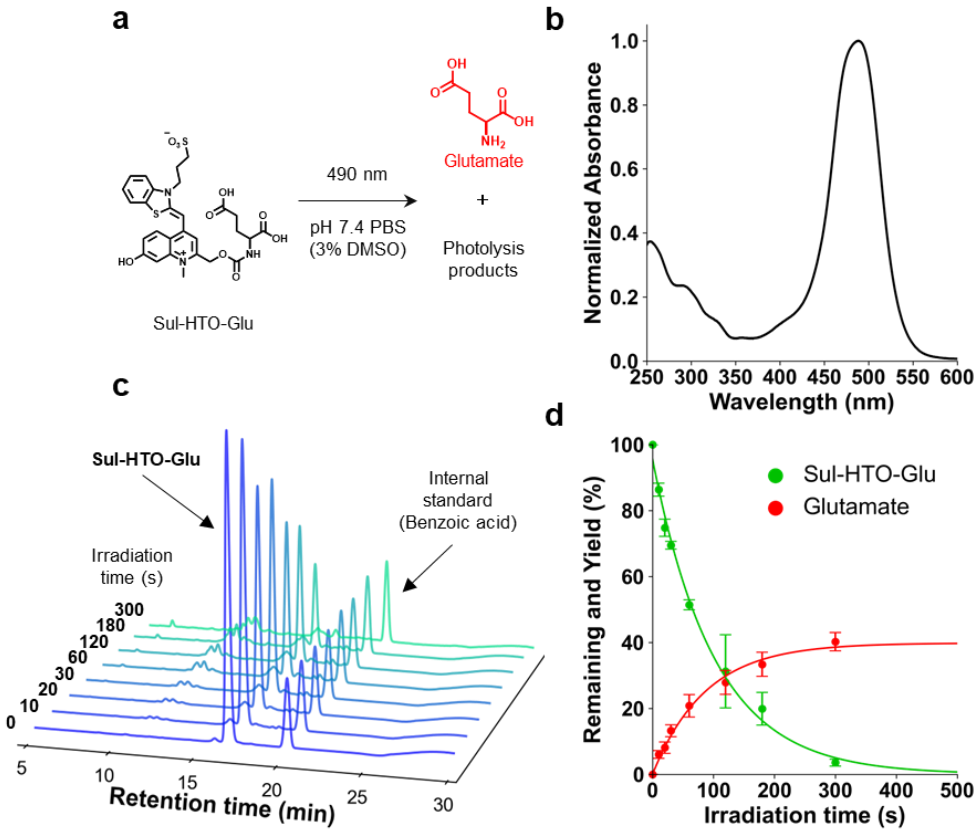

Figure 16. Photolysis of Sul-HTO-Glu with 1PE. (a) Light-induced glutamate release from Sul-HTO-Glu. (b) Normalized absorption spectrum of 10 μM Sul-HTO-Glu at 25°C in PBS buffer containing 0.1% DMSO (pH 7.4). (c) HPLC time courses of photolysis of Sul-HTO-Glu at 254 nm. Conditions: 50 μM Sul-HTO-Glu and 300 μM benzoic acid as an internal standard in PBS buffer containing 3% DMSO (pH 7.4). Light intensity = 10 mW/cm^2, λ = 490 ± 5 nm. (d) Quantitative monitoring of the reaction of Sul-HTO-Glu. Error bars represent the SD (N = 3).

maximum yield of 40%, likely due to a photoinduced side reaction, although this has not been confirmed (**Figure 16d**).

Spectroscopic and Photochemical Properties of HTO-caged Compounds

Table 1. Spectroscopic and photochemical properties of HTO-caged compounds. [a]PBS buffer (10% DMSO). [b]PBS buffer:CH_3CN = 1:1 (3% DMSO). [c]PBS buffer (3% DMSO)

compound	λ_{max} (nm)	ε ($M^{-1}cm^{-1}$)	t_{90} (s)	Φ	$\varepsilon \cdot \Phi$
HTO-OAc[a]	493	43000	69	8.6×10^{-3}	370
HTO-OPip[b]	490	50000	1239	3.8×10^{-4}	19
Sul-HTO-Glu[c]	488	49000	231	2.3×10^{-3}	110

The molar absorption coefficients (ε), photolysis quantum yields (Φ), and photolytic efficiencies (εΦ) are summarized in **Table 1**. The photolytic efficiency of HTO-OAc in aqueous solution was 370. This value is approximately five times higher than the BODIPY-core PPG (εΦ = 70 in methanol) bearing the same leaving group (acetic acid).[42] The high photolytic efficiency was attributed to higher Φ values for HTO-OAc compared with BODIPY-based PPGs (Φ = 4–24 $\times 10^{-4}$ in methanol) while the ε values are in the same order of magnitude. The photolytic efficiency of Sul-HTO-Glu in aqueous solution was 110, which was sufficiently high for spatiotemporal control of neurotransmitters. Moreover, this value (εΦ = 110) is much higher than those of other visible-light-sensitive caged compounds (εΦ = < 50) at ~550 nm-wavelength light containing bioactive compound.[41] This result indicates that HTO-caged compounds have superior properties for spatial and temporal control of biological functions compared to those with BODIPY-based visible-light-sensitive PPGs. Importantly, HTO-OAc, HTO-OPip, and Sul-HTO-Glu showed no hydrolysis for 24 h under dark conditions (**Figure 17**).

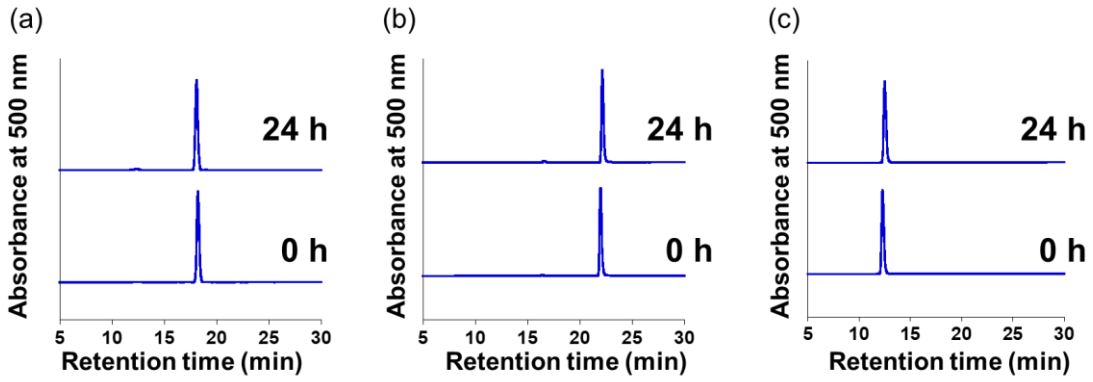

Figure 17. The stability of the caged HTO solutions kept in the dark. No changes were found in the chromatograms recorded after 24 h. (a) HTO-OAc (50 μM) in PBS containing 10% DMSO (pH 7.4), Buffer A: 0.1% TFA in H_2O, Buffer B: 0.1% TFA in CH_3CN, Buffer A/B ratio (%): 75/25 (0 min), 30/70 (30 min). (b) HTO-OPip (50 μM) in PBS buffer:acetonitrile (1:1) containing 3% DMSO (pH 7.4), buffer A: 0.1% HCOOH in H_2O, buffer B: 0.1% HCOOH in CH_3CN, buffer A/B ratio (%): 75/25 (0 min), 30/70 (30 min). (c) Sul-HTO-Glu (50 μM) in PBS containing 0.1% DMSO (pH 7.4), buffer A: 0.1% TFA in H_2O, buffer B: 0.1% TFA in CH_3CN, buffer A/B ratio (%): 80/20 (0 min), 50/50 (30 min).

Investigation of The Photolysis Reaction Mechanism

The mechanism of the photolysis reaction of HTO was investigated. The photodegradation of BHQ PPG involves deprotonation of the 7-hydroxy group in the triplet- or singlet-excited state and leads to heterolysis of the C−O bond to generate an ion pair that subsequently collapses into the free leaving group and a solvent-captured side product.[14,56] This deprotonation proceeds in aqueous buffer rather than aprotic polar

solvents. Thus, the author compared the photolysis of Sul-HTO-Glu in buffer containing polar aprotic acetonitrile solvent by monitoring the absorption. Under illumination, the author found a decrease in the absorption of Sul-HTO-Glu at around 490 nm in PBS buffer, corresponding with the results of HPLC analysis (**Figure 16c**). In contrast, the author found that photolysis of Sul-HTO-Glu was significantly reduced in the presence of 50% acetonitrile in PBS buffer (**Figure 18a**), indicating that deprotonation is involved in HTO photodegradation. Moreover, there were no significant differences in the photodegradation kinetics between non-degassed and degassed samples (**Figure 18b-d**), indicating that molecular oxygen did not influence the HTO photochemical reaction, unlike cyanine (Cy7)-based PPGs.[17,45]

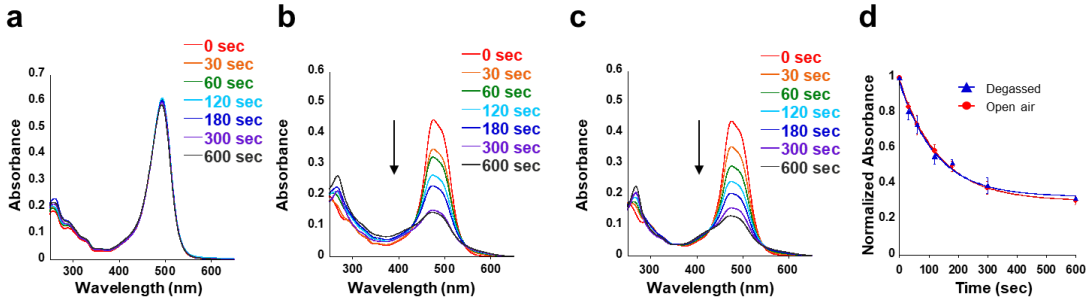

Figure 18. Absorption spectra of 10 μM Sul-HTO-Glu at 25 ºC after exposure to 490 nm light. Light intensity = 10 mW/cm^2, λ = 490 ± 5 nm. (a) In 1:1 PBS buffer/MeCN containing 0.1% DMSO (pH 7.4). (b) Degassed solution (pH 7.4 PBS buffer containing 0.1% DMSO). The samples were degassed using a freeze-pump-thaw technique (three cycles). (c) Open air solution (pH 7.4 PBS buffer containing 0.1% DMSO). (d) Absorbance traces at 490 nm. Blue: degassed solution. Red: open air solution. Data are presented as means ± SD (N = 3).

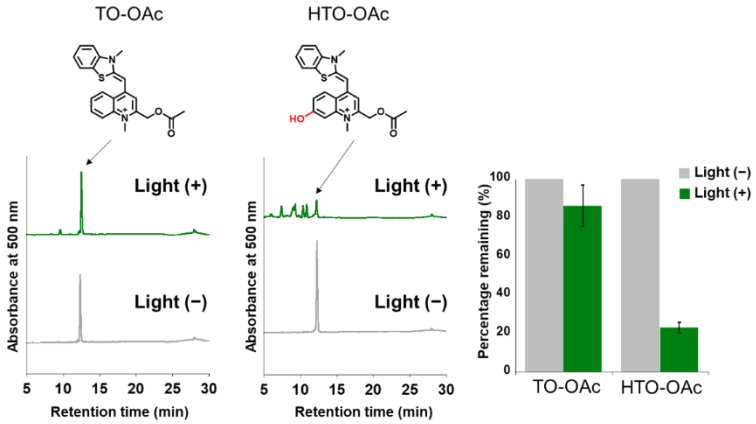

Figure 19. Illumination of TO-OAc and HTO-OAc. Column: Inertsil® ODS3, buffer A: 0.1% HCOOH in H_2O, buffer B: 0.1% HCOOH in CH_3CN, buffer A/B ratio (%): 75/25 (0 min), 30/70 (30 min). Light: λ = 490 ± 5 nm, 10 mW/cm^2, 120 s. Data are presented as means ± SD (N = 3).

To further examine the role of the hydroxy group in the HTO scaffold, the author synthesized TO-OAc, which lacks a hydroxy group in the quinoline ring. Illumination of TO-OAc led to reduced consumption of TO-OAc versus HTO-OAc (**Figure 19**). This

result indicates that the hydroxy group in HTO plays an important role in photochemical efficiency, as well as with BHQ and *N*-me-7HQm PPGs.

In addition, the photocleavage product containing ^{18}O (HTO-^{18}OH, m/z 353) was detected in the product mixtures after photolysis of HTO-OAc in ^{18}O-labeled water (**Figure 20**). These results indicate that photolysis generated a solvent-captured side product via heterolysis of the C−O bond. These results inferred that photodegradation of HTO resulted from the same photolysis mechanism as that with quinoline/quinolinium-based PPGs.

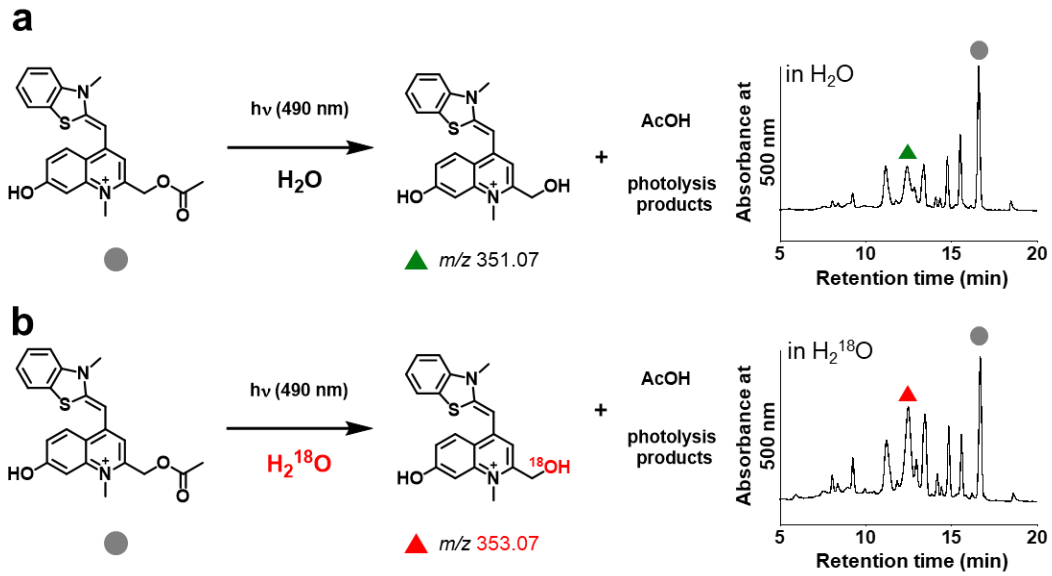

Figure 20. Oxygen-18 labeling experiment through photolysis of 100 µM HTO-OAc in (a) H_2O containing 10% DMSO and in (b) $H_2{}^{18}O$ (97% labelled) containing 10% DMSO. Light intensity = 10 mW/cm^2, λ = 490 ± 5 nm.

Activation of NMDA Receptors by Sul-HTO-Glu with Green Light

Figure 21. Oocyte membrane current response to 10 μM glycine (left) and 100 μM glutamate/10 μM glycine (right) treatments in a bath solution (pH 7.3).

To confirm the utility of these new green light-sensitive HTOs in the biological setting, the author attempted optical control of NMDARs in *Xenopus* oocytes and HEK293T cells using Sul-HTO-Glu. NMDARs are glutamate-gated ion channels that play important roles in learning and memory and may also be involved in various neurological and psychiatric disorders.[58] The binding of glutamate to the GluN2 subunits is required for full activation (**Figure 21**). The author tested whether illumination of Sul-HTO-Glu could release glutamate under biological conditions and activate an ionic current by opening NMDAR channels (**Figure 23a**). Ionic currents were recorded from *Xenopus* oocytes expressing NMDARs using a two-electrode voltage clamp. As expected, illumination of NMDAR-expressing oocytes in the absence of Sul-HTO-Glu did not activate a current (**Figure 22**). On the other hand, following a 10 s waiting period after preapplication of Sul-HTO-Glu, 10 s illumination of the NMDAR-expressing oocytes using a 505 nm LED immediately evoked an inward current (**Figure 23b**). Owing to its high water solubility and photolytic efficiency, Sul-HTO-Glu achieved long-wavelength light activation with fast kinetics which is necessary for controlling neural activities. Ca^{2+} influx via NMDARs was also observed in HEK293T cells using a red fluorescent Ca^{2+} indicator, Calbryte590. The calcium response was monitored on uncaging after HEK293T cells were loaded with Sul-HTO-Glu and glycine in the presence of Calbryte 590. A 10 s illumination using a 505 nm LED successfully evoked Ca^{2+} influx (**Figure 23c bottom row, Figure 23d**). On

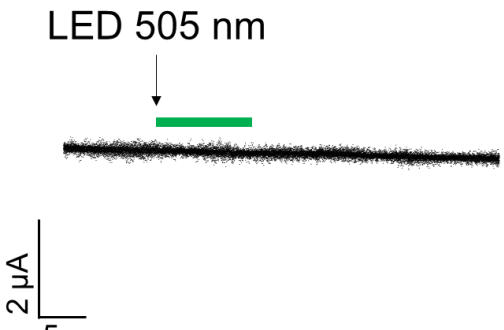

Figure 22. Oocyte membrane current in the absence of Sul-HTO-Glu and glycine. Light intensity = 30 mW/cm^2, λ = 505 nm. Light irradiation for 10 s.

the other hand, the no-light condition did not evoke a Ca^{2+} response (**Figure 23c top row, Figure 23d**). Moreover, the fluorescence of Sul-HTO-Glu was not observed either inside or outside non-transfected HEK293T cells when excited at 473 nm (**Figure 23e**). Importantly, Sul-HTO-Glu and the side products of illumination exhibited no cytotoxicity toward cultured HEK293T cells (**Figure 23f**).

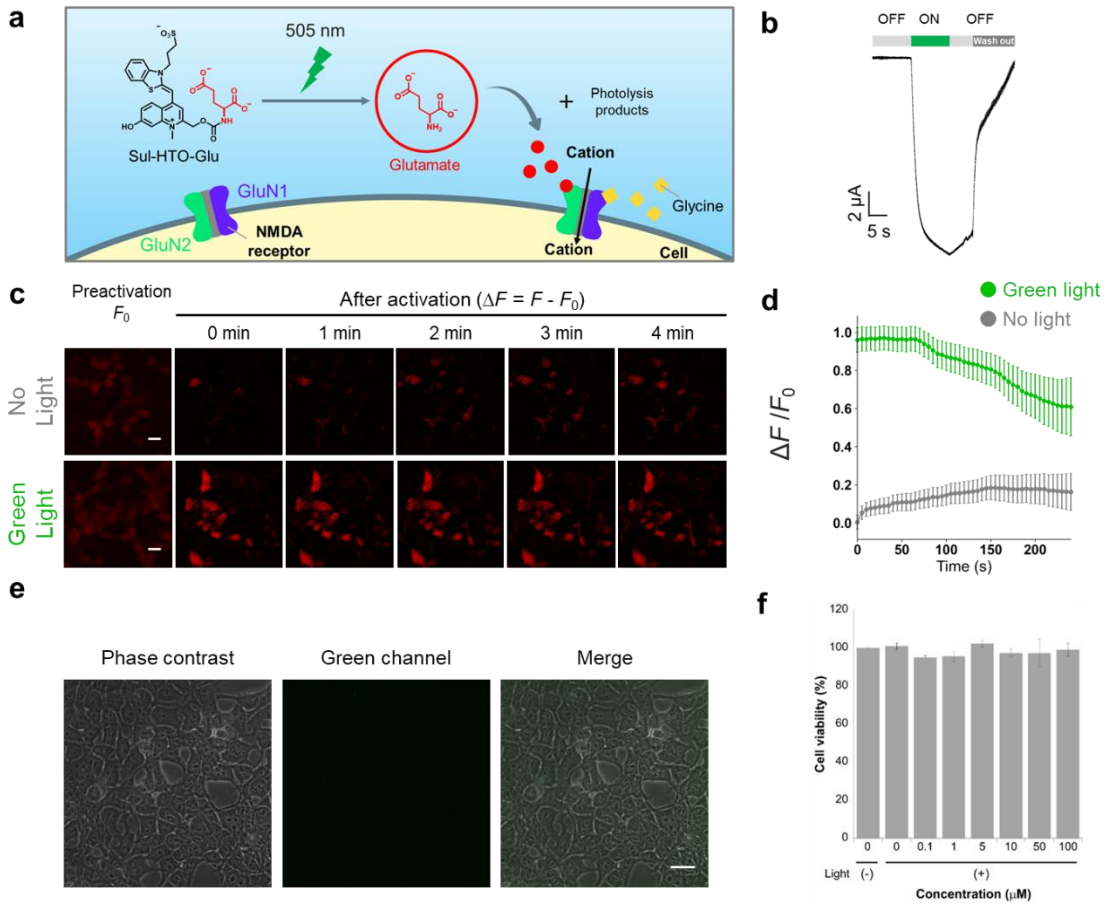

Figure 23. Uncaging experiment of Sul-HTO-Glu in *Xenopus* oocytes and HEK293T cells. (a) The glutamate released from Sul-HTO-Glu by green light illumination binds to GluN2, which results in channel opening. (b) Release of the glutamate to activate NMDARs in *Xenopus* oocytes upon green light photolysis with 100 μM Sul-HTO-Glu and 10 μM glycine in the pH 7.3 bath solution. Uncaging light was provided for 10 s (green bar). (c) Time lapse imaging of a red fluorescent Ca^{2+} indicator (Calbryte 590) with 559 nm excitation in HEK293T cells. Glutamate was uncaged upon green light photolysis with 25 μM Sul-HTO-Glu and 50 μM glycine (0.25% DMSO). Scale bar: 20 μm. (d) The fluorescence change after uncaging of glutamate. The fluorescence intensity was captured every 5 s. Error bars represent SEM, n = 30 cells from two independent experiments. (e) Confocal images of Sul-HTO-Glu (25 μM) with 473 nm excitation in HEK293T cells. Scale bar: 20 μm. (f) Cytotoxicity results for Sul-HTO-Glu at varying concentrations (0–100 μM) in HEK293T cells. Light = 30 mW/cm^2, Illumination period = 10 s. Error bars represent the SD (N = 3).

2PE Photolysis

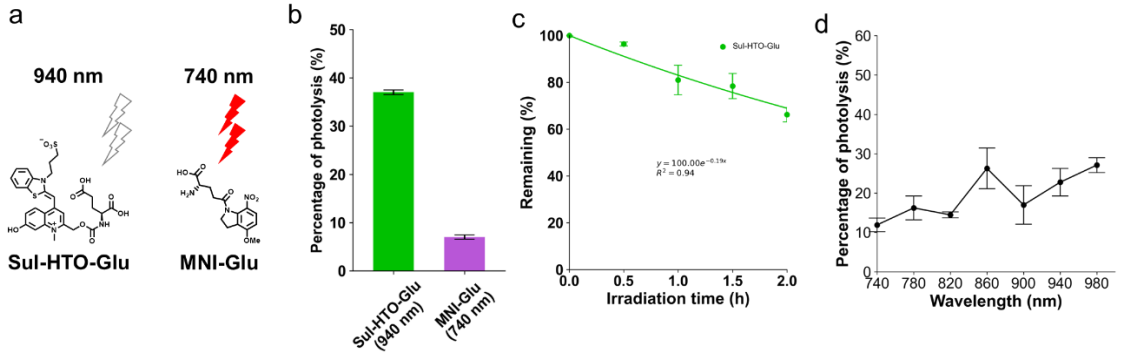

Figure 24. Photolysis of Sul-HTO-Glu or MNI-Glu with 2PE. (a)Sul-HTO-Glu and 2PE (740 nm) sensitive caged glutamate (MNI-Glu). (b) The percentages of Sul-HTO-Glu and MNI-Glu photolysis after 2PE for 1 h (Sul-HTO-Glu: 150 mW, λ_{ex} = 940 nm, MNI-Glu: 200 mW, λ_{ex} = 740 nm). Error bars represent the SD (N = 3). (c) Time courses of 2PE photolysis of Sul-HTO-Glu (Ti:sapphire laser). Condition: 50 µM Sul-HTO-Glu and 300 µM benzoic acid in pH 7.4 PBS buffer (3% DMSO). Light: 150 mW, λ_{ex} = 940 nm. The percentage remaining was determined by HPLC and is the average of 3 runs. (d) Wavelength-selective 2PE photolysis of Sul-HTO-Glu (Ti:sapphire laser). Condition: 50 µM Sul-HTO-Glu and 300 µM benzoic acid in pH 7.4 PBS buffer (3% DMSO). Light: 100 mW, 2h. The percentage of photolysis was determined by HPLC and is the average of 3 runs.

1PE uncaging using visible/NIR light can be replaced by 2PE uncaging with NIR light. To investigate the 2PE sensitivities of HTO-caged compounds, 2PE photolysis reactions with Sul-HTO-Glu were performed using a mode-locked Ti:sapphire laser and monitored by HPLC. The 2PE photolysis of Sul-HTO-Glu was evaluated by comparing 2PE photolysis with commercially available MNI-Glu at 740 nm (**Figure 24a**). Illumination of Sul-HTO-Glu at 940 nm for 1 h resulted in 37% of photolysis (**Figure 24b**). The percentage of MNI-Glu photolysis with 2PE was only 7% (**Figure 24b**). This result implies that Sul-HTO-Glu is more sensitive to 2PE than MNI-Glu despite using a longer wavelength for 2PE. The time courses and the wavelength-selective 2PE photolysis of Sul-HTO-Glu were shown in **Figure 24c**, **d**. The percentage of the remaining of Sul-HTO-Glu was decreased as irradiation time went on. The wavelength-selective 2PE photolysis revealed that there are two peaks of two-photon absorption around 860 nm and 980 nm.

Finally, the author tried single-spine stimulation by 2PE uncaging of Sul-HTO-Glu. 50 µM Sul-HTO-Glu was bath-applied to cultured hippocampal slices whose CA1 pyramidal neurons were transfected by injecting adeno-associated viral vector (AAV) encoding Clover, which is one of the brightest fluorescent proteins. The Clover fluorescence of spines was monitored by 2PE at 1000 nm, 1.2 mW and uncaged glutamate by 980 nm 2PE laser (4 mW). In this condition, only the volume of the stimulated spine increased after two-photon pulse irradiation (**Figure 25a**). The enlargement of adjacent spines did

not occur (**Figure 25b**). This result shows that the 2PE uncaging of Sul-HTO-Glu can activate and stimulate a single spine with high spatiotemporal resolution.

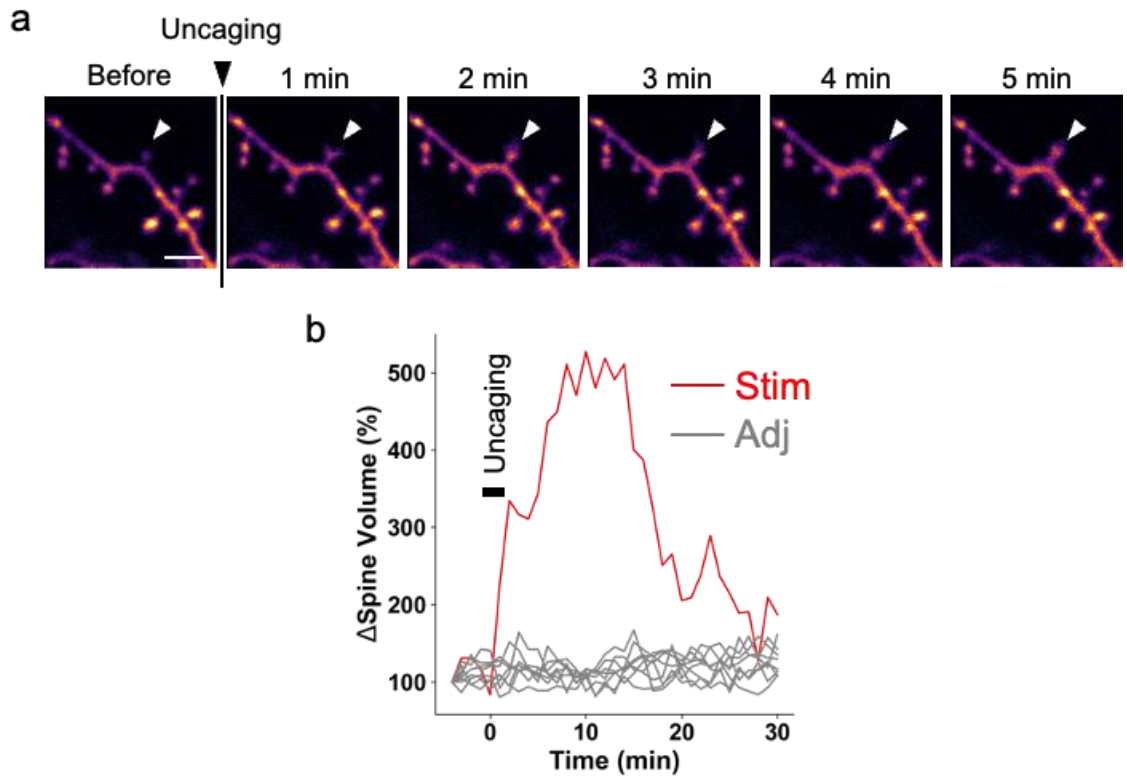

Figure 25. (a) A hippocampal CA1 neuron expressing Clover was observed by two-photon excitation at 1000 nm (1.2 mW), and Sul-HTO-Glu (50 μM) was activated at 980 nm (4 mW, duration/pulse 6 ms, 30 trains) in a spine indicated by a white arrow. Observation buffer with 4 mM $CaCl_2$,1 μM TTX in 4 mL. Scale bar: 3 μm. (b) Time course of the change in spine volume in the stimulated spine (Stim) and adjacent spines (Adj).

Experimental Methods

General

All reagents were purchased from Tokyo Chemical Industries, Wako Pure Chemical, or Sigma-Aldrich Chemical Co. and were used without further purification. Analytical thin-layer chromatography was performed on 60F254 silica plates (Merck & Co., Inc.) and visualized under UV light. Flash auto purification was conducted using the Isolera Spectra (Biotage) employing ZIP sphere, SNAP Ultra, and SNAP C18 cartridges. NMR spectra were recorded using an AVANCE500HD instrument (Bruker), with ^{1}H NMR spectra recorded at 500 MHz and ^{13}C NMR spectra recorded at 125 MHz using tetramethylsilane as an internal standard. FAB mass spectra were acquired using a JMS-700 mass spectrometer (JEOL), while electrospray ionization mass spectra were obtained using an

LCT-Premier XE mass spectrometer (Waters). Reversed-phase HPLC analyses were performed using an Inertsil ODS-3 column (4.6 × 250 mm; GL Sciences, Inc.) and an HPLC system comprising a pump (PU-2080 [JASCO] or Chromaster® 5110 [HITACHI]) and detector (MD-2010 plus and FP-2020 [JASCO] or Chromaster® 5430 and Chromaster® 5440 [HITACHI]). The sample injections were performed using an autosampler (AS-4550 [JASCO] or Chromaster® 5210 [HITACHI]). Preparative HPLC separations were performed using an Inertsil ODS-3 column (10.0 × 250 mm; GL Sciences, Inc.) and an HPLC system comprising a pump (PU-2087; JASCO) and detector (UV-2075; JASCO). Buffer A was composed of 0.1% TFA in H_2O or 0.1% HCOOH in H_2O, and buffer B was composed of 0.1% TFA in acetonitrile or 0.1% HCOOH in acetonitrile.

UV-Vis absorption spectroscopy

The absorption spectra of HTO-OAc (10 μM) were measured in PBS buffer (pH 7.4) containing 10% DMSO at 25 ºC. The absorption spectra of HTO-OPip (10 μM) were measured in a 1:1 (v/v) PBS/CH_3CN mixture containing 0.3% DMSO at 25ºC (pH 7.4). The absorption spectra of Sul-HTO-Glu (10 μM) were measured in PBS (pH 7.4) containing 0.1% DMSO at 25 ºC.

One-photon uncaging and photochemical quantum yield determination

The photon flux of the lamp (*I)* was determined using ferrioxalate actinometry.[59] The solution contained 1.0 mL 0.1 M $K_3[Fe(C_2O_4)_3]\cdot 3H_2O$ in 0.1 N sulfuric acid and was prepared in a dark room using a red light. Irradiation was conducted using a Xe lamp (λ_{ex} = 490 ± 5 nm). Samples in HPLC vials were irradiated for 0, 10, 20, or 30 s, and 0.250 mL of each sample was immediately transferred to a 10-mL volumetric flask, followed by the addition of 0.5 mL buffer stock solution (8.2 g NaOAc, 1 mL conc. H_2SO_4, 100 mL water), 4 mL 0.1% 1,10-phenanthroline solution in water, and water to a final volume of 10 mL. After at least 1 h in the dark, 0.2 mL of each sample was transferred to a cuvette, and the absorbance was measured at 510 nm. The photon flux (I einstein$\cdot s^{-1}\cdot cm^{-2}$) was determined using the following equations:

$$I = \frac{\Delta n}{\Phi_\lambda \cdot S \cdot t} \cdot \frac{1}{1-10^{-A\prime}} \quad \text{(Eq. 1)}$$

$$\Delta n = \frac{V_1 \cdot V_3 \cdot 10^{-3}}{V_2} \cdot \frac{\Delta A}{\varepsilon_{510} \cdot l} \quad \text{(Eq. 2)}$$

I : Photon flux (einstein·s^{-1}·cm^{-2})
Δn : Fe^{2+} photogenerated (mol)
Φ_λ : Photochemical quantum yield of the actinometer at a given wavelength
S : Irradiated area (cm^2)
t : Irradiation time (s)
A' : Absorbance of the actinometer at the irradiation wavelength
V_1 : Volume of the irradiated sample (mL)
V_2 : Volume of the transferred irradiated sample (mL)
V_3 : Volume of the volumetric flask containing the buffer and phenanthroline (mL)
ΔA : Difference in absorbance from the 0 s (dark) experiment
ε_{510} : Absorption coefficient of the complex (11100 L mol^{-1} cm^{-1})
l : Optical pathlength of the cuvette (cm)

Table S1. Solvent conditions and internal standards.

Compounds	Solvent	Internal standard
HTO-OAc	PBS buffer (10% DMSO, pH 7.4)	methyl 3-hydroxy-2-naphthoate
HTO-OPip	PBS buffer/acetonitrile = 1:1(3% DMSO, pH 7.4)	methyl 3-hydroxy-2-naphthoate
Sul-HTO-Glu	PBS buffer (3% DMSO, pH 7.4)	benzoic acid

The photochemical quantum yields were obtained using HPLC time-course experiments. HTO compounds and internal standards were irradiated using a Xe lamp (light intensity: 10 mW/cm^2, λ_{ex} = 490 ± 5 nm) in solution (**Table S1**) at room temperature. HPLC analyses were performed using the Chromaster® system after injection of each sample (100 µL) using an autosampler. Relative peak areas were obtained by dividing the HTO compound peak areas by the internal standard peak area. The degradation rates of HTO compounds were determined by fitting a monoexponential decay curve. Quantum yields for photolysis were determined using the following equation (Eq. 3):

$$\Phi = (I\sigma t_{90\%})^{-1} \quad \text{(Eq. 3)}$$

I is the photon flux in einstein·s^{-1}·cm^{-2}, σ is the decadic extinction coefficient (10^3 times the molar extinction coefficient, ε) at cm^2·mol^{-1}, and $t_{90\%}$ is the irradiation time in seconds for 90% photoconversion to the product. The photon flux of the lamp I (2.9126×10^{-8} einstein·s^{-1}·cm^{-2}) was measured by potassium ferrioxalate actinometry (see the previous section for details).

Two-photon excitation

Sample solutions (15 µL) containing 50 µM Sul-HTO-Glu and 300 µM benzoic acid as internal standards were placed on a 35-mm glass bottomed dish (IWAKI), the surface of which contained fluorescent beads (FluoSpheres™ Polystyrene Microspheres 1.0 µm, orange fluorescence (ex/em = 540/560), Invitrogen, or Fluoresbrite® YG Microspheres, Calibration Grade 0.5 µm (ex/em = 441/486), Polysciences) as a reference point for setting the position of the two-photon focal volume within a droplet of sample solution. Samples were irradiated for 1 h with 940 nm (Sul-HTO-Glu) or 740 nm (MNI-Glu) light

using a femtosecond-pulsed and mode-locked Ti:sapphire laser (Mai Tai DeepSee, Spectra-Physics) focused on the center of the droplet using an upright microscope (A1R-MP$^+$; Nikon) equipped with a water immersion objective lens (Apo LWD W, 1.10 NA, 25×, Nikon). The average power used was 150 mW at 940 nm and 200 mW at 740 nm, which was measured after passing through the objective lens using a power meter (PM100D; Thorlabs) and microscope power sensor head (S170C; Thorlabs). After irradiation, samples were analyzed by HPLC (Prominence series; Shimazu) analysis using a reversed-phase column (Poroshell 120 EC-C18, 4.6 × 100 mm; Agilent) to quantify the percentage of remaining starting material.

NMR photolysis experiments

HTO-OAc was dissolved in a 7:3 (v/v) mixture of DMSO-*d6* and D_2O. The sample was transferred into an NMR tube and irradiated with an LED light source (CL-1501; Asahi, light intensity: 100 mW/cm^2, λ_{ex} = 505 ± 5 nm,) for the time indicated. After irradiation, the ^{1}H NMR spectrum was recorded at 25 ºC in a 500 MHz spectrometer.

Oxygen-18 labeling experiments

As a control, a 100 μM solution of HTO-OAc in water containing 10% DMSO was irradiated using a Xe lamp (light intensity = 10 mW/cm^2, λ_{ex} = 490 ± 5 nm) while stirring at room temperature. The reaction was monitored by HPLC (Column: Inertsil® ODS3, buffer A: 0.1% HCOOH in H_2O, buffer B: 0.1% HCOOH in CH_3CN, buffer A/B ratio (%): 80/20 (0 min), 50/50 (30 min).) The fraction corresponding to HTO-OH was collected and analyzed using a mass spectrometer. A 100 μM solution of HTO-OAc in ^{18}O-labeled water containing 10% DMSO was irradiated using a Xe lamp (light intensity = 10 mW/cm^2, λ_{ex} = 490 ± 5 nm) while stirring at room temperature. The reaction was analyzed by HPLC and MS along with an unlabeled control experiment.

Quantification of glutamate

Glutamate in the aqueous solution was quantified using a fluorescent derivatization method with 4-fluoro-7-nitro-2,1,3-benzoxadiazole.[60] The derivatized fluorescent product was quantified by HPLC with fluorescence detection (ex/em = 470/530 nm). Buffer A contained 0.1% HCOOH in H_2O and buffer B was composed of 0.1% HCOOH

in acetonitrile. Standard glutamate solutions (10, 20, 30, 40 μM) were used to prepare a calibration curve.

Plasmids

NMDA receptors plasmids were acquired from Addgene (pCI-EGFP-NR1 wt (#45446) and pCI-EGFP-NR2a wt (#45445)).[61] For oocyte experiments, untagged NR1 and NR2a were synthesized by removing GFP from GFP-NR1 and GFP-NR2 constructs.

Preparation of oocytes

Oocytes were prepared as described previously.[62] Briefly, *Xenopus* oocytes were collected from frogs anaesthetized in pure water containing 0.2% ethyl 3-aminobenzoate methanesulfonate salt (Sigma-Aldrich, USA). The oocytes were defolliculated using type I collagenase (1.0 mg/mL, Sigma-Aldrich, USA) before cRNA injection. The plasmids were linearized by Not I and the cRNA was synthesized using a mMESSAGE mMACHINE T7 transcription kit (Thermo Fisher Scientific). A volume of 50 nL containing an equal amount of NR1 and NR2a cRNA was injected into each oocyte. The injected oocytes were incubated for 2–3 days at 18 °C in ND96 solution (5 mM HEPES, 96 mM NaCl, 2 mM KCl, 1.8 mM $CaCl_2$, and 1 mM $MgCl_2$ (pH 7.5)).

Uncaging glutamate in oocytes

Currents were recorded using a two-electrode voltage clamp with an Oocyte Clamp OC-725C amplifier (Warner Instruments) and digitized by Digidata 1550B (Molecular Devices). Electrodes were filled with a 3 M KCl solution. The software for the acquisition and analysis of data was Axon™ pCLAMP™ (Molecular Devices). The bath solution contained 115 mM NaCl, 5 mM KCl, 10 mM HEPES, 1.8 mM $BaCl_2$, and 0.01 mM EDTA (pH 7.3). The oocytes were irradiated with an LED light source (CL-1501; Asahi, λ_{ex} = 505 nm, laser intensity = 30 mW/cm^2, irradiation period = 10 s).

Cell culture and expression of NMDARs

HEK293T cells were cultured in Dulbecco's modified Eagle's medium (DMEM) containing 10% fetal bovine serum (FBS) and two antibiotics (100 units/mL penicillin and 0.1 mg/mL streptomycin). HEK293 cells expressing GFP-NR1 and GFP-NR2A subunits (1:1 ratio) were placed in a 35 mm glass-bottomed dish. Transient transfection was performed using Lipofectamine 3000 (Invitrogen) according to the manufacturer's instructions. At 4 h after transfection, the NMDAR antagonists DL-2-amino-5-phosphonovalerate (200 μM) and 7-chlorokynurenic acid (200 μM) were added to the

culture medium to reduce the cytotoxic effects of NMDAR expression. Cells were evaluated at 24–48 h post-transfection.

Calcium imaging

Calcium imaging was performed using an Olympus Fv10i confocal microscope equipped with a 60X lens. Non-transfected and transfected HEK293 cells were incubated in Mg^{2+}- and Ca^{2+}-free HEPES-buffered Hanks balanced salt solution (HHBSS) with 0.01% Pluronic F-127 (AnaSpec) containing 5 μg/mL Calbryte 590 AM Ca^{2+}-sensitive dye (AAT Bioquest) for 30 min at 37°C. The cells were rinsed twice with Mg^{2+}- and Ca^{2+}-free HHBSS before adding 10 mM Ca^{2+} in Mg^{2+}-free HHBSS containing 25 μM Sul-HTO-Glu and 50 μM glycine. Before the uncaging experiments, GFP fluorescence was used to localize GFP-NMDARs using the following excitation and emission wavelengths: GFP: 473 nm and 490–540 nm, respectively. Samples were uncaged with an LED light source (CL-1501; Asahi, λ_{ex} = 505 nm, laser intensity = 90 mW/cm^2, irradiation period = 10 s). Images were acquired every 5 s using the following excitation and emission wavelengths: Calbryte 590 AM: 559 nm and 570–620 nm, respectively. ImageJ was used for image analysis and presentation. The mean value of fluorescence in a cell was obtained by enclosing the cell in an ROI. $\Delta F/F_0$ was reported as the change in fluorescence intensity ($\Delta F = F_t - F_0$) relative to the fluorescence intensity which was calculated by averaging the frames (F_0) before irradiation.

Statistical analysis

Data were analyzed using a two-tailed Student's *t*-test (GraphPad Prism; GraphPad Software).

Cytotoxicity assay

HEK293T cells were re-plated into 96-well plates (1×10^4 cells/well) in DMEM containing 10% FBS and incubated overnight. The cells were then treated with the indicated concentrations of Sul-HTO-Glu. After 1 h, the cells were irradiated with an LED light source (CL-1501; Asahi, λ_{ex} = 505 nm, laser intensity = 30 or 90 mW/cm^2, irradiation period = 10 s). After 24 h, PrestoBlue™ cell viability reagent was added, and the cells were further incubated according to the manufacturer's guidelines. Cell viability was calculated by measuring the absorbance at 570 nm (experimental wavelength) and 600 nm (reference wavelength) using an M1000 microplate reader (Tecan).

Two-photon Sul-HTO-Glu uncaging

Hippocampal slices and transfection of Clover were prepared as described.[63] To activate Sul-HTO-Glu in single spines with two-photon excitation, a second Ti: sapphire laser

tuned at a wavelength of 980 nm was used with 30 trains (0.5 Hz or 1 Hz, 6 ms duration/pulse, 4 mW) in a spine of interest. Since the focal plane of imaging (1000 nm) and uncaging (980 nm) lasers were different (0.5–1.0 μm) due to chromatic aberration in the microscope, it was compensated by moving sample stage in z-axis (0.5–1.0 μm) with piezo stages (PKVL64F-100U, NCS6101C, Kohzu; Kawasaki, Japan) during the light activation of Sul-HTO-Glu. Experiments were performed in artificial cerebrospinal fluid containing no $MgCl_2$, 4 mM $CaCl_2$, 1 μM TTX, and 50 μM Sul-HTO-Glu aerated with 95% O_2/5% CO_2. Experiments were performed at 24–26 °C.

Synthesis of compound

Compound 1, 2, 3

Compound 1,2,3 were prepared according to literature procedures.[64]

4-chloro-2-methylquinolin-7-ol (compound 4)

Under a nitrogen atmosphere, BBr_3 (1 M solution in DCM, 4.66 mL, 4.66 mmol) was added to a solution of compound 3 (363 mg, 1.75 mmol) in DCM 15 mL at 0 °C. After complete addition, the ice bath was removed and stirring was continued for 3 h at room temperature. The reaction mixture was then added dropwise to a mixture of water and ice (30 mL) under stirring. After complete addition, the mixture was stirred for 30 min at room temperature and then filtered to give, after drying 4-chloro-2-methylquinolin-7-ol (compound 4) as a yellow solid (255 mg, 0.753 mmol, 75%): ^{1}H NMR (500 MHz, MeOD) δ 8.37 (d, J = 9.0 Hz, 1H), 7.85 (s, 1H), 7.52 (dd, J = 9.0 Hz, J = 2.0 Hz, 1H), 7.37 (d, J = 2.0 Hz, 1H), 2.89 (s, 3H); ^{13}C NMR (125 MHz, MeOD) δ 164.8, 156.7, 151.9, 141.3, 127.3, 122.6, 120.0, 119.9, 101.5, 19.9; HRMS (FAB+) Calcd for $[M+H]^+$, 194.0372, found for 194.0377.

4-chloro-7-(methoxymethoxy)-2-methylquinoline (compound 5)

Under a nitrogen atmosphere, *N*,*N*-diisopropylethylamine (0.225 mL, 1.30 mmol) was added to the solution of compound 4 (100 mg, 0.518 mmol) in dry DMF (10 mL). Chloromethyl methyl ether (0.098 mL, 1.30 mmol) was added to the reaction mixture dropwise. After stirring for 2 h, the solvent was concentrated under reduced pressure. The residue was purified by flash chromatography (4:6 EtOAc/hexane) to afford compound 5 as a colorless solid (71.7 mg, 0.302 mmol): ^{1}H NMR (500 MHz, $CDCl_3$) δ 8.09 (d, J = 9.0 Hz, 1H), 7.60 (d, J = 2.0 Hz, 1H), 7.29 (dd, J = 9.0 Hz, J = 2.0 Hz, 1H), 7.27 (s, 1H), 5.32 (s, 2H), 3.51 (s, 3H), 2.69 (s, 3H); ^{13}C NMR (125 MHz, $CDCl_3$) δ 159.5, 158.8,

150.2, 142.3, 125.2, 120.3, 120.1, 119.6, 111.0, 94.4, 56.3, 25.1; HRMS (FAB+) Calcd for $[M+H]^+$, 238.0635, found for 238.0638.

4-chloro-7-(methoxymethoxy)quinoline-2-carbaldehyde (compound 6)

Under a nitrogen atmosphere, selenium dioxide (135 mg, 1.22 mmol) was added to a solution of compound 5 (262 mg, 1.11 mmol) in dioxane (30 mL). The reaction mixture was stirred for 4 h at 85 °C, then cooled, diluted with methanol, and vacuum filtered. The filtrate was collected and concentrated, leaving a yellow solid, which was purified by column chromatography (2:8 EtOAc/hexane) to provide compound 6 (231 mg, 0.920 mmol) as a yellow solid: ^{1}H NMR (500 MHz, $CDCl_3$) δ 10.14 (s, 1H) 8.22 (d, J = 9.0 Hz, 1H), 7.97 (s, 1H), 7.82 (d, J = 2.0 Hz, 1H), 7.50 (dd, J = 9.0 Hz, J = 2.0 Hz, 1H), 5.38 (s, 2H), 3.54 (s, 3H); ^{13}C NMR (125 MHz, $CDCl_3$) δ 192.7, 159.4, 152.8, 150.4, 144.0, 125.6, 123.7, 123.5, 116.0, 112.1, 94.5, 56.5; HRMS (FAB+) Calcd for $[M+H]^+$, 252.0427, found for 252.0426.

(4-chloro-7-(methoxymethoxy)quinolin-2-yl)methanol (compound 7)

$NaBH_4$ was added to a solution of compound 6 (70.0 mg, 0.279 mmol) in methanol (15 mL). The reaction mixture was stirred for 15 min, diluted with EtOAc, washed with water followed by brine. The organic layer was dried over Na_2SO_4 and the solvent was evaporated to afford compound 7 (67.2 mg, 0.266 mmol) as a yellow solid: ^{1}H NMR (500 MHz, $CDCl_3$) δ 8.13 (d, J = 9.0 Hz, 1H), 7.65 (d, J = 2.0 Hz, 1H), 7.35 (dd, J = 9.0 Hz, J = 2.0 Hz, 1H), 7.28 (s, 1H), 5.38 (s, 2H), 4.86 (s, 2H), 4.15(br, 1H), 3.54 (s, 3H); ^{13}C NMR (125 MHz, $CDCl_3$) δ 159.6, 159.0, 149.1,143.0, 125.5, 121.3, 120.2, 116.6, 111.0, 94.4, 63.9, 56.4; HRMS (FAB+) Calcd for $[M+H]^+$, 254.0584, found for 254.0578.

(4-chloro-7-(methoxymethoxy)quinolin-2-yl)methyl acetate (compound 8)

Compound 7 (100 mg, 0.395 mmol) was dissolved in pyridine (2.5 mL). To the solution, acetic anhydride (37 μL, 0.395 mmol) was added. After being stirred at room temperature for 4 h, the reaction mixture was concentrated in vacuo, followed by flash chromatography to afford compound 8 as a colorless solid (83.0 mg, 0.281 mmol): ^{1}H NMR (500 MHz, $CDCl_3$) δ 8.12 (d, J = 9.0 Hz, 1H), 7.65 (d, J = 2.0 Hz, 1H), 7.43 (s, 1H), 7.35 (dd, J = 9.0 Hz, J = 2.0 Hz, 1H), 5.33 (s, 2H), 5.32 (s, 2H), 3.52 (s, 3H), 2.21 (s, 3H); ^{13}C NMR (125 MHz, $CDCl_3$) δ 170.6, 159.0, 156.7, 150.1, 143.2, 125.3, 121.3,

120.8, 117.7, 111.2, 94.4, 66.9, 56.4, 20.9; HRMS (FAB+) Calcd for [M+H]+, 296.0690, found for 296.0691.

4-chloro-2-(hydroxymethyl)-7-(methoxymethoxy)-1-methylquinolin-1-ium (Compound 9)

To a solution of compound 8 (50 mg, 0.169 mmol) in DCM (1.0 mL) was added dropwise methyl trifluoromethanesulfonate (37 μL, 0.339 mmol). After being stirred at room temperature for 4 h, the reaction mixture was concentrated in vacuo, followed by flash chromatography (10:1 DCM/MeOH) to provide the compound 9 (41.3 mg, 0.133 mmol) as a blue powder: ^{1}H NMR (500 MHz, $CDCl_3$) δ 8.42 (d, J = 9.5 Hz, 1H), 7.91 (s, 1H), 7.80 (d, J = 2.0 Hz, 1H), 7.66 (dd, J = 9.5 Hz, J = 2.0 Hz, 1H), 5.72 (s, 2H), 5.51 (s, 2H), 4.47 (s, 3H), 3.55 (s, 3H), 2.23 (s, 3H); ^{13}C NMR (125 MHz, $CDCl_3$) δ 169.9, 164.2, 155.7, 152.9, 143.1, 128.5, 123.7, 122.9, 120.6, 102.2, 95.5, 62.4, 57.2, 40.1, 20.5; HRMS (FAB+) Calcd for [M+H]+, 310.0841, found for 310.0847

Compound 10

Compound 10 was prepared according to a literature procedure.[65]

(Z)-2-(acetoxymethyl)-7-hydroxy-1-methyl-4-((3-methylbenzo[d]thiazol-2(3H)-ylidene)methyl)quinolin-1-ium (compound 11)

To a solution of the above compound 9 in ethanol (2.0 mL) was added compound 10 (42.6 mg, 0.258 mmol) and *N*,*N*-diisopropylethylamine (45 μL, 0.258 mmol). After being stirred at room temperature for 3 h in the dark, the solvent was removed under reduced pressure. The residue was used in the next step without further purification. To a solution of crude in DCM (4.00 mL) was added TFA (1.00 mL). After stirring for 2 h, a solvent was removed under reduced pressure. The residue was purified by reversed-phase HPLC under the following conditions: A/B = 80/20 (0 min), 50/50 (30 min), (solvent A: 0.1% HCOOH in H_2O; solvent B: 0.1% HCOOH in CH_3CN). After lyophilization, an orange powder of compound 11 (5.30 mg, 0.0135 mmol) was obtained: ^{1}H NMR (500 MHz, DMSO-d_6) δ 8.65 (d, J = 9.0 Hz, 1H), 8.04 (d, J = 8.0 Hz, 1H), 7.74 (d, J = 8.0 Hz, 1H), 7.59 (t, J = 8.0 Hz, 1H), 7.39 (t, J = 8.0 Hz, 1H), 7.36 (s, 1H), 7.32 (d, J = 8.0 Hz, 1H,) 7.26 (dd, J = 9.0 Hz, J = 2.0 Hz, 1H), 6.82 (s, 1H), 5.54 (s, 2H), 3.96 (s, 3H), 3.91 (s, 3H), 2.29 (s, 3H) ; ^{13}C NMR (125 MHz, DMSO-d_6) δ 170.3, 162.9, 159.7, 149.7, 148.5, 142.1,

141.0, 128.6, 128.1, 124.7, 124.1, 123.3, 118.0, 117.3, 113.2, 107.4, 101.9, 88.1, 63.1, 37.0, 34.1, 21.2; HRMS (FAB+) Calcd for $[M]^+$ 393.1267, found for 393.1271

(4-chloro-7-(methoxymethoxy)quinolin-2-yl)methylbenzo[d][1,3]dioxole-5-carboxylate (compound 12)

Under a nitrogen atmosphere, compound 7 (100 mg, 0.242 mmol) was dissolved in DCM (10 mL). *N*,*N*-diisopropylethylamine (45 μL, 0.36 mmol) and *N*,*N*-dimethyl-4-aminopyridine (10 mg, 0.08 mmol) were added, followed by piperonylic chloride (50 mg, 0.27 mmol). The reaction was stirred for 2 h. The mixture was washed with 0.1 M citric acid, water, and brine. The organic layer was dried over anhydrous Na_2SO_4. The solvent was evaporated, and the residue was purified by flash chromatography (3:7 EtOAc/hexane) to afford compound 12 as a colorless solid (90 mg, 0.16 mmol): ^{1}H NMR (500 MHz, $CDCl_3$) δ 8.14 (d, *J* = 9.0 Hz, 1H), 7.76 (dd, *J* = 8.0 Hz, *J* = 2.0 Hz, 1H), 7.65 (d, *J* = 2.0 Hz, 1H), 7.56 (d, *J* = 2.0 Hz, 1H), 7.50 (s, 1H), 7.36 (dd *J* = 9.0 Hz, *J* = 2.0 Hz, 1H), 6.88 (d, *J* = 8.0 Hz, 1H), 6.06 (s, 2H), 5.54 (s, 2H), 5.34 (s, 2H), 3.52 (s, 3H); ^{13}C NMR (125 MHz, $CDCl_3$) δ 165.5, 159.0, 157.0, 152.0, 151.1, 147.9, 143.3, 125.8, 125.4, 123.6, 121.4, 120.8, 117.6, 111.2, 109.7, 108.1, 102.0, 94.4, 67.3, 56.4; HRMS (FAB+) Calcd for $[M+H]^+$, 402.0744, found for 402.0749

2-(((benzo[d][1,3]dioxole-5-carbonyl)oxy)methyl)-4-chloro-7-(methoxymethoxy)-1-methylquinolin-1-ium (compound 13)

To a solution of compound 12 (33 mg, 0.823 mmol) in DCM (1.0 mL) was added dropwise methyl trifluoromethanesulfonate (18 μL, 0.165 mmol). After being stirred at room temperature for 4 h, the reaction mixture was concentrated in vacuo, followed by flash chromatography (10:1 DCM/MeOH) to provide the compound 13 (16.0 mg, 0.321 mmol) as a blue powder: ^{1}H NMR (500 MHz, $CDCl_3$) δ 8.43 (d, *J* = 9.0 Hz, 1H), 7.92 (s, 1H), 7.81 (d, *J* = 2.0 Hz, 1H), 7.73 (dd, *J* = 8.0 Hz, *J* = 2.0 Hz, 1H), 7.66 (dd, *J* = 9.0 Hz, *J* = 2.0 Hz, 1H), 7.48 (d, *J* = 2.0 Hz, 1H), 6.90 (d, *J* = 8.0 Hz, 1H), 6.09 (s, 2H), 5.96 (s, 2H), 5.50 (s, 2H), 4.57 (s, 3H), 3.56 (s, 3H); ^{13}C NMR (125 MHz, $CDCl_3$) δ 165.0, 164.2, 156.0, 153.0, 152.9, 148.2, 143.1, 128.6, 126.4, 123.6, 122.9, 121.6, 120.7, 109.6, 108.5, 102.2, 102.1, 95.4, 62.8, 57.2, 40.2; HRMS (FAB+) Calcd for $[M]^+$, 416.0895, found for 416.0900.

(Z)-2-(((benzo[d][1,3]dioxole-5-carbonyl)oxy)methyl)-7-hydroxy-1-methyl-4-((3-methylbenzo[d]thiazol-2(3H)-ylidene)methyl)quinolin-1-ium (compound 14)

Compound 10 (13.2 mg, 0.0803 mmol) was added to the solution of compound 13 (16.7 mg, 0.0401 mmol) in ethanol (2 mL). *N*,*N*-diisopropylethylamine (0.014 mL, 0.0803

mmol) was added to the reaction mixture dropwise. After stirring at room temperature for 3 h, the solvent was concentrated under reduced pressure. The residue was purified by flash chromatography (20:1 DCM/MeOH) to provide the orange powder, which was used immediately in next step. To the solution of crude in DCM (5 mL) was added TFA (2 mL). After stirring for 2 h, a solvent was removed under reduced pressure. The residue was purified by reversed-phase HPLC under the following conditions: A/B = 35/65 (0 min), 25/75 (30 min), (solvent A: 0.1% HCOOH in H_2O; solvent B: 0.1% HCOOH in CH_3CN). After lyophilization, an orange powder of compound 14 (3.35 mg, 0.00285 mmol) was obtained. ^{1}H NMR (500 MHz, CD_3CN) δ 8.28 (d, *J* = 9.5 Hz, 1H), 7.75 (d, *J* =8.0 Hz, 1H), 7.56 (s, 1H), 7.45 (d, *J* =8.0 Hz, 1H), 7.44 (t, *J* = 8.0 Hz, 1H), 7.36 (d, *J* = 9.5 Hz, 1H), 7.34 (s, 1H), 7.29 (s, 1H), 7.24 (t, *J* = 8.0 Hz, 1H), 7.18 (d, *J* = 8.5 Hz, 1H), 6.92 (d, *J* = 8.5 Hz, 1H), 6.52 (s, 1H), 6.02 (s, 2H), 5.54 (s, 2H), 3.83 (s, 3H), 3.71 (s, 3H); ^{13}C NMR (125 MHz, $CDCl_3/CD_3OD$); δ 168.0, 165.5, 159.1, 153.4, 149.3, 148.7, 148.1, 143.2, 141.0, 128.6, 127.1, 126.8, 124.8, 124.2, 122.9, 122.4, 121.0, 117.2, 112.2, 110.0, 108.8, 107.6, 102.9, 101.7, 87.8, 63.1, 36.4, 33.4; HRMS (FAB+) Calcd for $[M]^+$, 499.1322, found for 499.1327.

3-(2-methylbenzo[d]thiazol-3-ium-3-yl)propane-1-sulfonate (compound 15)

To a solution of 2-methylbenzothiazole (1000 mg, 6.06 mmol) in toluene (5.0 mL) was added 1,3-propanesultone (1110 mg, 9.09 mmol). The solution was refluxed for 24 h. The precipitate produced was filtered under suction, washed with toluene and dried *in vacuo* to afford compound 15 (1367 mg, 5.04 mmol, 75%) as a white solid: ^{1}H NMR (500 MHz, D_2O) δ 8.10 (d, *J* = 8.5 Hz, 1H), 8.09 (d, *J* = 8.5 Hz, 1H), 7.81 (t, *J* = 8.0 Hz, 1H), 7.70 (t, *J* = 8.0 Hz, 1H), 4.81 (m, 2H), 3.11 (s, 3H), 3.05 (t, *J* = 7.0 Hz, 2H), 2.34-2.28 (m, 2H); ^{13}C NMR (125 MHz, D_2O) δ 176.3, 141.0, 129.8, 129.0, 128.5, 123.8, 116.2, 47.7, 47.4, 23.1, 16.2; HRMS (FAB+) Calcd for $[M]^+$, 272.0415, found for 272.0413.

di-tert-butyl(((4-chloro-7-(methoxymethoxy)quinolin-2-yl)methoxy)carbonyl)glutamate (compound 16)

Under a nitrogen atmosphere, compound 7 (100 mg, 0.395 mmol) was dissolved in dry DCM (1.5 mL). 1,1'-Carbonyldiimidazole (769 mg, 0.474 mmol) was added, and the mixture was stirred at 0 ºC for 1 h. To the stirred solution were added H-Glu-(O^{t}Bu)-O^{t}Bu·HCl (233.8 mg, 0.790 mmol) and Et_3N (55.0 μL, 0.395 mmol) at 0 ºC. After stirring at room temperature for 23 h, the solvent was concentrated under reduced pressure. After being diluted with Et_2O, the mixture was washed with water, and brine. The organic layer was dried over anhydrous Na_2SO_4. The solvent was evaporated, and the residue was

purified by flash chromatography (3:7 EtOAc/hexane) to afford compound 16 (171 mg, 0.318 mmol, 80%) as a colorless solid: ^{1}H NMR (500 MHz, $CDCl_3$) δ 8.12 (d, *J* = 9.0 Hz, 1H), 7.64 (d, *J* = 2.5 Hz, 1H), 7.46 (s, 1H), 7.34 (dd, *J* = 9.0 Hz, *J* = 2.5 Hz, 1H), 5.54 (d, *J* = 8.0 Hz, 1H) 5.33 (s, 2H), 5.32 (s, 2H), 4.32-4.28 (m, 1H), 3.51 (s, 3H), 2.41-2.27 (m, 2H), 2.20-2.13 (m, 1H), 1.98-1.91 (m, 1H), 1.48 (s, 9H), 1.44 (s, 9H); ^{13}C NMR (125 MHz, $CDCl_3$); δ 171.1, 170.0, 158.9, 157.4, 155.6, 150.0, 143.2, 125.3, 121.3, 120.7, 117.5, 111.2, 94.4, 82.5, 80.8, 67.3, 56.3, 54.1, 28.1, 28.0, 27.9; HRMS (FAB+) Calcd for $[M]^+$, 539.2160, found for 539.2152.

(Z)-3-(2-((2-((((1,3-dicarboxypropyl)carbamoyl)oxy)methyl)-7-hydroxy-1-methyl-1l4-quinolin-4-yl)methylene)benzo[d]thiazol-3(2H)-yl)propane-1-sulfonate (compound 17)

To a solution of compound 16 (60 mg, 0.111 mmol) in DCM (1.0 mL) was added dropwise methyl trifluoromethanesulfonate (24 μL, 0.223 mmol). After being stirred at room temperature for 4 h, the reaction mixture was concentrated in vacuo, which was used in the next step without further purification. To a solution of the above quinolinium in ethanol (2.5 mL) was added compound 15 (44 mg, 0.163 mmol) and *N*,*N*-diisopropylethylamine (28 μL, 0.163 mmol). After being stirred at room temperature for 3 h in the dark, the solvent was removed under reduced pressure. The residue was used in the next step without further purification. To a solution of crude in DCM (4.00 mL) was added TFA (1.00 mL). After stirring for 2 h, a solvent was removed under reduced pressure. The residue was purified by reversed-phase HPLC under the following conditions: A/B = 75/25 (0 min), 35/65 (30 min), (solvent A: 0.1% HCOOH in H_2O; solvent B: 0.1% HCOOH in CH_3CN). After lyophilization, an orange powder of compound 17 (3.24 mg, 0.00513 mmol) was obtained: ^{1}H NMR (500 MHz, DMSO-d_6) δ 11.1 (s, 1H), 8.94 (d, *J* = 9.5 Hz, 1H), 8.21 (d, *J* = 8.0 Hz, 1H), 7.94 (d, *J* = 8.0 Hz, 1H), 7.78 (d, *J* = 8.0 Hz 1H), 7.55 (t, *J* = 8.0 Hz 1H), 7.38 (s, 1H), 7.36 (t, *J* = 8.0 Hz, 1H), 7.27 (d, *J* = 2.0 Hz, 1H), 7.18 (dd, *J* = 9.5 Hz, *J* = 2.0 Hz, 1H), 7.05 (s, 1H), 5.54 (s, 2H), 4.73 (t, *J* = 6.0 Hz, 2H), 4.12-4.08 (m, 1H), 3.90 (s, 3H), 2.69 (t, *J* = 6.0 Hz, 2H), 2.40-2.28 (m, 2H) 2.12-2.06 (m, 2H), 2.05-2.00 (m, 1H), 1.89-1.82 (m, 1H); ^{13}C NMR (125 MHz, DMSO-d_6) δ 165.1, 164.8, 153.7, 146.5, 142.0, 139.8, 133.0, 131.4, 120.3, 119.4, 115.6, 114.2, 108.8, 108.5, 104.0, 96.7, 92.5, 78.8, 53.4, 44.7, 37.2, 36.1, 27.5, 21.5, 17.6; HRMS (FAB+) Calcd for $[M]^+$, 632.1373, found for 632.1384.

Reference

[36] P. Klán, T. Šolomek, C. G. Bochet, A. Blanc, R. Givens, M. Rubina, V. Popik, A. Kostikov, J. Wirz, *Chem. Rev.* **2013**, *113*, 119–191.

[37] P. Paoletti, G. C. R. Ellis-Davies, A. Mourot, *Nat. Rev. Neurosci.* **2019**, *20*, 514–532.

[38] J. M. Silva, E. Silva, R. L. Reis, *J. Control. Release* **2019**, *298*, 154–176.

[39] E. Fino, R. Araya, D. S. Peterka, M. Salierno, R. Etchenique, R. Yuste, *Front. Neural Circuits* **2009**, *3*, 1–9.

[40] N. G. Patil, N. B. Basutkar, A. V. Ambade, *Chem. Commun.* **2015**, *51*, 17708–17711.

[41] N. Umeda, H. Takahashi, M. Kamiya, T. Ueno, T. Komatsu, T. Terai, K. Hanaoka, T. Nagano, Y. Urano, *ACS Chem. Biol.* **2014**, *9*, 2242–2246.

[42] P. P. Goswami, A. Syed, C. L. Beck, T. R. Albright, K. M. Mahoney, R. Unash, E. A. Smith, A. H. Winter, *J. Am. Chem. Soc.* **2015**, *137*, 3783–3786.

[43] J. A. Peterson, C. Wijesooriya, E. J. Gehrmann, K. M. Mahoney, P. P. Goswami, T. R. Albright, A. Syed, A. S. Dutton, E. A. Smith, A. H. Winter, *J. Am. Chem. Soc.* **2018**, *140*, 7343–7346.

[44] R. R. Nani, A. P. Gorka, T. Nagaya, H. Kobayashi, M. J. Schnermann, *Angew. Chem. Int. Ed.* **2015**, *54*, 13635–13638.

[45] R. R. Nani, A. P. Gorka, T. Nagaya, T. Yamamoto, J. Ivanic, H. Kobayashi, M. J. Schnermann, *ACS Cent. Sci.* **2017**, *3*, 329–337.

[46] R. Weinstain, T. Slanina, D. Kand, P. Klán, *Chem. Rev.* **2020**, *120*, 13135–13272.

[47] D. Kand, P. Liu, M. X. Navarro, L. J. Fischer, L. Rousso-Noori, D. Friedmann-Morvinski, A. H. Winter, E. W. Miller, R. Weinstain, *J. Am. Chem. Soc.* **2020**, *142*, 4970–4974.

[48] M. Klausen, M. Blanchard-Desce, *J. Photochem. Photobiol.* **2021**, *48*, 100423.

[49] G. C. R. Ellis-Davies, *Front. Synaptic. Neurosci.* **2019**, *10*, 1–13.

[50] J. P. Olson, H. B. Kwon, K. T. Takasaki, C. Q. Chiu, M. J. Higley, B. L. Sabatini, G. C. R. Ellis-Davies, *J. Am. Chem. Soc.* **2013**, *135*, 5954–5957.

[51] S. Ikeda, T. Kubota, M. Yuki, A. Okamoto, *Angew. Chem. Int. Ed.* **2009**, *48*, 6480–6484.

[52] O. D. Fedoryak, T. M. Dore, *Org. Lett.* **2002**, *4*, 3419–3422.

[53] M. Jarrett Davis, C. H. Kragor, K. G. Reddie, H. C. Wilson, Y. Zhu, T. M. Dore, *J. Org. Chem.* **2009**, *74*, 1721–1729.

[54] T. Narumi, K. Miyata, A. Nii, K. Sato, N. Mase, T. Furuta, *Org. Lett.* **2018**, *20*, 4178–4182.

[55] A. L. K. Hennig, D. Deodato, N. Asad, C. Herbivo, T. M. Dore, *J. Org. Chem.* **2020**, *85*, 726–744.

[56] J. Ma, A. C. Rea, H. An, C. Ma, X. Guan, M. De Li, T. Su, C. S. Yeung, K. T. Harris, Y. Zhu, J. L. Nganga, O. D. Fedoryak, T. M. Dore, D. L. Phillips, *Chem. Eur. J.* **2012**, *18*, 6854–6865.

[57] G. C. R. Ellis-Davies, *Acc. Chem. Res.* **2020**, *53*, 1593–1604.

[58] S. F. Traynelis, L. P. Wollmuth, C. J. McBain, F. S. Menniti, K. M. Vance, K. K. Ogden, K. B. Hansen, H. Yuan, S. J. Myers, R. Dingledine, *Pharmacol. Rev.* **2010**, *62*, 405–496.

[59] H. J. Kuhn, S. E. Braslavsky, R. Schmidt, *Pure Appl. Chem.* **2004**, *76*, 2105–2146.

[60] K. Imai, Y. Watanabe, *Analytica. Chimica. Acto.* **1981**, *130*, 377–383.

[61] A. Barria, *Neurons* **2002**, *35*, 345–353.

[62] S. Sakata, Y. Jinno, A. Kawanabe, Y. Okamura, *Proc. Natl. Acad. Sci. USA* **2016**, *113*, E7866.

[63] A. C. E. Shibata, H. H. Ueda, K. Eto, M. Onda, A. Sato, T. Ohba, J. Nabekura, H. Murakoshi, *Nat. Commun.* **2021**, *12*, DOI 10.1038/s41467-021-21025-6.

[64] Y. Abe, H. Kayakiri, S. Satoh, T. Inoue, Y. Sawada, N. Inamura, M. Asano, I. Aramori, C. Hatori, H. Sawai, T. Oku, H. Tanaka, *J. Med. Chem.* **1998**, *41*, 4062–4079.

[65] P. Gaur, A. Kumar, G. Dey, R. Kumar, S. Bhattacharyya, S. Ghosh, *ACS Appl. Mater. Interfaces* **2016**, *8*, 10690–10699.

Chapter 3

Rational Design of Hydroxylated Thiazole Orange Photocages for Green Light-Triggered DNA Recombination

Introduction

Precise control of DNA recombination can be exploited to induce the cell- or tissue-specific or time-dependent regulation of protein expression, leading to a deeper understanding of gene function. The Cre-ERT2/loxP system[66], a modified Cre/LoxP system, is one of the major methods for DNA recombination triggered by a small molecule inducer for estrogen receptor (ER). Cre-ERT2 remains in the cytoplasm until bound by the estrogen and its analogues (4-hydroxytamoxifen and cyclofen-OH inducer (Ind)). After ligand binding, the Cre enzyme translocates to the nucleus and recognizes the 34 bp DNA sequences called loxP sites, driving DNA recombination for the permanent activation or deletion of a gene flanked by two loxP sites. To realize spatiotemporal control of DNA recombination, photocaged small molecules (caged compounds) represent a versatile strategy.[67] In caged compounds, photo-responsive protecting groups (PPGs) are essential moieties that mediate the release of target compounds after light irradiation.[36] Thus far, *o*-nitrobenzene (ONB)[16] coumarin[68,69] and cyanine[17,18] caged ER antagonists are the most commonly used PPGs. ONB and coumarin photocages have been used to control light-inducible reporter gene recombination in cells and optogenetic mouse models.[70] However, both compounds require high-energy ultraviolet (UV) or blue light, which directly damages DNA and results in cell death. Although cyanine-caged inducers can be activated by longer visible/near-infrared light, thus reducing phototoxicity and enabling deep tissue penetration in living tissues or animals,[17,44] photodegradation requires prolonged illumination (30–60 min) because of its low uncaging efficiency.

In chapter 2, the author developed green (one-photon) and near-infrared (two-photon) light-sensitive PPGs based on a hydroxylated thiazole orange (HTO) chromophore.[71] The photolytic efficiencies of HTO-caged compounds in aqueous solution after green-light illumination are much higher than the efficiencies of caged compounds illuminated at wavelengths > 500 nm (e.g., BODIPY[42,72] or cyanine-based[17,73] photocages). Additionally, HTO-caged compounds display minimal fluorescence, such that there is no interference with the signal of a fluorescence indicator. HTO-caged glutamate activates *N*-methyl-D-aspartic acid receptors in *Xenopus* oocytes and mammalian HEK293T cells via green-light illumination. Considering the visible light sensitivity characteristics and

fast-uncaging kinetics, HTO-caged compounds may be useful in the precise spatiotemporal control of DNA recombination in living cells. Further improvement of the photolytic efficiencies of HTO-caged compounds will allow a wider range of applications. Here, the author describes the development of an HTO-based caged ER ligand for green-light-inducible DNA recombination in a Cre-ERT2/loxP system.

The photolytic efficiency of PPG was improved by synthesizing a series of HTO-based PPGs in which an electron-donating group (EDG) or electron-withdrawing group (EWG) was linked to the benzothiazole of TO, based on investigations of the effects of substituents on the PPG's photochemical properties. The introduction of EDG led to greater uncaging efficiency as supported by theoretical calculations. Experiments using the caged ER ligand with the most efficient HTO-analogue (DiMeO-HTO) demonstrated that temporal control of genetic recombination could be achieved with the Cre-ERT2/loxP system under green-light irradiation.

Results and Discussion

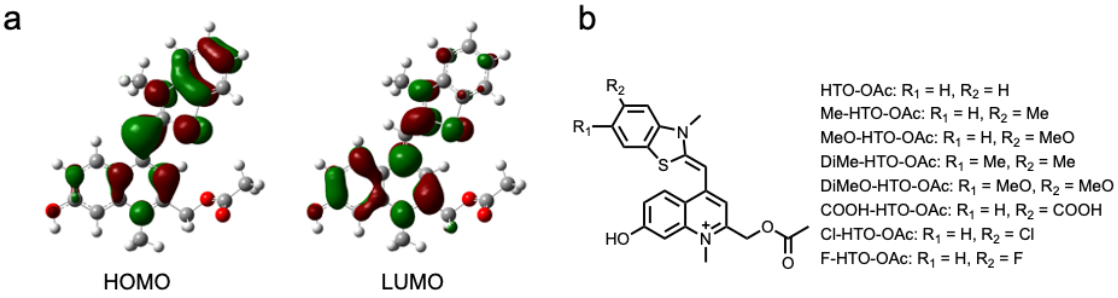

Figure 26. (a) Graphical representations of the frontier orbitals of HTO-OAc, calculated at the PCM: B3LYP/6-31G (d, p) level. Solvent: H_2O. (b) Structures of HTO derivatives bearing EWG or EDG at benzothiazole moiety.

Scheme 5. Synthesis of HTO derivatives

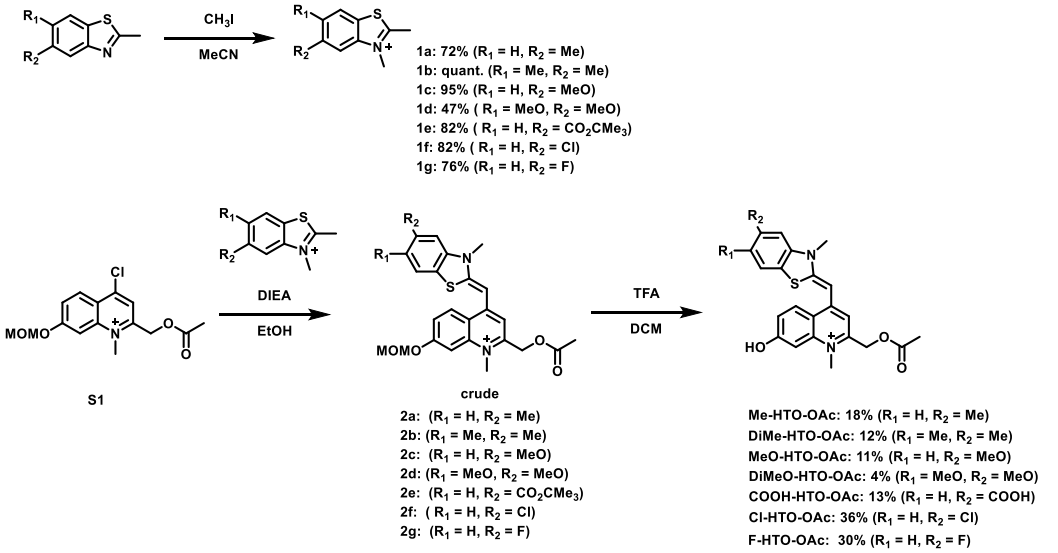

To improve photolytic efficiency, the author focused on the modification of the chromophore to change its intramolecular charge transfer (ICT) upon photo-induced excitation. Multiple studies have reported precise adjustment of the molecular design of existing caged compounds to increase their photolytic efficiencies. For example, extension of the π-conjugated system at the 3-position of coumarin photocages, such as DEAC450[50,74] and π-extended dipolar coumarins[75], led to accelerated ICT and an increased quantum yield. Similarly, the introduction of an electron-rich aromatic group at the 4-position of a quinoline-based PPG enhanced both one-photon and two-photon photolytic efficiencies.[55] Therefore, the author hypothesized that modification of the HTO scaffold would alter ICT, leading to enhanced photolytic efficiency. In the molecular

Table 2. Photochemical properties of HTO derivatives. [a]Solutions in MeOH containing 0.1%DMSO, [b]Solutions in PBS with 20% MeCN containing 0.1%DMSO.

Compound	λ_{abs}[a] (nm)	ε (M^{-1} cm^{-1})[b]	Φ_{chem}[b]	photolytic efficiency[b] ($\varepsilon \cdot \Phi_{chem}$)
HTO-OAc	494	46700	3.68×10^{-3}	**141**
Me-HTO-OAc	500	45700	3.17×10^{-3}	**145**
DiMe-HTO-OAc	505	31700	6.15×10^{-3}	**195**
MeO-HTO-OAc	503	46300	5.37×10^{-3}	**249**
DiMeO-HTO-OAc	520	50600	6.39×10^{-3}	**324**
COOH-HTO-OAc	499	68900	2.37×10^{-3}	**163**
Cl-HTO-OAc	493	64900	1.53×10^{-3}	**100**
F-HTO-OAc	493	47300	1.09×10^{-3}	**52**

design of TO dye, the introduction of electron donor groups (EDG) or acceptor groups (EWG) at the benzothiazole of TO can induce spectral shifts by altering the localization of electron density and causing changes in highest occupied molecular orbital (HOMO)–lowest unoccupied molecular orbital (LUMO) gap energy[76,77]. In a previous report regarding HTO and several reports focused on quinoline PPGs,[55,56,78] the uncaging mechanism involved ICT during the excited state. The previous study of HTO showed that photolysis of HTO occurred via heterolysis, which generates ion pairs; moreover, the hydroxy group of HTO enhances ICT and improves photolytic efficiency. In a computational study of HTO-OAc to characterize its HOMO and LUMO (**Figure 26a**), the electron density of the HOMO was localized on the benzothiazole ring, whereas the electron density of the LUMO was localized on the quinoline. Therefore, a series of HTO analogues bearing EWG or EDG substituents on the benzothiazole ring were synthesized to investigate the effect of each substituent on the photolytic efficiency of HTO (**Figure 26b**, **Scheme 5**). Late-stage modifications of benzothiazole rings facilitated the preparation of a library of HTO analogues. Acetate was chosen as a model leaving group to simplify the synthesis. Methoxymethyl-protected 7-hydroxyquinoline derivatives (**Scheme 5**) were then conjugated with leaving groups, followed by *N*-alkylation. After the formation of HTO analogues with EWG- or EDG-substituted benzothiazole derivatives, target compounds were obtained by deprotection of the methoxymethyl groups. The spectroscopic properties of these HTO analogues are summarized in **Table 2**. The absorption maxima of EWG-substituted HTO derivatives, such as F-HTO-OAc and Cl-HTO-OAc, were slightly hypsochromically shifted relative to HTO-OAc, while the absorption maxima of EDG-substituted HTO derivatives, such as MeO-HTO-OAc and DiMeO-HTO-OAc, were bathochromically shifted. Dimethoxy substitution on the benzothiazole ring caused a 26-nm red shift in the absorption spectrum relative to HTO-OAc. The trends in spectral shifts of absorption maxima can be understood in terms of the effects of substituents on frontier orbitals. For HTO derivatives, the electron density

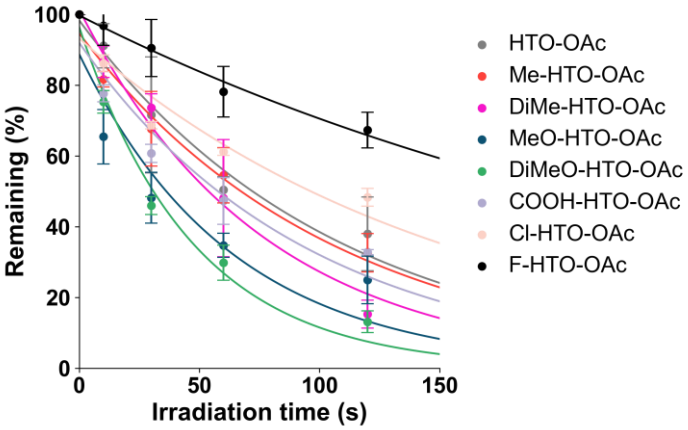

Figure 27. (d) Time courses of photolysis of HTO derivatives. Conditions: 50 μM HTO derivatives in PBS buffer/acetonitrile = 4:1. Light intensity = 10 mW/cm^2, λ = 490 ± 5 nm. Error bars represent the SD (N = 3).

of the HOMO is localized on the benzothiazole ring; therefore, EWGs on benzothiazole will stabilize the HOMO rather than the LUMO, leading to a larger HOMO–LUMO gap and blue-shifted spectra. In contrast, EDGs on the benzothiazole will destabilize the HOMO, leading to red-shift absorption.

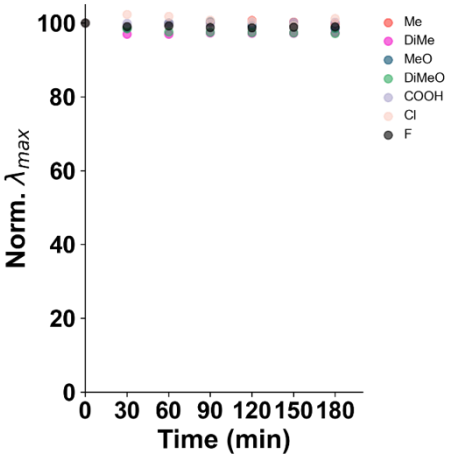

Figure 28. The stability of HTO derivatives solutions kept in the dark. No changes were found in the absorption spectra recorded after 180 min.

Next, the photolytic efficiencies of HTO derivatives carrying protected acetates were investigated using 490-nm light in phosphate-buffered saline (PBS) with 20% acetonitrile. The photolysis reactions that occurred over time were monitored by HPLC (**Figure 27**). As expected, EWG-substituted (e.g., fluoro, chloro) HTOs tended to have a lower photolytic efficiency than non-substituted HTO (HTO-OAc), whereas EDG-substituted HTOs had a higher photolytic efficiency (**Table 2**). These results suggested that the ICT caused by differences in electron density influenced the photolysis reaction. Our previous work showed that increases in the aprotic polar solvent percentage of the uncaging medium led to lower photolytic efficiency. Therefore, the photolytic efficiency of HTO-OAc ($\varepsilon\Phi$ = 141) in this report was below the previously reported value ($\varepsilon\Phi$ = 370 in PBS with 10% DMSO). However, to ensure that all compounds were dissolved in the solution, PBS with 20% acetonitrile was used as the uncaging medium. Among the EDG substitutes, dimethoxy substituents had the highest photolytic efficiency: $\varepsilon\Phi$ = 324, a 2.3-fold increase compared with the value determined for non-substituted HTO-OAc ($\varepsilon\Phi$ = 141). The photolytic efficiency of DiMeO-HTO-OAc was also higher than the efficiencies of commonly used BODIPY derivatives

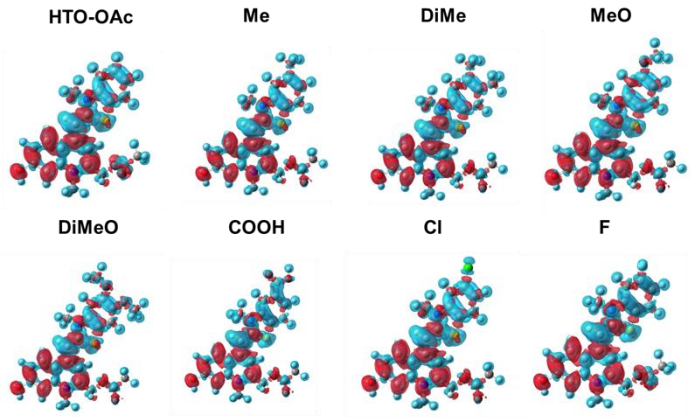

Figure 29. Electron density difference between the lowest-energy excited state and the ground state, $\Delta\rho = \rho(S_1) - \rho(S_0)$, as calculated at the PCM: B3LYP/6-31G(d,p) level in water. Blue (red) lobes are associated with negative (positive) $\Delta\rho$ values. isocontour value 0.0004 au.

($\varepsilon\Phi \leq 117$ in methanol)[42]. After 3 h in the dark, the HTO derivatives in PBS with 20% acetonitrile were stable (< 4% degradation) (**Figure 28**).

The ICT effects of the substitutes on photolytic efficiency were assessed by computing the density difference upon excitation ($\Delta\rho$) and photo-induced ICT, which were quantified in a well-established procedure based on the transferred charge (q_{CT}), associated charge-transfer distance, and dipole moment (μ).[79,80] The density differences in HTO derivatives upon excitation ($\Delta\rho$) are graphically depicted in (**Figure 29**). The density reduction moiety was mostly located on the benzothiazole ring, whereas the regions of density enhancement were on the quinoline moiety. These data showed that electrons were transferred from benzothiazole to the quinoline moiety. According to the DFT calculations, the introduction of EWGs or EDGs on the benzothiazole ring effectively influenced the transferred charge (q_{CT}) upon photo-induced excitation (**Table 3**). The largest q_{CT} was observed for dimethoxy(DiMeO)-substituted HTO, which had the highest photolytic efficiency among the HTO derivatives. A plot of the photolytic efficiency vs. the

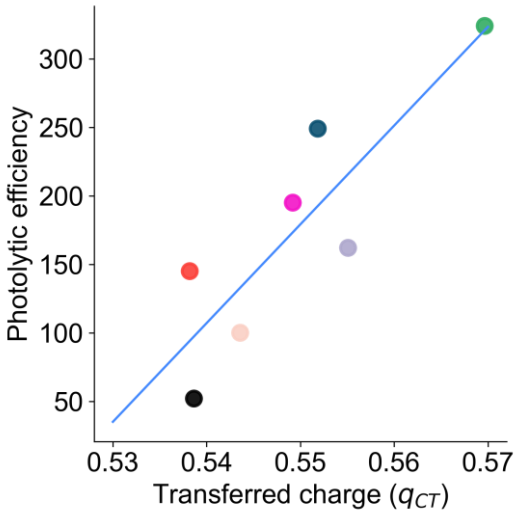

Figure 30. Correlation plots for electron donor–acceptor substituted HTO derivatives. Photolytic efficiency was plotted against the transferred charge (q_{CT}) and fitted to a linear curve (blue line).

Table 3. Charge transferred upon excitation (q_{CT},|e|), charge transfer distance (d_{CT}, Å) and transition dipole moment (μ_{CT}, D), calculated at the TDDFT CAM-B3LYP/6-31G(d,p) level in water.

Compound	CT charge (e)	CT distance (Ang)	CT dipole (Debye)
HTO-OAc	0.530	2.07	5.27
Me-HTO-OAc	0.538	2.06	5.32
DiMe-HTO-OAc	0.549	2.08	5.49
MeO-HTO-OAc	0.552	2.13	5.64
DiMeO-HTO-OAc	0.570	2.25	6.16
Cl-HTO-OAc	0.544	2.16	5.64
F-HTO-OAc	0.539	2.12	5.48
COOH-HTO-OAc	0.555	2.15	5.73

transferred charge (q_{CT}) of the HTO derivatives (**Figure 30**) showed a good correlation (r = 0.87), indicating that the large electron density transition involved enhanced photolytic efficiency.

Dimethoxy-substituted HTO was then used in the optical control of DNA recombination. In the synthesis of DiMeO-HTO caged cyclofen-OH (DiMeO-HTO-Ind) (**Figure 31a**), unwanted photochemical reactions, such as photo-Claisen rearrangement[68], were avoided by inserting the dimethylethylenediamine-carbamoyl self-immolating linker between DiMeO-HTO and the cyclofen-OH inducer (**Figure 31b**). The synthetic scheme for DiMeO-HTO-Ind is outlined **Scheme 6**. In briefly, the self-immolating linker was connected to TBDPS-protected 7-hydroxyquinoline derivatives by CDI coupling, followed by removal of the Boc-protecting group of the linker. Next, the 4-nitrophenylcarbonate-activated cyclofen derivative was allowed to react with the linker-hydroxyquinoline derivative conjugate. After the formation of HTO analogues with DiMeO-substituted benzothiazole derivatives, the deprotection of TBDPS and removal of the Boc protecting group resulted in DiMeO-HTO-Ind. The remaining photolysis and release kinetics of the free cyclofen-OH inducer were monitored by HPLC. Illumination with green light (490 nm, 20 mW/cm^2) for 5 min showed that only 5% of the DiMeO-HTO-Ind remained (**Figure 31c, d**); it also revealed the release of the linker-cyclofen-OH inducer conjugate (linker-Ind) (**Figure 32a**). The increased release of free cyclofen-OH inducer was also monitored by HPLC (**Figure 32b**). After incubation of DiMeO-HTO-Ind at 37°C for 2 h, the uncaging yield was ~82% (**Figure 31d**). Under the same conditions but without illumination, there was no release of cyclofen-OH inducer.

Scheme 6. Synthesis of DiMeO-HTO-Ind

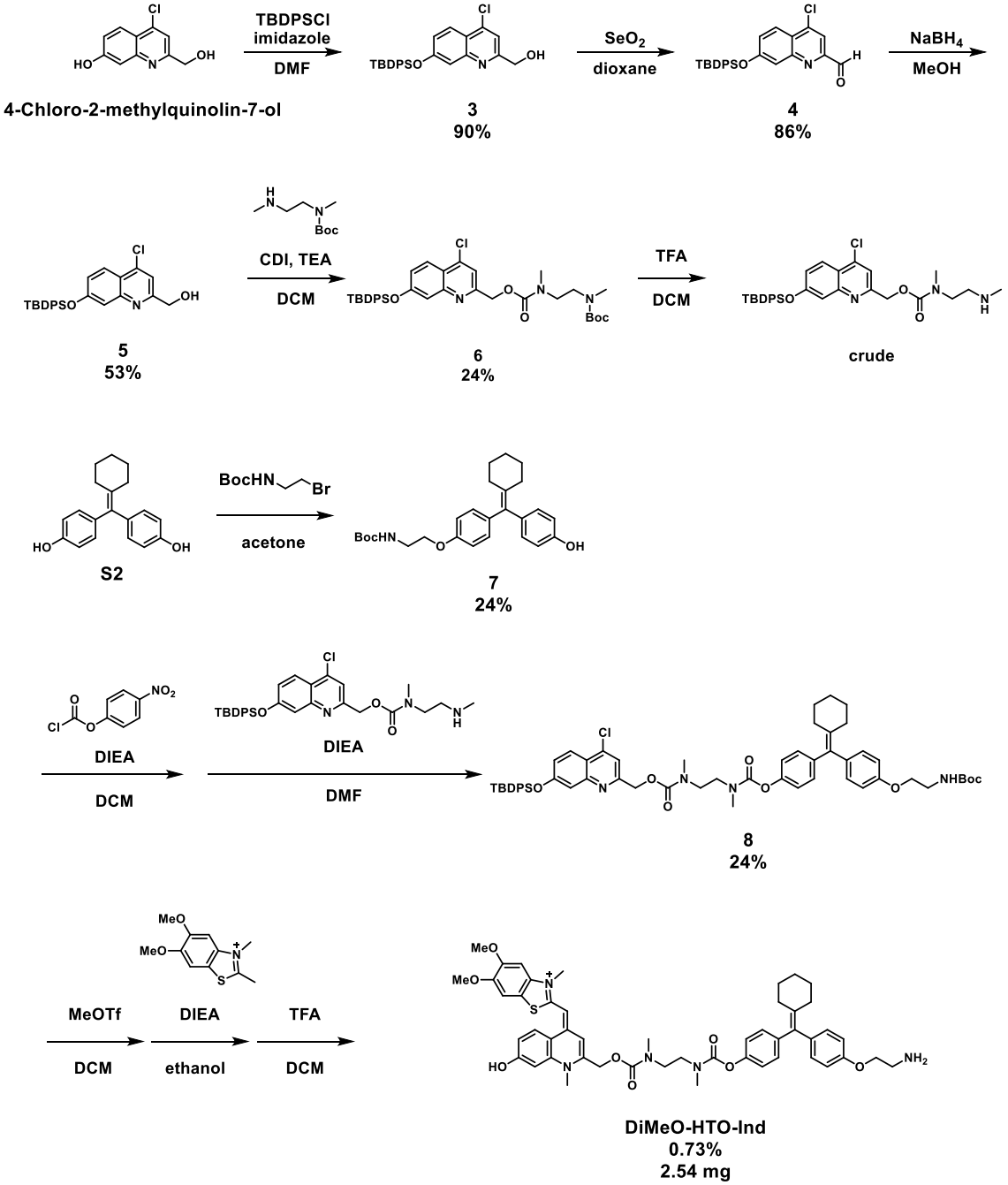

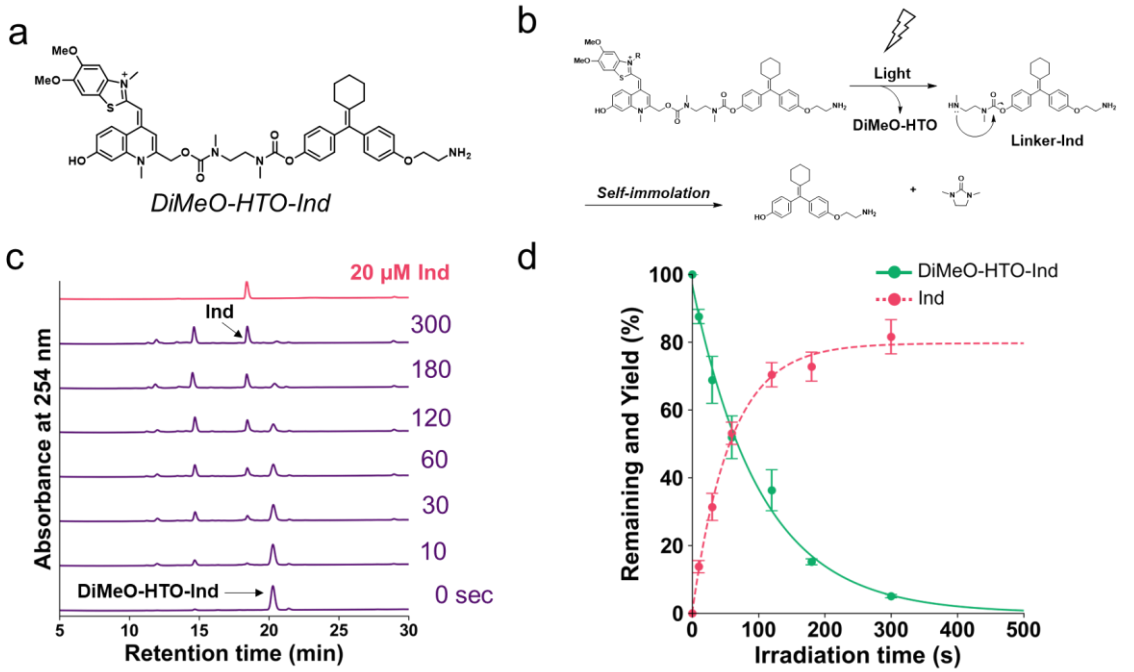

Figure 31. DiMeO-HTO caged cyclofen-OH inducer (DiMeO-HTO-Ind). (a) Structure of DiMeO-HTO-Ind. (b) Light-induced cleavage of the leaving group and subsequent self-immolating cyclization, resulting in the release of cyclofen-OH inducer. (c) HPLC-based time courses of the photolysis of DiMeO-HTO-Ind at 254 nm. Conditions: 25 μM DiMeO-HTO-Ind in PBS buffer/acetonitrile = 4:1. Light intensity = 20 mW/cm^2, λ = 490 ± 5 nm. (d) Quantitative monitoring of the reaction of DiMeO-HTO-Ind. Error bars represent the SDs (N = 3).

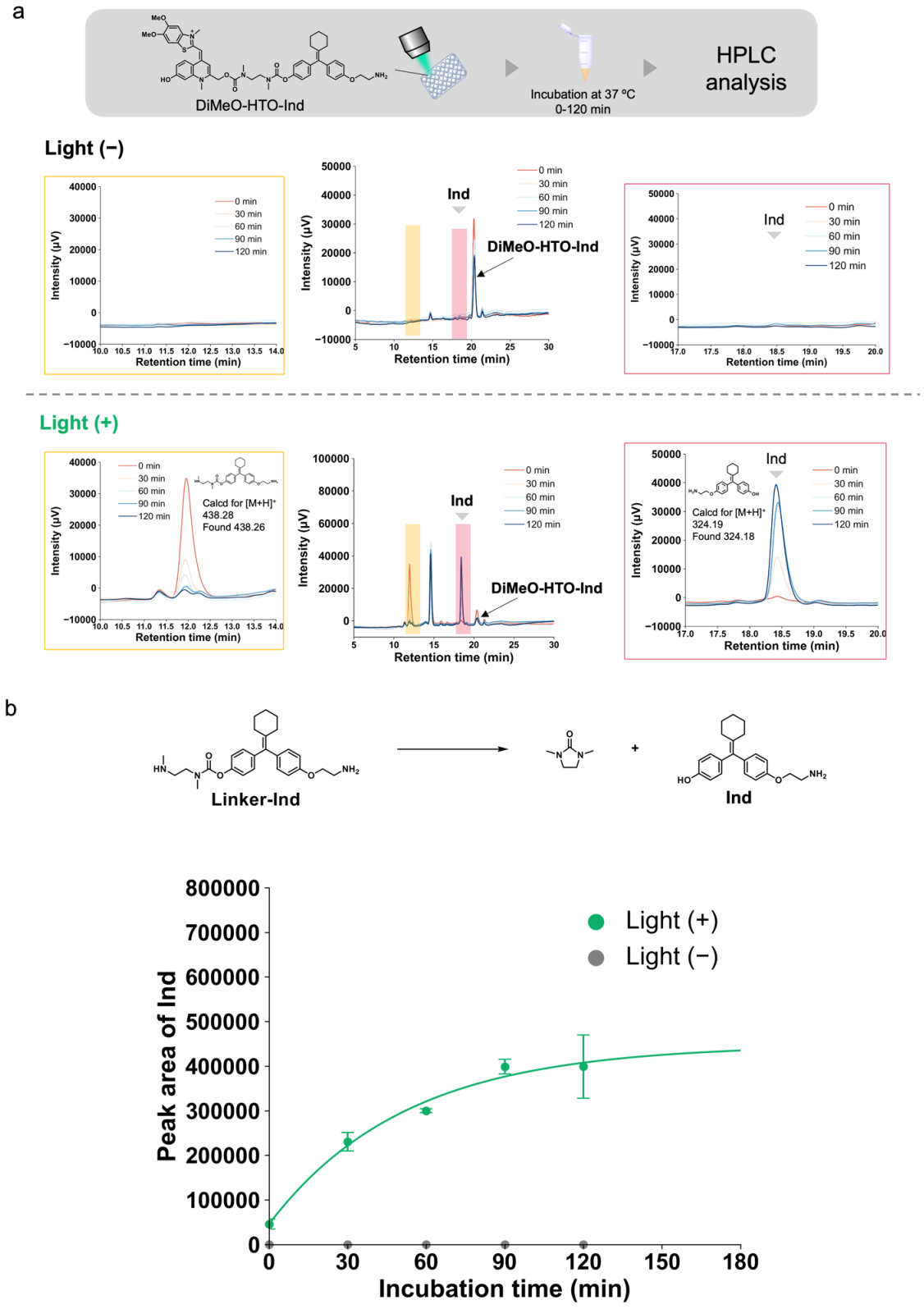

Figure 32. (a) Cyclofen-OH Inducer (Ind) release at 37 ºC (30 min intervals) from DiMeO-HTO-Ind (25 μM, PBS buffer/acetonitrile = 4:1). Light intensity = 20 mW/cm^2, λ = 490 ± 5 nm. Illumination period = 180 s. (b) Self-immolative kinetics of linker-appended Ind.

ER antagonists such as tamoxifen and its analogues are cytotoxic at a micromolar level, similar to cyanine-based caged ER antagonists.[18] In the cytotoxicity assay of DiMeO-HTO-Ind, whereas Ind exhibited cytotoxicity at concentrations > 10 µM, up to 100 µM DiMeO-HTO-Ind did not inhibit cell viability after 24 h of incubation (**Figure 33**). These results indicated that DiMeO-HTO-Ind can be used as a caged cyclofen-OH.

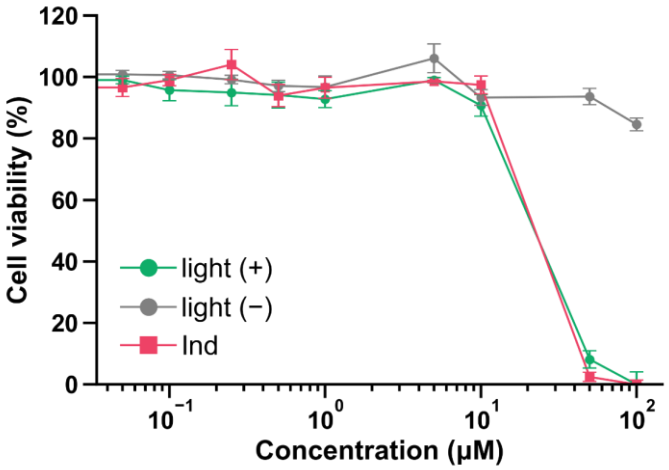

Figure 33. Cytotoxicity results for DiMeO-HTO-Ind and Ind at varying concentrations (0–100 µM) in HEK293T cells. Error bars represent the SD ($N = 3$).

Finally, the ability of illuminated DiMeO-HTO-Ind to induce gene recombination in live cells was examined. HEK293T cells were transfected with Cre-ERT2 and a loxP-mCherry-loxP-BFP plasmid, which contained a loxP-flanked red fluorescent protein (mCherry). After Cre-ERT2 binding of the ER ligand (Ind), loxP-flanked mCherry was deleted by the translocated Cre recombinase, leading to expression of blue fluorescent protein (BFP) (**Figure 34a**). HEK293T cells were treated with 250 nM DiMeO-HTO-Ind or 250 nM Ind alone, then incubated at 37°C for 5 min. The DiMeO-HTO-Ind-treated cells were either exposed for 3 min to green light (505 nm, 20 mW/cm^2) or kept in the dark prior to incubation at 37°C for 1 h. Next, they were washed with Hanks' balanced salt solution (HBSS), and the medium was replaced. After green-light illumination for 24 h, downstream BFP expression was observed by fluorescence microscopy and measured by flow cytometry. In the absence of green light, cells treated with DMSO alone or with DiMeO-HTO-Ind displayed minimal background BFP fluorescence (**Figure 34b**) and limited BFP expression (DMSO: 3.6%, no light: 4%) (**Figure 34 c, d**). In contrast, a large increase in BFP fluorescence and a 30% increase in BFP expression were observed among cells exposed to green light. These results demonstrated that DiMeO-HTO-Ind could control gene expression when used with the Cre-ERT2/loxP system. Whereas previous light-mediated Cre recombination with ONB or coumarin photocages required UV light irradiation, light-mediated control of Cre recombination via DiMeO-HTO-Ind at the same probe concentration (250 nM) as ONB or coumarin photocages was achieved with longer-wavelength (505 nm) light. Moreover, the illumination time required for sufficient

uncaging was considerably shorter for Ind than for cyanine photocages (DiMeO-HTO-Ind: 3 min vs cyanine: 30–60 min). These results reflect the excellent uncaging efficiency of DiMeO-substituted HTO. Among the advantages of DiMeO-HTO-Ind are its long-wavelength light activation, low loading concentration, and short illumination period. The ability of DiMeO-HTO-Ind to control gene expression with high spatial and temporal precision in vivo will lead to its use in many biological applications.

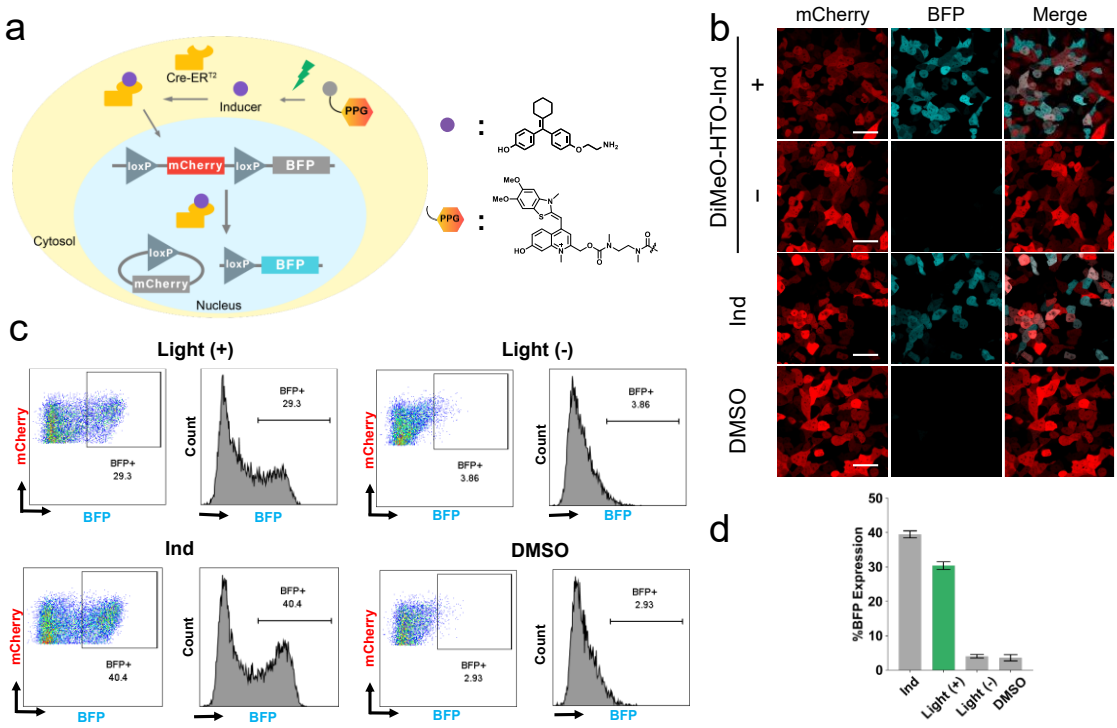

Figure 34. Light activation of Cre-ERT2 mediated BFP expression in HEK293T cells. (a) Photocontrol of Cre-ERT2 mediated BFP expression in HEK293T cells. (b) Confocal imaging of DiMeO-HTO-Ind treated HEK293T cells with light (505 nm, 20 mW/cm^2, for 3 min), without light (DMSO). Scale bar: 20 μm. (c) Flow cytometry analysis of light-dependent BFP expression in HEK293T cells. (d) Percentages of BFP-expressing cells, determined by flow cytometry, are shown with error bars (SD, $N = 4$).

Experimental Methods

General

All reagents were purchased from Tokyo Chemical Industries, Wako Pure Chemical, or Sigma-Aldrich Chemical Co. and used without further purification. Analytical thin-layer chromatography was performed on $^{60}F_{254}$ silica plates (Merck & Co., Inc.) and visualized under UV light. Flash auto purification was conducted using the Isolera Spectra (Biotage), with Biotage® Sfär HC and Sfär C18 D cartridges. Nuclear magnetic resonance (NMR) spectra were recorded using an AVANCE500HD instrument (Bruker), with ^{1}H NMR

spectra recorded at 500 MHz and ^{13}C NMR spectra recorded at 125 MHz; tetramethylsilane was used as an internal standard. FAB mass spectra were acquired using a JMS-700 mass spectrometer (JEOL). Electrospray ionization or Direct Analysis in Real Time (DART™) mass spectra were obtained using JMS-T100LP (JEOL). Matrix-assisted laser desorption/ionization (MALDI) mass spectra were obtained using JMS-S3000 (JEOL). Reversed-phase HPLC analyses were performed using an Inertsil ODS-3 column (4.6 × 250 mm; GL Sciences) or InertCore Plus C18 (4.6 × 100 mm; GL Sciences), along with an HPLC system comprising a pump (PU-2080; JASCO) and detector (MD-2010 plus and FP-2020; JASCO). Samples were injected using an autosampler (AS-4550; JASCO). Preparative HPLC separations were performed using an Inertsil ODS-3 column (10.0 × 250 mm; GL Sciences) and an HPLC system comprising a pump (PU-2087; JASCO) and detector (UV-2075; JASCO). Buffer A was composed of 0.1% trifluoroacetic acid (TFA) in H_2O or 0.1% HCOOH in H_2O; buffer B was composed of 0.1% TFA in acetonitrile or 0.1% HCOOH in acetonitrile.

One-photon uncaging and photochemical quantum yield determination

Photochemical quantum yields were obtained in HPLC time-course experiments. HTO compounds and internal standards (methyl 3-hydroxy-2-naphthoate) were irradiated using a Xe lamp (light intensity: 10 mW/cm^2, $\lambda_{ex} = 490 \pm 5$ nm) in a 4:1 (v/v) PBS/CH_3CN mixture containing 0.5% DMSO at room temperature. Relative peak areas were obtained via division of the peak area of the HTO compound by the peak area of the internal standard. The degradation rates of HTO compounds were determined by fitting a mono-exponential decay curve. Quantum yields for photolysis were determined using Eq. (1):

$$\Phi = (I\sigma t_{90\%})^{-1} \quad \text{(Eq. 1)}$$

where I is the photon flux in (Einstein·s^{-1}·cm^{-2}), σ is the decadic extinction coefficient (10^3 × molar extinction coefficient [ε]) at cm^2·mol^{-1}, and $t_{90\%}$ is the irradiation time (in s)

for 90% photoconversion to the product. The photon flux of the lamp I (2.9126×10^{-8} einstein$\cdot s^{-1} \cdot cm^{-2}$) was measured by potassium ferrioxalate actinometry.

Quantification of cyclofen-OH inducer

Cyclofen-OH inducer in PBS with 20% acetonitrile was quantified by HPLC. Buffer A contained 0.1% TFA in H_2O; buffer B contained 0.1% TFA in acetonitrile. Cyclofen-OH inducer (10, 20, 30, 40 μM) was used to prepare a calibration curve.

Computational methods

DFT and time dependent DFT (TD-DFT) calculations on all molecules were conducted using the Gaussian 09 program package[81]; they included the effects of the water or methanol solvent based on the polarization continuum model (PCM)[82]. The molecular geometries of the ground electronic state were optimized using DFT with the B3LYP function and 6-31G** basis set. No optimized structures had imaginary frequencies. Vertical excitations were obtained from single-point TD-DFT calculations with CAM-B3LYP/6-31G**.

Construction of plasmids

pCAG-ERT2CreERT2

Cre recombinase plasmids were obtained from Addgene (pCAG-ERT2CreERT2 (#13777)).[83]

pCALNL-loxP-mCherry-loxP-BFP

The DNA fragment of mCherry was prepared from pcDNA3.1-mCherry[84] (#128744; Addgene) by PCR using primers A and B (see Table S2 for sequence information). The mCherry fragment and the pCALNL-GFP vector[83] (#13770; Addgene) were digested with *Bcl*I and *Bst*BI, then ligated together to generate pCALNL-mCherry-GFP. The DNA fragment BFP was prepared from pTagBFP-actin (evrogen) by PCR using primers C and D (see Table S2 for sequence information). The BFP fragment and the pCALNL-

mCherry-GFP vector were digested with *Kpn*I and *Not*I, then ligated together to generate pCALNL-mCherry-BFP.

Table S2. The sequences of the oligonucleotide primers used for plasmid construction**.**

Primer name	Sequence
A	5‘-AAATGATCAATGGTGAGCAAGGG-3‘
B	5‘-AATTTCGAATTACTTGTACAGCTCGTCC-3‘
C	5‘-ATAGGTACC GCCACCATGAGCGAGCTG-3‘
D	5‘-GCAAACTGGGGCACAAGCTTAATTGAGCGGCCGC ATA-3‘

Cell culture

HEK293T cells were cultured in Dulbecco’s modified Eagle’s medium (DMEM) containing 10% fetal bovine serum and antibiotics (100 units penicillin/mL and 0.1 mg streptomycin/mL). HEK293T cells were transfected with plasmids using Lipofectamine 3000 (Invitrogen), in accordance with the manufacturer’s protocol. The transfected cells were maintained at 37°C throughout the experiments.

Cytotoxicity assay

HEK293T cells were re-plated into 96-well plates (1×10^4 cells/well) in DMEM containing 10% fetal bovine serum, then incubated overnight. Next, the cells were treated with the indicated concentrations of DiMeO-HTO-Ind or Ind. After 1 h of incubation, the cells were irradiated with a light-emitting diode (LED) light source (CL-1501; Asahi, λ_{ex} = 505 nm, light intensity = 20 mW/cm^2, irradiation period = 3 min). After 24 h of incubation, the PrestoBlue^{TM} cell viability reagent was added; cells were incubated with the reagent in accordance with the manufacturer’s guidelines. Cell viability was calculated by measuring the absorbance at 570 nm (experimental wavelength) and 600 nm (reference wavelength) using an M1000 microplate reader (Tecan).

Live-cell imaging of HEK293T cells

HEK293T cells were transfected with ERT2CreERT2 and loxP-mCherry-loxP-BFP using Lipofectamine 3000 (Invitrogen), in accordance with the manufacturer’s protocol. The

transfected cells were incubated with 5% CO_2 at 37°C for 24 h, after which the medium was removed and the cells were washed with HBSS. Subsequently, the cells were incubated with 250 nM cyclofen-OH or 250 nM DiMeO-HTO-Ind (0.5% DMSO) for 5 min, followed by light irradiation [light intensity: 20 mW/cm^2 for 3 min, λ_{ex} = 505 nm, LED light source; CL-1501 (Asahi)]. After 1 h incubation, the medium was removed and cells were washed with HBSS, then transferred to DMEM. After incubation with 5% CO_2 at 37°C for 23 h, probe-treated cells were examined using a confocal laser-scanning microscope with excitation wavelengths of 405 and 559 nm and emission wavelengths of 420–460 nm and 570–620 nm.

Measurement of genetic recombination efficiency by flow cytometry

HEK293T cells in DMEM containing 10% fetal bovine serum were re-plated into 96-well plates and allowed to reach near-confluency overnight. The cells were subsequently transfected with ERT2CreERT2 and loxP-mCherry-loxP-BFP using Lipofectamine 3000 (Invitrogen), in accordance with the manufacturer's protocol. After the transfected cells had been incubated with 5% CO_2 at 37°C for 24 h, the medium was removed and the cells were washed twice with HBSS; they were then incubated for 5 min with 250 nM DiMeO-HTO-Ind in DMEM (0.5% DMSO). Next, the cells were subjected to light irradiation (light intensity: 20 mW/cm^2, for 3 min, λ_{ex} = 505 nm) before incubation with 5% CO_2 at 37°C for 24 h. After removal of the medium, the cells were washed twice with PBS and incubated with cell dissociation buffer for 5 min. Subsequently, buffer was removed by centrifuging the cell suspension at 3,000 rpm for 3 min; the cell pellet was then resuspended in 1% fetal bovine serum in PBS. The genetic recombination efficiency of photoactivated DiMeO-HTO-Ind in HEK293T cells was measured using a flow cytometer (SH800S; SONY) as follows: laser, 405 and 561 nm; filter, 450 ± 25 nm and 600 ± 30 nm.

Synthesis of compound

Compound S1

Compound S1 was prepared according to published procedures.[71]

2,3,5-trimethylbenzo[d]thiazol-3-ium (Compound 1a)

Iodomethane (2608 mg, 18.4 mmol) was added to a solution of 2,5-dimethylbenzo[d]thiazole (1500 mg, 9.19 mmol) in acetonitrile (2.0 mL), and the solution

was refluxed for 12 h. The resulting precipitate was filtered under suction, washed with acetonitrile, and dried *in vacuo* to afford compound 1a (1480 mg, 6.60 mmol) as a white solid: ^{1}H NMR (500 MHz, DMSO-d_6) δ 8.14 (d, J = 8.0 Hz, 1H), 8.06 (s, 1H), 7.66 (d, J = 8.0 Hz, 1H), 4.84 (s, 3H), 4.25 (s, 3H), 2.64 (s, 3H); ^{13}C NMR 125 MHz, DMSO-d_6) δ 177.3, 142.3, 140.3, 130.0, 126.3, 124.5, 117.0, 36.6, 21.7, 17.6; HRMS (FAB+) Calcd for $[M]^+$,178.0685, found for 178.0684.

2,3,5,6-tetramethylbenzo[d]thiazol-3-ium (Compound 1b)

Compound 1b was synthesized as described for *2,3,5-trimethylbenzo[d]thiazol-3-ium* (1a) using 2,5,6-trimethylbenzothiazole (1500 mg, 8.47 mmol). The residue was washed with acetonitrile to afford compound 1b (1678 mg, 8.73 mmol, quant) as a white solid: ^{1}H NMR (500 MHz, DMSO-d_6) δ 8.15 (s, 1H), 8.11 (s, 1H), 4.16 (s, 3H), 3.13 (s, 3H), 2.47 (s, 3H), 2.43 (s, 3H); ^{13}C NMR (125 MHz, DMSO-d_6) δ 175.6, 140.7, 139.7, 138.4, 126.5, 124.1, 117.0, 36.6, 20.4, 20.2, 17.4; HRMS (FAB+) Calcd for $[M]^+$,192.0841, found for 192.0844.

5-methoxy-2,3-dimethylbenzo[d]thiazol-3-ium (Compound 1c)

Compound 1c was synthesized as described for *2,3,5-trimethylbenzo[d]thiazol-3-ium* (1a) using 5-methoxy-2-methylbenzothiazole (1500 mg, 8.38 mmol). The residue was washed with acetonitrile to afford compound 1c (1547 mg, 7.97 mmol) as a white solid:^{1}H NMR (500 MHz, DMSO-d_6) δ 8.29 (d, J = 8.0 Hz, 1H), 7.78 (d, J = 2.5 Hz, 1H), (dd, J = 8.0 Hz, J = 2.5 Hz, 1H), 4.18 (s, 3H), 3.97 (s, 3H), 3.14 (s, 3H); ^{13}C NMR (125 MHz, DMSO-d_6) δ 177.6, 161.1, 143.6, 125.6, 120.9, 118.3, 100.4, 56.9, 36.7, 17.6; HRMS (FAB+) Calcd for $[M]^+$,194.0634, found for 194.0643.

5,6-dimethoxy-2,3-dimethylbenzo[d]thiazol-3-ium (Compound 1d)

Compound 1d was synthesized as described for *2,3,5-trimethylbenzo[d]thiazol-3-ium* (1a) using 5,6-dimethoxy-2-methylbenzo[d]thiazole[85] (320 mg, 1.53 mmol). The residue was washed with acetonitrile to afford compound 1d (160 mg, 0.713 mmol) as a white solid: ^{1}H NMR (500 MHz, DMSO-d_6) δ 7.96 (s, 1H), 7.75 (s, 1H), 4.17 (s, 3H), 3.98 (s, 3H) 3.89 (s, 3H), 3.09 (s, 3H); ^{13}C NMR (125 MHz, DMSO-d_6) δ 173.2, 151.6, 150.4, 136.6, 121.4, 105.3, 99.3, 57.1, 56.7, 36.8, 17.2; HRMS (FAB+) Calcd for $[M]^+$,224.0740, found for 224.0743.

Tert-butyl 2-methylbenzo[d]thiazole-5-carboxylate

N,*N*-dimethylformamide di-*tert*-butyl acetal (3160 mg, 15.5 mmol) was added to a solution of 2-methylbenzo[d]thiazole-5-carboxylic acid (500 mg, 2.59 mmol) in toluene

(3.0 mL). After 20 min of stirring at 85°C, the mixture was diluted with dichloromethane (DCM), then washed with sat. $NaHCO_3$ *aq* and brine. The organic layer was dried over anhydrous Na_2SO_4. The solvent was evaporated, and the residue was purified by flash chromatography (2:3 EtOAc/hexane) to afford tert-butyl 2-methylbenzo[d]thiazole-5-carboxylat (184 mg, 0.820 mmol) as a colorless solid: (184 mg, 0.820 mmol) as a white solid: ^{1}H NMR (500 MHz, $CDCl_3$) δ 8.57 (d, *J* = 1.5 Hz, 1H), 7.99 (s, *J* = 8.0 Hz, *J* = 1.5 Hz, 1H), 7.84 (d, *J* = 8.0 Hz, *J* = 1.0 Hz, 1H), 2.85 (s, 3H), 1.63 (s, 9H); ^{13}C NMR 125 MHz, $CDCl_3$) δ 168.1, 165.5, 153.2, 140.0, 130.2, 125.3, 123.7, 121.0, 81.3, 28.2, 20.3; HRMS (FAB+) Calcd for $[M+H]^+$,250.0902, found for 250.0906.

5-(tert-butoxycarbonyl)-2,3-dimethylbenzo[d]thiazol-3-ium (Compound 1e)

Compound 1e was synthesized as described for *2,3,5-trimethylbenzo[d]thiazol-3-ium* (1a) using *tert*-butyl 2-methylbenzo[d]thiazole-5-carboxylate (183 mg, 0.734 mmol). The residue was washed with acetonitrile to afford compound 1e (184 mg, 0.696 mmol, quant) as a white solid: ^{1}H NMR (500 MHz, DMSO-d_6) δ 8.65 (d, *J* = 1.5 Hz, 1H), 8.53 (d, *J* = 8.5 Hz, 1H), 8.25 (dd, *J* = 8.5 Hz, *J* = 1.5 Hz, 1H), 4.26 (s, 3H), 3.20 (s, 3H) 1.62 (s, 9H); ^{13}C NMR (125 MHz, DMSO-d_6) δ 180.0, 164.2, 142.2, 133.4, 132.6, 128.3, 125.5, 117.9, 82.9, 36.8, 28.2, 17.7; HRMS (FAB+) Calcd for $[M+H]^+$,246.1053, found for 246.1045.

5-chloro-2,3-dimethylbenzo[d]thiazol-3-ium (Compound 1f)

Compound 1f was synthesized as described for *2,3,5-trimethylbenzo[d]thiazol-3-ium* (1a) using 5-chloro-2 methylbenzothiazole (1500 mg, 8.20 mmol). The residue was washed with acetonitrile to afford compound 1f (1338 mg, 6.76 mmol) as a white solid: ^{1}H NMR (500 MHz, DMSO-d_6) δ 8.54 (d, *J* = 2.0 Hz, 1H), 8.45 (d, *J* = 8.0 Hz, 1H), 7.88 (dd, *J* = 8.0 Hz, *J* = 2.0 Hz, 1H), 4.18 (s, 3H), 3.17 (s, 3H); ^{13}C NMR (125 MHz, DMSO-d_6) δ 178.6, 141.9, 133.7, 127.8, 127.1, 125.4, 166.3, 35.8, 16.7; HRMS (FAB+) Calcd for $[M]^+$,198.0139, found for 198.0145.

5-fluoro-2,3-dimethylbenzo[d]thiazol-3-ium (Compound 1g)

Compound 1g was synthesized as described for *2,3,5-trimethylbenzo[d]thiazol-3-ium* (1a) using 5-fluoro-2 methylbenzothiazole (1500 mg, 8.98 mmol). The residue was washed with acetonitrile to afford compound 1g (1240 mg, 6.81 mmol) as a white solid: ^{1}H NMR (500 MHz, DMSO-d_6) δ 8.49 (dd, *J* = 9.5 Hz, *J* = 5.0 Hz, 1H), 8.34 (dd, *J* = 8.0 Hz, *J* = 2.0 Hz, 1H), (td, *J* = 9.5 Hz, *J* = 2.5 Hz, 1H), 4.17 (s, 3H), 3.17 (s, 3H); ^{13}C NMR

(125 MHz, DMSO-d_6) δ 178.9, 160.8, 142.2, 126.0, 124.1, 116.1, 103.6, 35.9, 16.8; HRMS (FAB+) Calcd for $[M]^+$,183.0434, found for 182.0439.

General Procedure for the HTO-derivatives

Compounds 1-7 (2 equivalents) and *N*,*N*-diisopropylethylamine (2 equivalents) were added to a solution of S1 in ethanol (0.12-0.06 mmol). After the mixture had been stirred at room temperature for 3 h in the dark, the solvent was removed under reduced pressure and the residue was used in the next step without further purification. Crude product in DCM (4.00 mL) was mixed with TFA (1.00 mL) and stirred for 2 h; the solvent was removed under reduced pressure. The residue was purified by reversed-phase HPLC. Lyophilization of the sample produced the HTO derivatives as an orange powder.

(Z)-2-(acetoxymethyl)-4-((3,5-dimethylbenzo[d]thiazol-2(3H)-ylidene)methyl)-7-hydroxy-1-methylquinolin-1-ium (Me-HTO-OAc)

^{1}H NMR (500 MHz, MeOD) δ 8.35 (d, *J* = 9.5 Hz, 1H), 7.32 (s, 1H), 7.28 (s, 1H), 7.20-7.16 (m, 2H), 7.13 (s, 1H), 6.63 (s, 1H), 5.47 (s, 2H), 3.87 (s, 3H), 3.82 (s, 3H), 2.47 (s, 3H), 2.31 (s, 3H); ^{13}C NMR (125 MHz, MeOD) δ 170.2, 163.5, 160.0, 148.5, 148.3, 142.0, 140.6, 138.9, 126.7, 125.4, 121.6, 120.9, 117.7, 117.1, 112.3, 107.9, 100.7, 87.2, 62.6, 35.5, 32.5, 20.3, 19.4; HRMS (ESI+) Calcd for $[M]^+$,407.1424, found for 407.1441.

(Z)-2-(acetoxymethyl)-7-hydroxy-1-methyl-4-((3,5,6-trimethylbenzo[d]thiazol-2(3H)-ylidene)methyl)quinolin-1-ium (DiMe-HTO-OAc)

^{1}H NMR (500 MHz, MeOD) δ 8.24 (d, *J* = 9.0 Hz, 1H), 7.49 (s, 1H), 7.21 (s, 1H), 7.19 (s, 1H), 7.12 (d, *J* = 9.0 Hz, 1H), 7.05 (s, 1H), 5.44 (s, 2H), 3.81 (s, 3H), 3.78 (s, 3H), 2.34 (s, 3H), 2.34 (s, 3H), 2.34 (s, 3H); ^{13}C NMR (125 MHz, MeOD) δ 170.2, 163.6, 159.4, 147.9, 141.7, 138.6, 137.6, 133.9, 130.7, 126.5, 122.0, 121.1, 177.7, 116.8, 112.6, 107.5, 100.6, 87.1, 62.6, 35.4, 32.5, 19.4, 19.0, 18.4; HRMS (ESI+) Calcd for $[M]^+$,421.1580, found for 421.1584.

(Z)-2-(acetoxymethyl)-7-hydroxy-4-((5-methoxy-3-methylbenzo[d]thiazol-2(3H)-ylidene)methyl)-1-methylquinolin-1-ium (MeO-HTO-OAc)

^{1}H NMR (500 MHz, MeOD) δ 8.36 (d, *J* = 9.0 Hz, 1H), 7.65 (d, *J* = 7.5 Hz, 1H), 7.30 (s, 1H), 7.19 (d, *J* = 9.0 Hz, 1H), 7.14 (s, 1H), 6.94 (d, *J* = 7.5 Hz, 1H), 6.64 (s, 1H), 5.47 (s, 2H), 3.89 (s, 6H), 3.82 (s, 3H), 2.31 (s, 3H). ^{13}C NMR (125 MHz, DMSO-d_6) δ 170.3, 165.8, 160.4, 159.6, 148.8, 147.5, 142.4, 127.7, 123.6, 119.6, 116.4, 115.2, 112.0, 106.8,

101.7, 98.7, 98.4, 87.9, 63.2, 56.4, 36.8, 34.0, 21.2; HRMS (ESI+) Calcd for $[M]^+$,423.1373, found for 423.1381.

(Z)-2-(acetoxymethyl)-4-((5,6-dimethoxy-3-methylbenzo[d]thiazol-2(3H)-ylidene)methyl)-7-hydroxy-1-methylquinolin-1-ium (DiMeO-HTO-OAc)

^{1}H NMR (500 MHz, MeOD) δ 8.36 (d, *J* = 9.0 Hz, 1H), 7.54 (s, 1H), 7.26 (s, 1H), 7.68 (d, *J* = 9.0 Hz, 1H), 7.15 (s, 1H),7.12 (s, 1H) 5.45 (s, 2H), 3.95 (s, 3H), 3.92 (s, 6H), 3.87 (s, 3H), 2.30 (s, 3H). ^{13}C NMR (125 MHz, MeOD) δ 170.2, 162.5, 160.3, 150.8, 147.9, 147.7, 141.9, 134.7, 134.1, 126.6, 117.1, 116.8, 115.3, 107.5, 104.6, 100.1, 96.4, 87.4, 65.7, 55.8, 55.6, 35.2, 32.9, 19.4; HRMS (ESI+) Calcd for $[M]^+$,453.1479, found for 453.1484.

(Z)-2-(acetoxymethyl)-4-((6-carboxy-3-methylbenzo[d]thiazol-2(3H)-ylidene)methyl)-7-hydroxy-1-methylquinolin-1-ium (COOH-HTO-OAc)

^{1}H NMR (500 MHz, MeOD) δ 8.63 (d, *J* = 9.0 Hz, 1H), 8.07 (d, *J* = 8.0 Hz, 1H), 8.04 (s, 1H), 7.86 (dd, *J* = 8.0 Hz, *J* = 1.0 Hz, 1H), 7.34 (s, 1H),7.33 (d, *J* = 1.0 Hz, 1H), 7.27 (dd, *J* = 9.0 Hz, *J* = 1.0 Hz, 1H), 5.55 (s, 2H), 3.95 (s, 3H), 3.92 (s, 3H), 2.30 (s, 3H). ^{13}C NMR (125 MHz, MeOD) δ 170.3, 167.1, 163.1, 159.5, 150.0, 148.8, 142.1, 141.3, 131.0, 129.0, 128.2, 125.1, 123.3, 118.4, 117.5, 113.2, 107.7, 101.8, 88.4, 63.0, 37.2, 34.2, 21.2; HRMS (ESI+) Calcd for $[M]^+$,437.1166, found for 437.1179.

(Z)-2-(acetoxymethyl)-4-((5-chloro-3-methylbenzo[d]thiazol-2(3H)-ylidene)methyl)-7-hydroxy-1-methylquinolin-1-ium (Cl-HTO-OAc)

^{1}H NMR (500 MHz, MeOD) δ 8.32 (d, *J* = 8.0 Hz, 1H), 7.69 (d, *J* = 7.5 Hz, 1H), 7.43 (s, 1H), 7.30 (s, 1H), 7.24 (d, *J* = 7.5 Hz, 1H), 7.20 (d, *J* = 7.5 Hz, 1H), 7.19 (d, J_{ba} = 8.0 Hz, 1H), 7.14 (s, 1H), 5.49 (s, 2H), 3.91 (s, 3H), 3.77 (s, 3H), 2.32 (s, 3H); ^{13}C NMR (125 MHz, MeOD) δ 170.2, 164.5, 159.2, 148.8, 142.1, 141.6, 136.3, 134.0, 126.8, 123.8, 123.0, 122.3, 118.6, 117.2, 111.9, 108.2, 100.8, 87.6, 62.5, 35.8, 32.5, 19.4; HRMS (ESI+) Calcd for $[M]^+$, 427.0878, found for 427.0899.

(Z)-2-(acetoxymethyl)-4-((5-fluoro-3-methylbenzo[d]thiazol-2(3H)-ylidene)methyl)-7-hydroxy-1-methylquinolin-1-ium

^{1}H NMR (500 MHz, DMSO-d_6) δ 8.44 (m, 1H), 7.93 (d, *J* = 7.5 Hz, 1H), 7.58 (d, *J* = 9.0 Hz, 1H), 7.22 (s, 1H), 7.14 (m, 3H), 6.67 (s, 1H), 5.50 (s, 2H), 3.83 (s, 6H), 2.27 (s, 3H); ^{13}C NMR (125 MHz, DMSO-d_6) δ 170.3, 163.8, 161.9, 158.8, 148.8, 147.9, 142.9, 127.6,

124.4, 124.3, 119.3, 116.3, 111.3, 111.1, 106.7, 100.7, 100.4, 88.2, 63.1, 37.0, 34.0, 21.2; HRMS (ESI+) Calcd for $[M]^+$, 411.1173, found for 411.1191.

7-((tert-butyldiphenylsilyl)oxy)-4-chloro-2-methylquinoline (compound 3)

Imidazole (0.71 g, 10.4 mmol) and *tert*-butyldiphenylchlorosilane (0.098 mL, 1.30 mmol) were added under a nitrogen atmosphere to a solution of 4-chloro-2-methylquinolin-7-ol[71] (1.00 g, 5.18 mmol) in dry dimethylformamide (10 mL). After the mixture had been stirred for 4 h, it was diluted with 1:1 EtOAc/hexane, then washed with 5% $NaHCO_3$ *aq*, water, and brine. The organic layer was dried over anhydrous Na_2SO_4. The solvent was evaporated, and the residue was purified by flash chromatography (5:1 EtOAc/hexane) to afford compound 3 as a colorless solid (2.00 g, 4.64 mmol): ^{1}H NMR (500 MHz, $CDCl_3$) δ 7.92 (d, J = 9.0 Hz, 1H), 7.93-7.73 (m, 4H), 7.43-7.39 (m, 6H), 7.37-7.33 (d, J = 2.5 Hz, 1H), 7.19 (s, 1H) 7.01 (dd, J = 9.0 Hz, J = 2.5 Hz, 1H), 2.60 (s, 3H), 1.13 (s, 9H); ^{13}C NMR (125 MHz, $CDCl_3$) δ 159.2, 157.5, 150.1, 142.3, 135.5, 134.8, 130.1, 127.9, 127.7, 125.0, 122.3, 119.9, 116.1, 26.5, 25.1, 19.5; HRMS (DART+) Calcd for $[M+H]^+$,432.1545, found for 432.1545.

7-((tert-butyldiphenylsilyl)oxy)-4-chloroquinoline-2-carbaldehyde (compound 4)

Selenium dioxide (1.18 g, 10.7 mmol) was added to a solution of compound 3 (4.18 g, 9.70 mmol) in dioxane (60 mL). The reaction mixture was stirred for 1 h at 90°C, cooled to room temperature, and diluted with MeOH (40 mL). After the addition of silica gel (12 g), the mixture was concentrated to dryness and then purified by column chromatography (2:8 EtOAc/hexane) to afford compound 4 (3.72 g, 8.33 mmol) as a yellow solid: ^{1}H NMR (500 MHz, $CDCl_3$) δ 10.03 (s, 1H), 8.06 (d, J = 9.0 Hz, 1H), 7.89 (s, 1H), 7.76-7.74 (m, 4H), 7.50 (d, J = 2.0 Hz, 1H) 7.47-7.43 (m, 2H), 7.41-7.39 (m, 4H), 7.32 (dd J = 9.0 Hz, J = 2.0 Hz, 1H), 1.16 (s, 9H); ^{13}C NMR (125 MHz, $CDCl_3$) δ 192.8, 158.2, 152.6, 150.2, 143.8, 135.5, 131.8, 130.3, 129.7, 128.0, 126.0, 125.4, 117.4, 115.7, 26.4, 19.5; HRMS (DART+) Calcd for $[M+H]^+$,446.1338, found for 446.1334.

(7-((tert-butyldiphenylsilyl)oxy)-4-chloroquinolin-2-yl)methanol (compound 5)

$NaBH_4$ was added to a solution of compound 4 (3.70 g, 8.58 mmol) in methanol (50 mL). The reaction mixture was stirred for 15 min and diluted with EtOAc, then washed with water followed by brine. The organic layer was dried over Na_2SO_4 and the solvent was evaporated to afford compound 5 (1.98 g, 4.42 mmol) as a yellow solid: ^{1}H NMR (500 MHz, $CDCl_3$) δ 7.96 (d, J = 9.0 Hz, 1H), 7.76-7.74 (m, 4H), 7.46-7.42 (m, 2H), 7.40-7.42 (m, 4H), 7.35 (d, J = 2.5 Hz, 1H), 7.19 (s, 1H), 7.16 (dd, J = 9.0 Hz, J = 2.5 Hz, 1H), 4.78 (s, 2H), 1.14 (s, 9H); ^{13}C NMR (125 MHz, $CDCl_3$) δ 159.3, 157.8, 148.9, 143.0,

135.5, 132.1, 130.1, 128.0 125.3, 122.9, 121.0, 116.3, 116.1, 63.8, 26.5, 19.5; HRMS (DART+) Calcd for $[M+H]^+$,448.1494, found for 448.1505.

tert-butyl ((7-((tert-butyldiphenylsilyl)oxy)-4-chloroquinolin-2-yl)methyl) ethane-1,2 diylbis(methylcarbamate) (compound 6)

Compound 5 (800 mg, 1.79 mmol) was dissolved in dry DCM (20 mL) under a nitrogen atmosphere. 1,1'-Carbonyldiimidazole (435 mg, 2.68 mmol) was added, and the mixture was stirred at 0°C for 1 h; this was followed by the addition of *tert*-butyl methyl(2-(methylamino)ethyl) carbamate (673 mg, 3.58 mmol) and Et_3N (499 μL, 3.58 mmol) at 0°C. After the mixture had been stirred at room temperature for 23 h, the solvent was concentrated under reduced pressure and diluted with DCM, then washed with water and brine. The organic layer was dried over anhydrous Na_2SO_4. The solvent was evaporated and the residue was purified by flash chromatography (2:3 EtOAc/hexane) to afford compound 6 (803 mg, 1.37 mmol) as a colorless solid: ^{1}H NMR (500 MHz, $CDCl_3$) δ 7.96 (d, *J* = 8.0 Hz, 1H), 7.52-7.73 (m, 4H) 7.44-7.41 (m, 2H), 7.38-7.35 (m, 6H), 7.18-7.16 (m, 1H), 5.27 (s, 2H), 3.45-3.37 (m, 4H), 3.01-2.98 (m, 3H), 2.90-2.78 (m, 3H), 1.43 (s, 9H), 1.14 (s, 9H);^{13}C NMR (125 MHz, $CDCl_3$) δ 171.2, 157.7, 149.9, 143.6, 143.1 135.5, 132.1, 130.2, 130.1, 128.0, 125.1, 123.3, 121.1, 117.4, 116.4, 67.7, 60.4, 46.8, 34.6, 28.4, 26.4, 21.1, 19.5, 14.2; HRMS (DART+) Calcd for $[M+H]^+$, 662.2812, found for 662.2831.

***tert*-butyl (2-(4-(cyclohexylidene(4-hydroxyphenyl)methyl)phenoxy)ethyl)carbamate (compound 7)**

Tert-butyl (2-bromoethyl)carbamate (0.963 g, 4.32 mmol) and compound S2[69] (1.10g, 3.93 mmol) were dissolved in a solution of acetone (20 mL) and treated with K_2CO_3 (0.543 g, 3.93 mmol). The mixture was refluxed at 80°C for 24 h, the solids were filtered off, and the filtrate was evaporated. The residue was purified on a reversed-phase column (0–100% 0.1% HCOOH in water/0.1% HCOOH in MeCN, linear gradient). After lyophilization of the sample, a colorless powder of compound 7 was obtained (0.391 g, 0.924 mmol). ^{1}H NMR (500 MHz, MeOD) δ 6.96 (d, *J* = 9.0 Hz, 2H), 6.87 (d, *J* = 9.0 Hz, 2H), 6.82 (d, *J* = 9.0 Hz, 2H), 6.67 (d, *J* = 9.0 Hz, 2H), 3.97 (t, *J* = 5.5 Hz, 2H), 3.40 (t, *J* = 5.5 Hz, 2H), 2.24-2.21 (m, 4H), 1.63-1.56 (m, 6H), 1.43 (s, 9H); ^{13}C NMR (125

MHz, MeOD) δ 159.2, 157.4, 139.4, 138.2, 136.6, 136.2, 132.5, 116.2, 115.6, 80.9, 68.6, 41.7, 34.1, 30.4, 29.4, 28.6; HRMS (FAB+) Calcd for $[M]^+$,423.2410, found for 423.2417.

tert-butyl (2-(4-(cyclohexylidene(4-(((4-nitrophenoxy)carbonyl)oxy)phenyl)methyl)phenoxy)ethyl)carbamate (compound 8)

Compound 7 (200 mg, 0.473 mmol) in DCM (6.0 mL) was mixed with 4-nitrophenyl chloroformate (190 mg, 0.945 mmol) and *N*,*N*-diisopropylethylamine (165 μL, 0.945 mmol), stirred at room temperature for 3 h, concentrated onto silica gel, and purified by flash chromatography (1:4 EtOAc/hexane) to afford compound 7-PNP. Compound 6 (200 mg, 0.302 mmol) in DCM (4.00 mL) was mixed with TFA (1.00 mL) and stirred for 1 h; the solvent was subsequently removed under reduced pressure. The residue was used in the next step without further purification. Crude dimethylformamide (4.00 mL) was mixed with compound 7-PNP (134 mg, 0.228 mmol) and *N*,*N*-diisopropylethylamine (79 μL, 0.456 mmol), then stirred at room temperature for 1 h; next, the solvent was removed under reduced pressure. The residue was purified by flash chromatography (1:10 MeOH/DCM) to afford compound 8 (183 mg, 0.181 mmol) as a colorless solid: ^{1}H NMR (500 MHz, $CDCl_3$) δ 7.94-7.91 (m, 1H), 7.45-7.73 (m, 4H), 7.44-7.41 (m, 2H), 7.38-7.33 (m, 6H), 7.15 (dd, J = 9.5 Hz, J = 2.5 Hz, 1H), 7.04 (d, J = 8.0 Hz, 2H), 7.00 (d, J = 8.0 Hz, 2H), 6.94 (d, J = 8.0 Hz, 2H), 5.28-5.25 (m, 2H), 3.98 (t, J = 5.0 Hz, 2H), 3.56-3.51 (m, 6H), 3.10-3.04 (m, 3H),.3.00-2.88 (m, 3H), 2.24-2.21 (m, 4H), 1.58-1.54 (m, 6H), 1.44 (s, 9H), 1.13 (s, 9H); ^{13}C NMR (125 MHz, $CDCl_3$) δ 171.2, 157.7, 156.9, 156.1, 155.9, 155.8, 154.6, 149.9, 143.1, 140.4, 139.2, 135.9, 135.5, 133.1, 132.1, 131.0, 130.7, 130.6, 130.2, 128.0, 125.1, 123.3, 121.1, 121.0, 116.4, 113.8, 79.5, 67.7, 67.1, 60.4, 40.1, 34.8, 32.5, 28.7, 28.4, 26.8, 26.4, 21.1, 19.5, 14.2; HRMS (MALDI+) Calcd for $[M]^+$, 1011.4448, found for 1011.4490.

DiMeO-HTO-Ind

Methyl trifluoromethanesulfonate (8 μL, 0.0791 mmol) was added dropwise to a solution of compound 8 (40 mg, 0.396 mmol) in DCM (2.0 mL). The reaction mixture was stirred at room temperature for 4 h and concentrated *in vacuo*. The residue was used in the next step without further purification. Compound 1d (17.9 mg, 0.0800 mmol) and *N*,*N*-diisopropylethylamine (14 μL, 0.0139 mmol) were added to the residue in ethanol (2.0 mL). The mixture was stirred at room temperature for 3 h in the dark, after which the solvent was removed under reduced pressure. TFA (1.00 mL) was added to a solution of crude product in DCM (4.00 mL). The mixture was stirred for 2 h and the solvent was removed under reduced pressure. The residue was purified by reversed-phase HPLC under the following conditions: A/B = 80/20 (0 min), 40/60 (30 min), (solvent A: 0.1%

TFA in H_2O; solvent B: 0.1% TFA in CH_3CN). After lyophilization, a purple powder of DiMeO-HTO-Ind (2.54 mg, 0.0029 mmol) was obtained: ^{1}H NMR (500 MHz, DMSO-d_6) δ 8.62-8.56 (m, 1H), 7.63-7.56 (m, 1H), 7.43-7.41 (m, 1H), 7.26 (s, 1H), 7.24-7.20 (m, 2H), 6.99-6.90 (m, 6H), 6.88-6.84 (m, 2H), 6.97 (s, 1H), 5.50-5.45 (m, 2H), 4.14-4.10 (m, 2H), 4.00 (s, 3H), 3.92 (s, 3H), 3.88-3.87 (m, 3H), 3.83-3.78 (m, 3H), 3.64-3.58 (m, 4H), 3.23-3.19 (m, 2H), 3.10-3.02 (m, 3H), 2.95-2.84 (m, 3H), 2.10-1.99 (m, 4H), 1.52-1.39 (m, 6H); ^{13}C NMR (125 MHz, DMSO-d_6) δ 161.5, 159.0, 157.4, 157.0, 155.6, 153.3, 149.6, 148.8, 146.6, 146.1, 140.9, 139.0, 137.7, 134.7, 134.1, 132.1, 129.8, 129.4, 126.8, 120.6, 116.4, 116.0, 114.0, 113.6, 105.6, 104.6, 100.8, 96.8, 87.2, 63.7, 55.8, 55.7, 37.8, 34.3, 34.1, 34.0, 33.9, 33.6, 31.1, 31.0, 27.4, 27.3, 25.5; HRMS (MALDI+) Calcd for $[M]^+$, 874.3823, found for 874.3844.

Reference

[66] R. Feil, J. Brocard, B. Mascrez, M. Lemeur, D. Metzger, P. Chambon, *Proc. Natl. Acad. Sci. USA* **1996**, *93*, 10887–10890.

[67] G. C. R. Ellis-Davies, *Nat. Methods* **2007**, *4*, 619–628.

[68] P. T. Wong, E. W. Roberts, S. Tang, J. Mukherjee, J. Cannon, A. J. Nip, K. Corbin, M. F. Krummel, S. K. Choi, *ACS Chem. Biol.* **2017**, *12*, 1001–1010.

[69] L. Fournier, C. Gauron, L. Xu, I. Aujard, T. Le Saux, N. Gagey-Eilstein, S. Maurin, S. Dubruille, J. B. Baudin, D. Bensimon, M. Volovitch, S. Vriz, L. Jullien, *ACS Chem. Biol.* **2013**, *8*, 1528–1536.

[70] X. Lu, S. S. Agasti, C. Vinegoni, P. Waterman, R. A. Depinho, R. Weissleder, *Bioconjug Chem* **2012**, *23*, 1945–1951.

[71] R. Hashimoto, M. Minoshima, S. Sakata, F. Ono, H. Ishii, Y. Watakabe, T. Nemoto, S. Yanaka, K. Kato, K. Kikuchi, *Chem. Sci.* **2022**, *13*, 7462–7467.

[72] N. Rubinstein, P. Liu, E. W. Miller, R. Weinstain, *Chem. Commun.* **2015**, *51*, 6369–6372.

[73] H. Janeková, M. Russo, U. Ziegler, P. Štacko, *Angew. Chem. Int. Ed.* **2022**, *61*,

[74] J. M. Amatrudo, J. P. Olson, G. Lur, C. Q. Chiu, M. J. Higley, G. C. R. Ellis-Davies, *ACS Chem. Neurosci.* **2014**, *5*, 64–70.

[75] M. Klausen, V. Dubois, G. Clermont, C. Tonnelé, F. Castet, M. Blanchard-Desce, *Chem. Sci.* **2019**, *10*, 4209–4219.

[76] A. A. Vasilev, M. I. Kandinska, S. S. Stoyanov, S. B. Yordanova, D. Sucunza, J. J. Vaquero, O. D. Castaño, S. Baluschev, S. E. Angelova, *Beilstein. J. Org. Chem.* **2017**, *13*, 2902–2914.

[77] E. E. Rastede, M. Tanha, D. Yaron, S. C. Watkins, A. S. Waggoner, B. A. Armitage, *Photochem. Photobiol. Sci.* **2015**, *14*, 1703–1712.

[78] N. Asad, D. Deodato, X. Lan, M. B. Widegren, D. L. Phillips, L. Du, T. M. Dore, *J. Am. Chem.*

Soc. **2017**, *139*, 12591–12600.

[79] T. Le Bahers, C. Adamo, I. Ciofini, *J. Chem. Theory. Comput.* **2011**, *7*, 2498–2506.

[80] D. Jacquemin, T. Le Bahers, C. Adamo, I. Ciofini, *Phys. Chem. Chem. Phys.* **2012**, *14*, 5383–5388.

[81] M. J. Frisch, G. W. Trucks, H. B. Schlegel, G. E. Scuseria, M. A. Robb, J. R. Cheeseman, G. Scalmani, V. Barone, B. Mennucci, G. A. Petersson, H. Nakatsuji, M. Caricato, X. Li, H. P. Hratchian, A. F. Izmaylov, J. Bloino, G. Zheng, J. L. Sonnenberg, M. Hada, M. Ehara, K. Toyota, R. Fukuda, J. Hasegawa, M. Ishida, T. Nakajima, Y. Honda, O. Kitao, H. Nakai, T. Vreven, J. A. Montgomery, J. E. Peralta, F. Ogliaro, M. Bearpark, J. J. Heyd, E. Brothers, K. N. Kudin, V. N. Staroverov, R. Kobayashi, J. Normand, K. Raghavachari, A. Rendell, J. C. Burant, S. S. Iyengar, J. Tomasi, M. Cossi, N. Rega, J. M. Millam, M. Klene, J. E. Knox, J. B. Cross, V. Bakken, C. Adamo, J. Jaramillo, R. Gomperts, R. E. Stratmann, O. Yazyev, A. J. Austin, R. Cammi, C. Pomelli, J. W. Ochterski, R. L. Martin, K. Morokuma, V. G. Zakrzewski, G. A. Voth, P. Salvador, J. J. Dannenberg, S. Dapprich, A. D. Daniels, Ö. Farkas, J. B. Foresman, J. V Ortiz, J. Cioslowski, D. J. Fox, *Gaussian 09*, Gaussian, Inc, Wallingford CT, **2009**.

[82] J. Tomasi, B. Mennucci, E. Cance, *J. Mol. Struct.* **2018**, *464*, 211–226.

[83] T. Matsuda, C. L. Cepko, *Proc. Natl. Acad. Sci. USA* **2007**, *104*, 1027–1032.

[84] B. Kleaveland, C. Y. Shi, J. Stefano, D. P. Bartel, *Cell* **2018**, *174*, 350-362.e17.

[85] M. C. Henry, V. M. Abbinante, A. Sutherland, *European J. Org. Chem.* **2020**, *2020*, 2819–2826.

Conclusions and Perspectives

Light provides a noninvasive tool to perturb or probe biological systems by incorporating active-targeting reporters or light-responsive triggers in synthetic compounds. This thesis has described pH-activatable fluorescent probes for deep bone cavities and photo-activatable tools (caged compounds) to investigate biological processes in living systems.

In Chapter 1, a new fluorescent pHocas-RIS probe containing a risedronate fragment with moderate bone-binding affinity has been used to visualize the pH environments of osteocytic lacunae in bone tissue. Intravital two-photon fluorescent imaging studies using this probe revealed the presence of acidic regions on bone surfaces produced through the action of acid secreting osteoclasts that are responsible for dissolving bone mineral. This new probe was shown to be able to penetrate deep within bone tissues, which enabled it to be used for in vivo imaging of osteocytic lacunae containing bone resorbing osteocytes that produce acidic microenvironments. The author anticipates that the use of these probes in tandem with transgenic mice that express fluorescently labeled bone cells will enable real time imaging of osteocyte mediated bone resorptive processes that are important in remodeling bone-matrix in aging, health, and disease.

In Chapter 2, a new class of visible (one-photon) and near-infrared (two-photon) light-sensitive PPGs based on an HTO chromophore has been developed. The photolytic efficiencies of HTO-caged compounds were superior to those of reported visible-light-responsive PPGs in aqueous conditions. Caged glutamate (Sul-HTO-Glu) was efficiently photolyzed by 2PE at 940 nm. These results demonstrate that HTO-caged compounds can immediately release biomolecules and activate target biological functions using visible/NIR-light illumination. Moreover, Sul-HTO-Glu was shown to activate NMDA receptors in *Xenopus* oocytes and mammalian HEK293T cells, which will enable its use in the optical control of neural circuits. The author expects that the excellent optical properties of HTO will allow the control of biological functions in deeper tissue *in vivo*. The HTO light activation system can also be extended to a wide range of bioactive molecules such as drugs, peptides, and neurotransmitters. Furthermore, modification of HTO by replacing benzothiazole with other heterocyclic compounds enables the extension of the π-conjugate systems, which could provide long-wavelength visible/NIR-light-sensitive PPGs.

In Chapter 3, the author created PPG scaffolds that exhibit efficient photolysis in response to visible light, and then utilized them to achieve optical control of gene recombination in a Cre-ERT2/loxP system. Multiple HTO-caged derivatives bearing

EWG or EDG on the benzothiazole ring were synthesized. The introduction of EDGs, including a dimethoxy (DiMeO) substituent, significantly improved the photochemical properties of HTO-Ind. Theoretical calculations indicated a good correlation between photolytic efficiency and the transferred charge (q_{CT}) upon photo-induced excitation, implying that the EDG on the benzothiazole ring accelerates ICT to enhance the photochemical cleavage reaction. The use of DiMeO-HTO PPG in conjunction with a caged ER ligand (DiMeO-HTO-Ind) resulted in efficient photolysis of the ligand by green light and the release of the cyclofen-OH inducer with a maximum yield of 82%. Visible-light-induced Cre recombination involving DiMeO-HTO-Ind was confirmed by fluorescence imaging and flow cytometry. The high photolytic efficiency of DiMeO-HTO in the presence of green light allowed gene expression to be controlled at sub-micromolar concentrations of DiMeO-HTO-Ind. Anticipated applications of DiMeO-HTO-Ind include photoactivation of recombination and protein expression in Cre/loxP transgenic mice. Furthermore, this new generation of HTO-caged compounds will expand the use of visible light-sensitive caged compounds to include multicolor uncaging or photoactivated chemotherapy, as well as light-mediated control of bioactivity in vivo.

The author developed light responsive molecular probes that can visualize or activate targeted biological function in vivo by installing an active-targeting moiety or visible/NIR light removable protecting groups. These chemical probes can investigate cellular function with high spatial and temporal resolution in vivo, which will contribute to understanding biological function and drug development. Moreover, a combination of active-targeting moiety with visible/NIR light-responsive caged compound will offer a promising chemical tool that allows site-specific delivery and controlled release of a fluorescent probe or bioactive molecule in complexed in vivo system.

List of Publications

1) An Acid Activatable Fluorescence Probe for Imaging Osteocytic Bone Resorption Activity in Deep Bone Cavities

   Ryu Hashimoto, Masafumi Minoshima, Junichi Kikuta, Shinya. Yari, Steven D. Bull, Masaru Ishii, and Kazuya Kikuchi

   Angew. Chem. Int. Ed., **2020**, *59*, 20996-21000.

2) Efficient Visible/NIR Light-driven Uncaging of Hydroxylated Thiazole Orange-based Caged Compounds in Aqueous Media

   Ryu Hashimoto, Masafumi Minoshima, Souhei Sakata, Fumihito Ono, Hirokazu Ishii, Yuki Watakabe, Tomomi Nemoto, Saeko Yanaka, Koichi Kato, and Kazuya Kikuchi

   Chem. Sci. **2022**, *13*, 7462–7467.

3) Rational Design of Hydroxylated Thiazole Orange Photocages for Green Light-Triggered DNA Recombination

   Ryu Hashimoto, Masafumi Minoshima, and Kazuya Kikuchi

   ChemBioChem accepted.

Acknowledgments

The author is most grateful to Professor Kazuya Kikuchi for his continuous guidance, support, and encouragement throughout this study. The author also expresses his cordial thanks to Dr. Masafumi Minoshima, Dr. Yuichiro Hori, and Dr. Tomoya Yamamoto for their kind help and valuable discussions.

The author is deeply grateful to Professor Masaru Ishii, Dr. Junichi Kikuta, Dr. Kentaro Fujii, and Dr. Shinya Yari at the Graduate School of Medicine in Osaka University for their technical support and valuable advice regarding intravital imaging and flow cytometry measurement. The author is also grateful to Professor Fumihito Ono and Dr. Souhei Sakata at Osaka Medical and Pharmaceutical University for their technical support and valuable advice regarding the two-electrode voltage clump. The author is also grateful to Professor Nemoto Tomomi, Dr. Hirokazu Ishii, Yuki Watakabe, Dr. Saeko Yanaka, and Professor Koichi Kato at National Institutes of Natural Sciences, Exploratory Research Center on Life and Living Systems for their technical support and valuable advice regarding the two-photon uncaging and HPLC analysis. The author is also grateful to Dr. Hideji Murakoshi at National Institute for Physiological Sciences for their technical support and valuable advice regarding single spine stimulation.

The author also thanks all the members of the Kikuchi laboratory for their kind help, teaching, and friendship.

The author is honored and grateful to have received financial support from the Japanese Chemical Industry Association and Interactive Materials Science Cadet Program. Finally, the author appreciates the tremendous support and continuous encouragement from his family and friends.

Osaka, Japan
January 2024

Ryu Hashimoto

Laboratory of Chemical Biology
Division of Applied Chemistry
Graduate School of Engineering
Osaka University